UNIVERSITY OF CALIFORNIA, SAN DIEGO

Bit patterned media with composite structure for microwave assisted magnetic recording

A dissertation submitted in partial satisfaction of the requirements for the degree Doctor of Philosophy

in

Electrical Engineering (Applied Physics)

by

Nasim Eibagi

Committee in charge:

Professor Eric E. Fullerton, Chair
Professor Vitaliy Lomakin
Professor Shirley Meng
Professor Shayan Mookherjea
Professor Oleg Shpyrko

2016

The Dissertation of Nasim Eibagi is approved, and it is acceptable in quality and form for publication on microfilm and electronically:

Chair

University of California, San Diego

2016

Dedication

To my parents for their endless love and support …

Table of Contents

List of Symbols

γ Gyromagnetic ratio
e Electron charge
μ Magnetic moment
v Veloscity
c Speed of light
M Magnetization
χ Suceptibility
H Magnetic field
E energy
K anisotropy constant
μ_B Bohr magneton
H_k Anisotropy field
E_B Energy barrier
M_s Saturation magnetization
$\hbar$ Plank's constant
R Resistance
H_{ex} Exchange field
ω_0 Precession frequency
GB Giga byte
HDD Hard disk drive
CGR Compound growth rate
FM Ferromagnet
AFM Antiferromagnet
PMA Perpendicular magnetic anisotropy
ECC Exchanged coupled composite
BPM Bit patterned media
SEM Scanning electron microscopy

List of Figures

List of Tables

Acknowledgements

I wrote this part last since I don't know how to put in words that how much I am grateful for the amazing people that helped me through this journey.

Mom and Dad, from bottom of my heart, I appreciate all the sacrifices you made in your life for my success. Thank you for teaching me to be positive, logical, and persistent. I would also like to thank my brothers, Amir and Omid, for always being there for me, support me and for being the best brothers one can ever have.

I would like to thank my husband, Omid for his support through last years of my Ph.D. You always loved, encouraged, and helped me to continue my path with high self-confidence.

Fullerton group, thank you for being great friends and for supporting me in various ways, which helped to make this journey possible.

I am grateful for having an amazing advisor, Professor Eric Fullerton. Thank you for your support and help that assisted me to achieve my lifelong wish of becoming a scientist. I always feel thankful for having you as my teacher and role model, and I will be lucky if I ever could accomplish a tiny bit of your success!

Technical Acknowledgement:

Chapter 4, in part, is published: N.Eibagi, J.J. Kan, F.E. Spada, and E.E. Fullerton, "Role of dipolar interaction on the thermal stability of high density bit-patterned media", IEEE Magnetic Letters, vol.3, pp.4500205 (2012). I also would like to thank Fred Spada for giving me access to the polar MOKE for data that is represented in chapter 4.

Chapter 5, in part is currently being prepared for publication. N. Eibagi, S.W. Chen, H. Guo, S. Sinha, V. Lauter, and E.E. Fullerton. I also would like to thank H.Ambaye, R. Goyetter and V. Lauter who helped me with neutron experiments in chapter 5. Research at Research at the ORNL Spallation Neutron Source ORNL was sponsored by the Scientific User Facilities Division, Office of Basic Energy Sciences, US Department of Energy. ORNL is managed by UT-Battelle, LLC, under contract DE-AC05-00OR22725 with the US Department of Energy.

Chapter 6, in part, is currently being prepared for publication. N.Eibagi, J.J. Kan and E.E. Fullerton.

I would like to thank Department of Energy for funding my research.

Vita

2009	Bachelor of Science, University of California, Davis
2011	Master of Science, University of California, San Diego
2016	Doctor of Philosophy, University of California, San Diego

Publications

1. D.A. Gilbert, G.T. Zimanyi, R.K. Dumas, M. Winklhofer, A. Gomez, N. Eibagi, J.L. Vincent, and K. Liu, "Quantitative decoding of interactions in tunable nanomagnet arrays using first order reversal curves", Scientific Reports, vol. 4, 4204 (2014)
2. V. Uhlir, M. Urbanek, L. Hladik, J. Spousta, M.Y. Im, P. Fischer, N. Eibagi, J.J. Kan, E.E. Fullerton and T. Sikola, "Switching vortex chirality in patterned magnetic nanodisks by nanosecond field pulses" Nature Nanotechnology, vol. 8, pp.341(2013).
3. J. Dou, M. J. Pechan, E. Shipton, N. Eibagi, and E.E Fullerton, "Tunable resonant properties of perpendicular anisotropy [Co/Pd]/Fe/[Co/Pd] multilayers" J. App. Phys.,Vol. 113, pp.17C115 (2013).
4. N.Eibagi, J.J. Kan, F.E. Spada, and E.E. Fullerton, "Role of dipolar interaction on the thermal stability of high density bit-patterned media", IEEE Magnetic Letters, vol.3, pp.4500205 (2012).
5. R.K. Dumas, D. Gilbert, N. Eibagi, and K. Liu ,"Chirality control via double vortices in asymmetric Co dots", Physical Review B, 83 060415 (2011).
6. M.T. Rahman, R.K. Dumas, N.Eibagi, N.N. Shams, Y. Wu, K. Liu, and C. Lai, "Controlling magnetization reversal by engineering the geometry of nanostructure with perpendicular anisotropy", Applied Physics Letters, 94, 042507(2009).

Presentations

1. "Exchange coupled composite bit patterned media for microwave assisted magnetic recording", Eibagi, S.W Chen, H. Guo, J.J. Kan, V. Lauter, J. Dou, M. J. Pechan, S.S. Sinha, and E.E. Fullerton, The 58th MMM conference, November 2013. (Poster presentation)
2. "Depth dependent magnetization study of composite bit patterned media", N.Eibagi, S.Chen, H. Guo, J.J. Kan, V. Lauter, S.S. Sinha, and E.E. Fullerton, The 12th Joint MMM and Intermag conference, January 2013.
3. "Composite structure for bit patterned media". N. Eibagi, J.J. Kan, M. Lubarda, V. Lomakin, and E.E. Fullerton, The 56th MMM conference, November 2011.

4. Center for Magnetic Recording Research review talks every six months.
5. “Controlling magnetization reversal in Co/Pt networks with perpendicular anisotropy”,N. Eibagi, R.K. Dumas, K. Liu, M.T. Rahman, N.N. Shams, Y. Wu, C. Lai, APS California section meeting, October 2008.

ABSTRACT OF THE DISSERTATION

Bit patterned media with composite structure for microwave assisted magnetic recording

by

Nasim Eibagi

Doctor of Philosophy in Electrical Engineering (Applied Physics)

University of California, San Diego, 2016

Professor Eric E. Fullerton, Chair

Patterned magnetic nano-structures are under extensive research due to their interesting emergent physics and promising applications in high-density magnetic data storage, through magnetic logic to bio-magnetic functionality. Bit-patterned media is an example of such structures which is a leading candidate to reach magnetic densities which cannot be achieved by conventional magnetic media.

Patterned arrays of complex heterostructures such as exchange-coupled composites are studied in this thesis as a potential for next generation of magnetic recording media. Exchange-coupled composites have shown new functionality and

performance advantages in magnetic recording and bit patterned media provide unique capability to implement such architectures. Due to unique resonant properties of such structures, their possible application in spin transfer torque memory and microwave assisted switching is also studied.

This dissertation is divided into seven chapters. The first chapter covers the history of magnetic recording, the need to increase magnetic storage density, and the challenges in the field. The second chapter introduces basic concepts of magnetism. The third chapter explains the fabrication methods for thin films and various lithographic techniques that were used to pattern the devices under study for this thesis. The fourth chapter introduces the exchanged coupled system with the structure of [Co/Pd] / Fe / [Co/Pd], where the thickness of Fe is varied, and presents the magnetic properties of such structures using conventional magnetometers. The fifth chapter goes beyond what is learned in the fourth chapter and utilizes polarized neutron reflectometry to study the vertical exchange coupling and reversal mechanism in patterned structures with such structure. The sixth chapter explores the dynamic properties of the patterned samples, and their reversal mechanism under microwave field. The final chapter summarizes the results and describes the prospects for future applications of these structures.

Chapter 1: History and Principal of Magnetic Recording

1.1. Digital Universe

We are living in a digital era, where most daily operations are done digitally; from people using their smartphones, tablets, and laptops on daily basis to various enterprises in the society. As technology advances, our world gets more digitized, and as a result more digital data is being generated, transmitted and processed. The International Data Corporation (IDC) and EMC Corporation report on the digital universe on yearly basis. The recent IDC study published in April 2014 [(1)] finds that digital universe is expected to continue to grow at 40% annually for next decade and the amount of data that is created in 2013, 4.4 trillion Giga bytes (GBs), will grow by a factor of 10 by 2020 to 44 trillion GBs, and this is 300 times of the digital data that was produced in 2005[(1,2)]. These studies confirm that digital universe nearly doubles every two years [(1)]. The graph shown in Fig. 1 compares the total digital data over the past few years and compares it to the expected value for year 2020 [(1, 2, 3, 4, 5, 6, 7)]. Based on the statistics the digital universe is growing fast; however, the yearly storage capacity increase rate is much slower. In 2013 available storage capacity could only store 33% of the created data and this number is expected to decrease to 15% in 2020[(1)]. Thus, new technologies are required to maintain or increase the growth of the storage capacity to keep up with societal demand.

Hard disk drives (HDDs) are one of the reliable storage technologies that have been used for more than 50 years and is the dominate technology for archival storage.

HDDs are non-volatile and low cost comparatively, and they provide good power

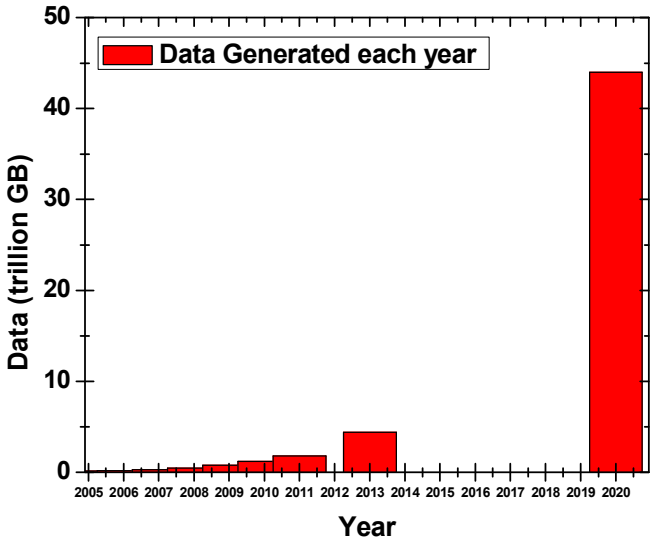

Figure 1: This graph shows the number of data that is generated and processed in each year and the predicted value for the year 2020. This data is collected by IDC [1, 2, 3, 4, 5, 6, 7].

efficiency along with fast data access. In this thesis, new advances are discussed which would help to innovate next generation HDDs. Thus, it is crucial to understand the magnetic recording process and critical aspects of the HDD. The rest of this chapter concentrates on the history of the magnetic recording and provides a basic introduction of the HDD and its mechanism. At the end, the challenges for further increasing of the areal density of HDDs will be addressed, and the new emerging technologies to address these challenges will be introduced.

1.2. History of Magnetic Recording

Magnetic recording started with Oberlin Smith. He was an American engineer, who was motivated with Edison's invention of the phonograph. In 1888 he published in Electrical World a proposal for recording sound (music) as a magnetic signal on a silk or cotton thread which included steel and metal particles to be magnetized [8]. However, it wasn't until 1898 when Valdemar Poulsen, a Danish inventor, was able to build a working magnetic recording machine, and he named it the Telegraphone (Fig. 2) [9] that recorded an analog signal onto a metal wire. This was the beginning of the magnetic recording and the basic concept was shown in the original US patent #661,619 (Fig. 2). After many decades of works on this approach which, at the time,

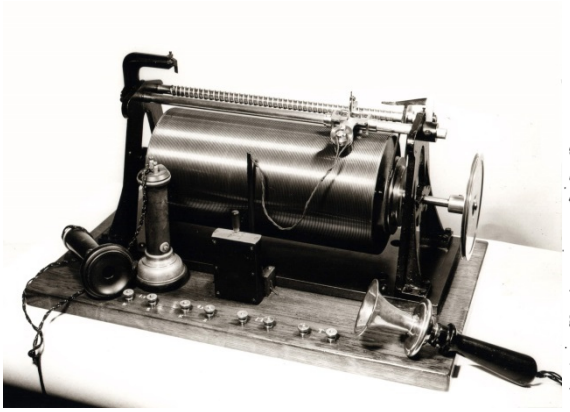

The solution of this problem is based on the discovery that a paramagnectic body, such as a steel wire or ribbon, which is moved past an electromagnet connected with an electric or magnetic transmitter, such as a telephone, is magnetically excited along its length in exact correspondence with the signals, messages, or speech delivered to the transmitter, and, further, that when the magnetically-excited wire is again moved past the electromagnet it will reproduce the said signals, messages, or speech

Figure 2: The Poulson Telergraphone , 1989 [11] along with text from the original UC patent#661,619 describing the working concept.

was "new" topic, on 1928 Fritz Pfleumer, a German-Austrian engineer developed the first magnetic tape. On 1929 he patented a tape which is made of oxide bonded to a film as the magnetic tape for magnetic recording [10]. Magnetic tapes launched the information age and they were the main means for recording audios and videos for

decades. Further along the path, hard disk drives were invented and provided an approach for digital magnetic data storage.

1.3. Hard Disk Drive

The first commercialized hard drive was implemented by IBM in 1956, the IBM 305 RAMAC, where RAMAC stands for "Random Access Method of Accounting and Control" and provided real time accounting. RAMAC had fifty, 24-inch disks with total capacity of 5 Mbytes which corresponded to an areal storage density of 2000 bits per square inch. It had the access time of just less than a second and it costs 1cent per byte [12,13]. Later the ongoing research resulted in improvements in write and read processes which helped in size and cost reduction along with increase of the data access time and areal density. It was on 1980 when IBM 3380 was introduced as first over gigabyte storage which still was as big as a refrigerator. This computer had two hard drives each with the capacity of 1.26 GB[14]. The ongoing research led to today's HDDs, 2.5 and 3.5 inch drives with storage densities of 500 GB/in^2 and more.

Figure 3 shows the trends and evolution of the HDD over the last 15 years [15] compared to flash technologies. In the first few decades after the development of the first HDD, the increase in areal density were achieved through conventional scaling of the HDD's write and head elements and related parts which led to using magnetic thin films as recording layer and resulted in annual compound growth rate (CGR) of 30%.

One of the major breaks in scaling of the HDD to achieve higher density was the introduction of the magneto-resistive read head. Previously the same head was used to write and read the data. The read-back was achieved by the inductive signal in the head resulting from the changing magnetic fields arising from the transitions. The magneto-resistive head directly measures the field strength and further allowed the separate optimization of the read and write heads. The first implementation used the anisotropic magneto-resistance (AMR) which boosted the CGR to 60% in early 1990's. Later, in 2000 the giant magneto-resistance (GMR) effect was utilized in the head's and the CGR reached to 100%. Tunneling magneto-resistance (TMR) is currently used in modern heads. As the rate started slowing down around 2005 due to thermal instabilities in the recording media, perpendicular magnetic recording was introduced to replace the conventional longitudinal recording. The current computer and devices work with 2.5 and 3.5 inch hard disk drives with the areal density of 500 GB/in^2 and more. In 2011 Toshiba designed a 500GB HDD 2.5 inch by using multiple platters with areal density of 744 GB/in^2 [16].

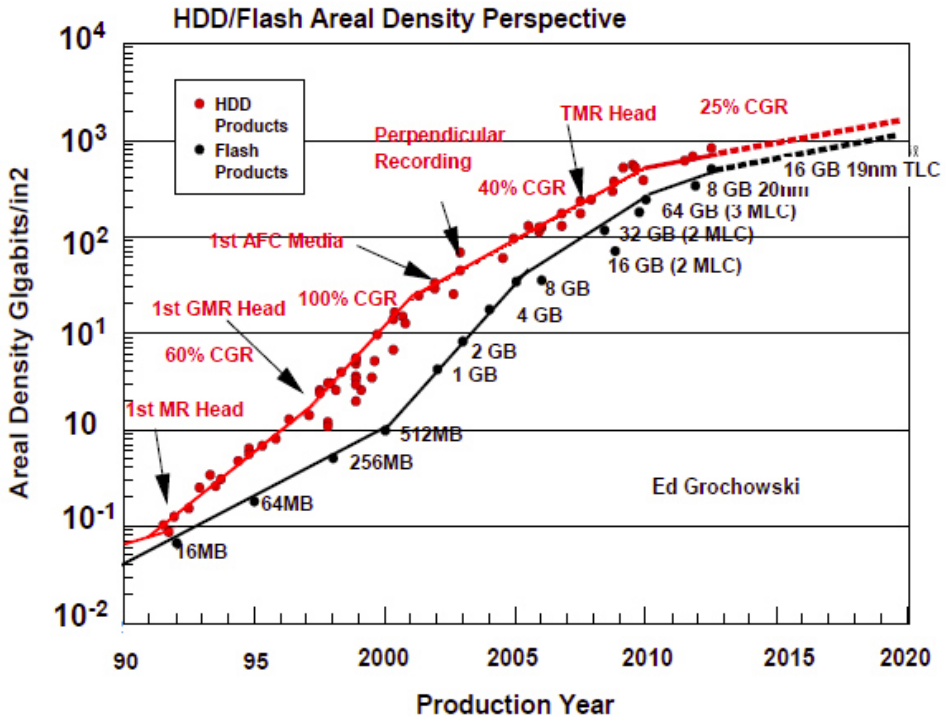

Figure 3: Evolution of hard disk drives' area density through years[(courtesy of Edward Grochowski)(15)].

1.3.1. Hard Disk Drive's Mechanical Configuration

It is crucial to understand the basics of a conventional HDD parts to further discuss the possible promising technologies to increase the areal density. A typical HDD and its parts are shown in Fig. 4. There are one or more disks which are made of aluminum or glass substrates and are covered with thin-film layers including the under layers/ magnetic layers/ protection layers/ and a lubricant layer. The information is stored in bits as the direction of magnetization of a collection of magnetic grains in the magnetic layer. The bits form concentric circular paths (tracks). The disk is mounted

to a spindle motor which rotates 5400 to 15000 rpm [17]. There is an actuator arm which at its tip, there is a slider which flies at close proximity to the media surface where the read/write element (head) is implemented. This arm moves the head across the platter for data to be written or read from the platter.

The areal density increase is possible by modifying the mechanical, electrical and magnetic parts of HDD. In general higher storage capacity is achieved by scaling although, as mentioned in section 1.3, the advances in magnetoresistive read head technology resulted in increased areal density growth in 1990's. The basic idea of scaling is that if all dimensions of a HDD components are scaled by the same factor the performance of the drive is maintain and higher storage densities are achieved. The reduction of the dimensions of hard disk drive components such as read and write element (head), recording media, and also the head and media spacing have been scaled over the recent decades to increase the areal density. However, this method is reaching its limit as a result of numerous challenges such as thermal instability of the recording media and limits in fabrication methods.

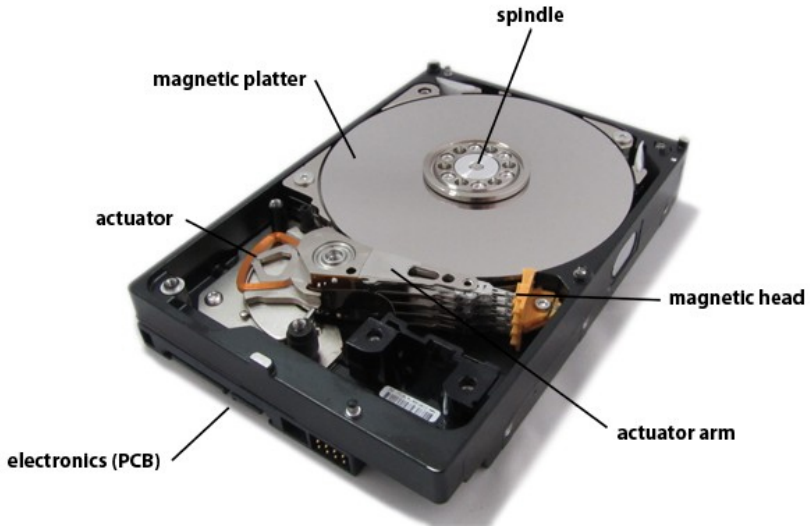

Figure 4: A conventional hard drive is shown where some of the mechanical parts are highlighted [18].

In the next section, the challenges in the increasing the areal density of hard disk drives by conventional methods are discussed in more details and the new technologies to replace the traditional methods are introduced.

1.4. Magnetic Trilemma

As mentioned in section 1.1, the rate of digital data creation in society is increasing exponentially which puts pressure on hard drives suppliers to produce drives with every increasing areal density to keep pace. However, as it was discussed in the previous section, increasing HDD's area density requires total scaling of HDD mechanical parts along with grain size in magnetic recording thin films to keep the magnetic grains per bit. The magnetic grains are introduced to limit magnetic correlation lengths in the media and allowing data to be written with high spatial

resolution. The transition from one bit to another will be defined by grain boundaries. The uncertainty in the position of the transitions in magnetic recording (known as the transition jitter) can be estimated by the equation:

$$\sigma = \frac{\pi^2}{4} a \sqrt{\frac{s}{3W}} \quad (1)$$

where a is the transition width, and s is the cross-track correlation length (the distance over which the magnetic transition fluctuates across the width of the track, W). For uniform, magnetically decoupled grains, the media's transition width is a half the grain diameter (D/2) and s = D. Thus, for the well-defined media the jitter scales as $D^{3/2}$. Because of this, to achieve higher areal densities it is very important to have as small as possible grain diameter.

The superparamagnetic effect or the magnetic 'trilemma' (shown schematically in Fig. 5) describes the results of enhanced thermal effects in modern recording media that has been proposed as a physical limit to the growth of areal density. This arises from scaling the media thickness (t) and grain diameter (D). As the grain volume $V = \pi D^2 t/4$ is reduced in the scaling process, the magnetization of the grains may become unstable due to thermal fluctuations, and data loss may occur. The weak intergranular exchange coupling between the grains allows the recording medium to be approximated as a collection of independent particles (as was assumed in Eq. (1)). The energy barrier for magnetization reversal in the presence of an external magnetic field H is given by:

$$E_B(H,V) = K_u V\left(1 - \frac{H}{H_0}\right)^n \quad (2)$$

where K_u is the magnetic anisotropy density and H_0 is the intrinsic switching field (coercive field). For simplicity of the following discussion, the energy barrier can be considered as $E_B=K_UV$. However depending on the data pattern, there will be fields generated that can lower the energy barrier. When considering finite temperatures, the energy barrier needs to be compared to the thermal activation energy k_BT, where k_B is Boltzmann's constant and T is the absolute temperature. Thermally activated switching is characterized by a time constant t following the Arrhenius Néel law:

$$\tau = \frac{1}{f_0}\exp\left(\frac{E_B}{k_BT}\right) \quad (3)$$

The attempt frequency f_0 is on the order of $10^9 - 10^{12}$ Hz and sets the time scale for thermally activated magnetization reversal. To have the data stable greater than 5 years (i.e. $\tau > 5$ years) sets a stability requirement of K_UV exceeds 50 k_BT. To deal with distributions and elevated temperatures during operation the average grain stability is maintained at 75 k_BT at room temperature.

In traditional scaling you need to decrease the grain diameter and thickness with increasing areal density. To first order you want the number of grains per bit to remain constant as you go to higher storage densities and to maintain the read-back signal-to-noise ratio (SNR). Therefore to maintain thermal stability as V decreases as you make the bits (and grains) small you need to increase K_U to maintain thermal stability which increases the write field requirements. The write field (H_w) from the write head must be exceed the media coercive field that is given by:

$$H_C \approx H_0 \approx \frac{K_u}{M_s} \quad (4)$$

where M_s is the saturation magnetization of the recording media. Write field improvements were traditionally achieved by design changes in the write head and the use of materials with higher saturation magnetization as the write poles. However, modern write poles already consist of low-anisotropy materials with saturation magnetization density approaching the highest recorded value. Thus H_w is limited and does not increase with scaling which, in turn, places a limit on the coercive field of the media (i.e. puts a limit on the media anisotropy K_u). The competition between media SNR (i.e. small grain volume V), thermal stability ($K_uV>50\ k_BT$) and writability ($H_C<H_W$) in magnetic recording is known as the magnetic trilemma (Fig. 5) which influences the magnetic media design greatly.

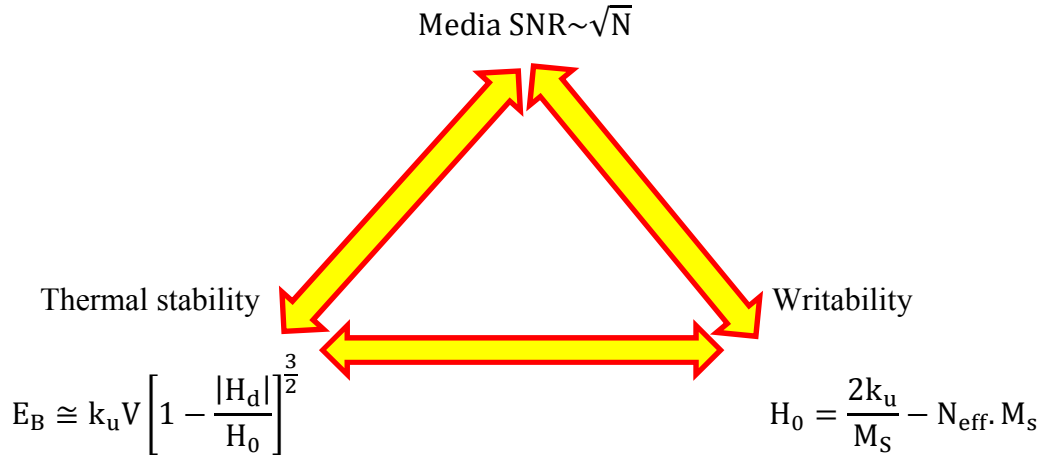

Figure 5: Magnetic trilemma which considers the challenges for the HDD capacity increase.

There are numerous possible solutions to the magnetic recording trilemma which leads to new recording technologies: perpendicular magnetic recording (PMR) [19], exchange-coupled media [20, 21, 22, 23, 24, 25, 26], energy-assisted magnetic recording, and bit-patterned media (BPM) [27]. PMR in combination with exchange-coupled media is already being used by industry in state-of-the-art HDDs. Exchange coupled media provide thermally stable small grains while remains in the range of conventional field for writability through engineering of the magnetic material. In energy assisted techniques, a media with small grains and high anisotropy is being used, but to solve the writability problem, an external energy such as heat (heat assisted magnetic record, HAMR) [28] or RF frequency (microwave assisted magnetic recording, MAMR) [29] are being used during the writing process to help the switching by reducing the energy barrier. Bit-patterned media uses the lithographic technique to create a magnetic recording media with patterned islands with diameter of 30nm and less which results in high areal density. This significantly increases the magnetic volume V since now you only have one magnetic grain per bit.

In this thesis, exchange-coupled media is studied in the form of bit-patterned media and the dynamic properties of the media were studied for possible combination with MAMR.

Chapter 2: Principles of Magnetism

2.1. Magnetism

Materials are made of atoms and atoms are made out of electrons in orbital motions around the nucleus. Electrons are the main origin of magnetism in materials due to their natural properties: spin, orbital motion and interactions. Magnetic moments are defined by the orbital motion and spin of an electron [30]:

$$\mu(\text{Orbit}) = \frac{e\vartheta r}{2c} \text{ (cgs) or } \frac{e\vartheta r}{2} \text{ (SI)} \quad (5)$$

$$\mu(\text{Spin}) = 0.927 \times 10^{-20} \text{ emu} = 9.27 \times 10^{-24} \text{ Am}^2 \quad (6)$$

where e is electron charge, v is the velocity of electron in orbit, r is the radius of orbit, and c is the speed of light. The vector sum of the electron moments define the atomic moment and this would divide atoms in two main groups of magnetic and non-magnetic. If the orientations of the magnetic moment of electrons result in a net magnetic moment of zero, then this class of atoms is called diamagnets or non-magnets. The rest with non-zero net magnetic moments are called magnetic atoms. The combination of the magnetic atoms results in materials which further get divided in to four basic magnetic groups: paramagnets, ferromagnets, antiferromagnets, and ferrimagnets.

2.1.1. Diamagnetism

Diamagnets are materials with atoms that have full orbits and no unpaired electrons such as monoatomic gasses, He, Ne, etc. Ionic solids and covalent bonded materials with full shell are also examples of diamagnetic materials. These materials in a magnetic field produce negative magnetization within the materials that opposes the external field. This effect is explained classically by Paul Langevin. The electron orbital motion creates currents which produce a magnetic dipole and the external field applies a torque on the magnetic dipole and drives it into precession. This results in reduction in effective current arises a magnetic moment to oppose the external field (negative magnetization). As a result these materials are known to have negative susceptibility where magnetic susceptibility, χ, is the value that represents the amount of magnetization induced in a material in an external field.

$$\vec{M} = \chi \vec{H} \tag{7}$$

where M is the magnetization, and H is the external field. The magnetization, M, is vector sum of magnetic dipole moments per unit volume, m/V. Superconductors are class of materials that are perfect diamagnets (for small fields) with susceptibility of negative one, (χ = -1) for field below the critical field.

2.1.2. Paramagnetism

This group of materials' atoms has net magnetic moment but these atoms orient randomly such a way that the net magnetization is zero in absence of any external magnetic field at finite temperature (Fig. 6). This is due to the randomizing

effect of temperature. In the presence of external field the magnetic, the field works against the effect of temperature and the magnetic moment of atoms rotate in the direction of the applied field and causes partial alignment of the magnetic moments, and results in net magnetization. Based on Curie-Weiss law the susceptibility (in the low field linear regime) of paramagnetic materials depends inversely on the temperature:

$$\chi = \frac{C}{T-\theta} \tag{8}$$

where C is the curie constant that is material dependent, T is temperature, and θ is a constant that is related to the magnetic interactions of atoms. θ has dimension of temperature and also is being called Curie temperature, T_C. At this critical point, T_C, the orientation of magnetic moment changes direction. Below the Curie point the magnetic material has net magnetic moment (ferromagnetism) and above this point the sample becomes paramagnetic.

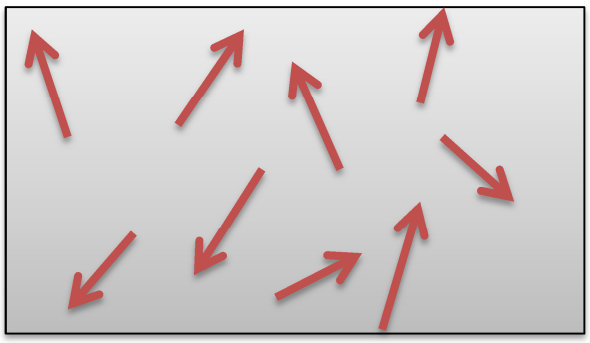

Figure 6: Schematic of a paramagnet material. The random orientationof moments results in zero net magnetization.

2.1.3. Ferromagnetism

Ferromagnets have net magnetic moment in the absence of external field because they are spontaneously magnetized. Ferromagnets are Fe, Ni, and Co and many of their alloys along with some rare earth materials. The ferromagnetism origin can be explained phenomenologically through a molecular field:

$$\vec{H}_m = \gamma \vec{M} \tag{9}$$

where γ is the molecular field coefficient and M is magnetization. Ferromagnets have very strong molecular field that causes spontaneous magnetization without presence of external magnetic field. The origin of molecular field can be explained through the quantum mechanical effect of exchange interactions which will be discussed in detail in the next section. This effect causes that the spin of unpaired electrons to align. Although ferromagnets are spontaneously magnetized, ferromagnets materials like a piece of iron, in general, can be found with no net magnetization; that is because these materials are divided into regions which are called domains (Fig. 7), and within each domain the magnetic moments are aligned, but the magnetizations of domains are aligned in a way that the net magnetization of the whole material is zero. The domain formations within ferromagnets are due to minimizing the total magnetic energy which is discussed in detail in the next section.

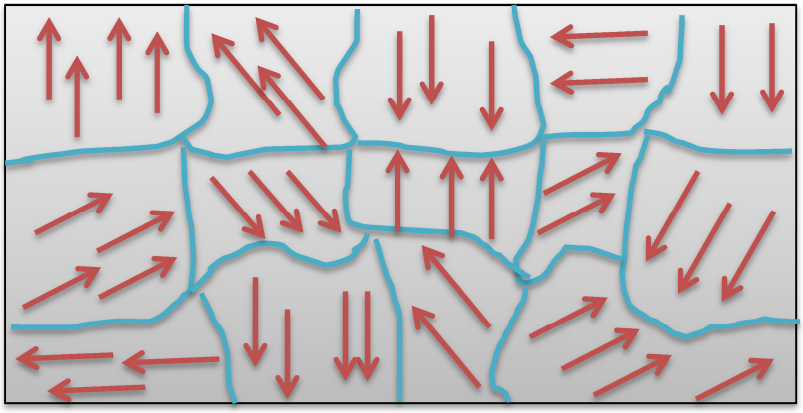

Figure 7: Schematic of a ferromagnet which contains domains in the absenceof external field. Although within each domain there is a spontaneous magnetization, the net magnetization of the sample is zero.

When a magnetic field is applied to a ferromagnetic material, the magnetizations of domains align with the direction of the field and the sample becomes magnetized, and it can maintain its magnetization at zero field. A field in the opposite direction is actually is needed to further bring the magnetization to zero and eventually magnetized the sample in the opposite direction. The behavior of magnetization vs. field traces a loop which is called hysteresis loop (Fig. 8). By measuring hysteresis loops, important magnetic properties can be extracted such as saturation magnetization (M_s), saturation field (H_s), coercivity (H_c) (Fig. 8).

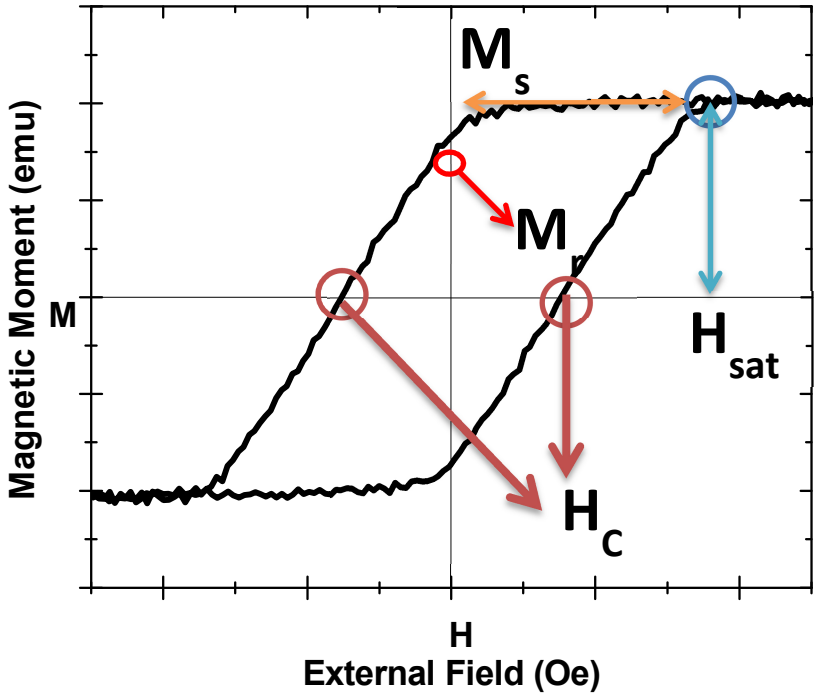

Figure 8: A typical ferromagnetic magnetic hysteresis. The important information that can beextracted from hysteresis loop is pointed out such as coercivity field (H_C), remnant magnetization (M_r), saturation field (H_{sat}), and saturation magnetization (M_S).

2.1.4. Antiferromagnetism

Antiferromagnets consist of two sub-lattices of magnetic ions. These sub-lattices have opposing magnetic moments as it shown in Fig. 9. The cause of this alignment is again due to molecular field or exchange force which is negative for these materials (exchange integral was positive for the case of ferromagnetism). The antiferomagnets' susceptibility depends on the temperature and also obeys the Curie-Weiss law but the negative sign **θ** should be considered in Eq. 8. Here this temperature

is called Néel temperature above which antiferomagnets change to paramagnets since the thermal fluctuations overcome the molecular field.

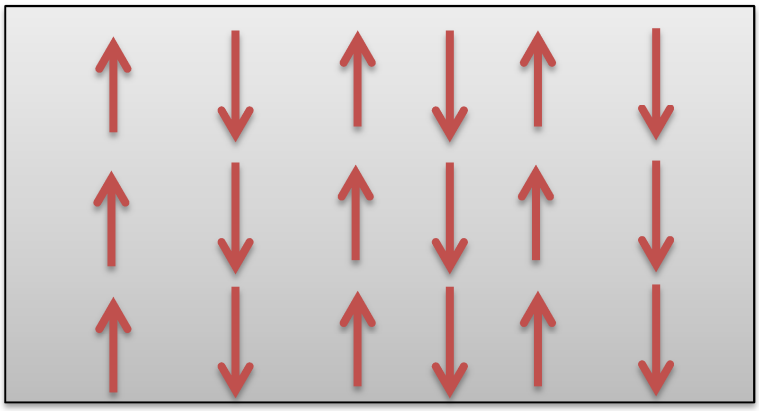

Figure 9: Schematic of an Antiferromagnet which has two sublattices with opposite and equal magnetic moments.

2.1.5. Ferrimagnetism

Ferrimagnets like antiferromagnets consist of two sub-lattices with opposing moments, but they have spontaneous magnetization at room temperature. This means that one of the sub-lattices have slightly higher magnetic moment than the other (Fig. 10). Some examples of ferrimagnets are some rare earth transition metals, most double oxides of iron and ferrites.

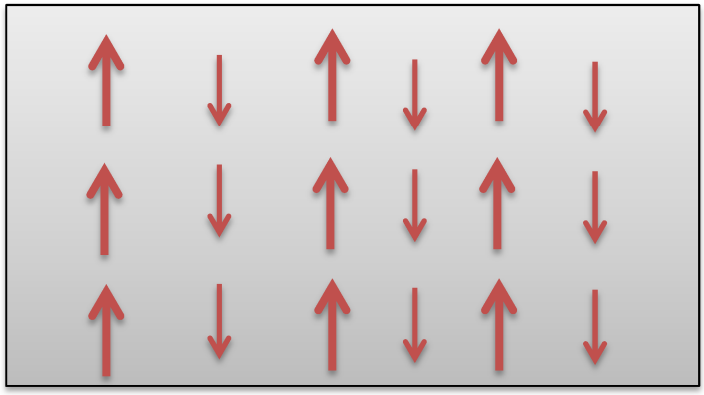

Figure 10: Schematic of a ferrimagnet. It has two sublattices with opposite magnetic direction anddifferent magnitudes.

2.2. Magnetic Energies

Within a magnetic sample the total energy represent the total interactions of magnetization. As an example, as it mentioned in section 1.2.3., ferromagnets are divided into domains where magnetization has different direction. Domain walls separate domains that within it, the direction of magnetization changes. The width of the domain wall is determined based on the sample's magnetic energies (Exchange and Anisotropy).

The total energy is the sum of Zeeman energy (resulting from the external magnetic field, E_Z), exchange energy (interactions, E_{ex}), demagnetizing energy (dipole interaction, E_d), and anisotropy energy (i.e. crystal fields, E_A):

$$\vec{E}_{total} = \vec{E}_Z + \vec{E}_{ex} + \vec{E}_d + \vec{E}_A \qquad (10)$$

Each one of these energies is going to be introduced in the following subsections.

2.2.1. Zeeman Energy

Zeeman energy is the interaction between magnetic moment and an external magnetic field:

$$\vec{E}_Z = -\vec{M}.\vec{H}_{ext} \quad (11)$$

The external field exerts a torque on magnetic moment which tends to align the magnetic moment along the external field to minimize the Zeeman energy.

2.2.2. Exchange Energy

Exchange energy (exchange interaction) is a quantum mechanical effect between two electrons and depends on the orientation of their spins. When two electrons are near each other they would interact through their wavefunction as it overlaps. This interaction is considered the strongest in solids and it is the reason for well-known Pauli Exclusion Principle which states that two electrons can have same energy if their spin orientations are opposite of each other. The exchange energy in case of two electrons can be defined as:

$$E_{ex} = -2\, J_{ex}\vec{S}_i.\vec{S}_j \quad (12)$$

where J_{ex} is exchange integral which depends on characteristic of the magnetic material and it's crystal structure, and S_i and S_j are the spins of the i^{th} and j^{th} electrons respectively. The exchange integral describe the coupling or magnetic moments' orientation (nearest neighbors) based on the interatomic distance which is shown in

Bethe-Slater curve (Fig. 11) . If $J_{ex} > 0$, then E_{ex} is minimum when S_i and S_j are parallel. This rare case happens for ferromagnets, and the exchange energy is

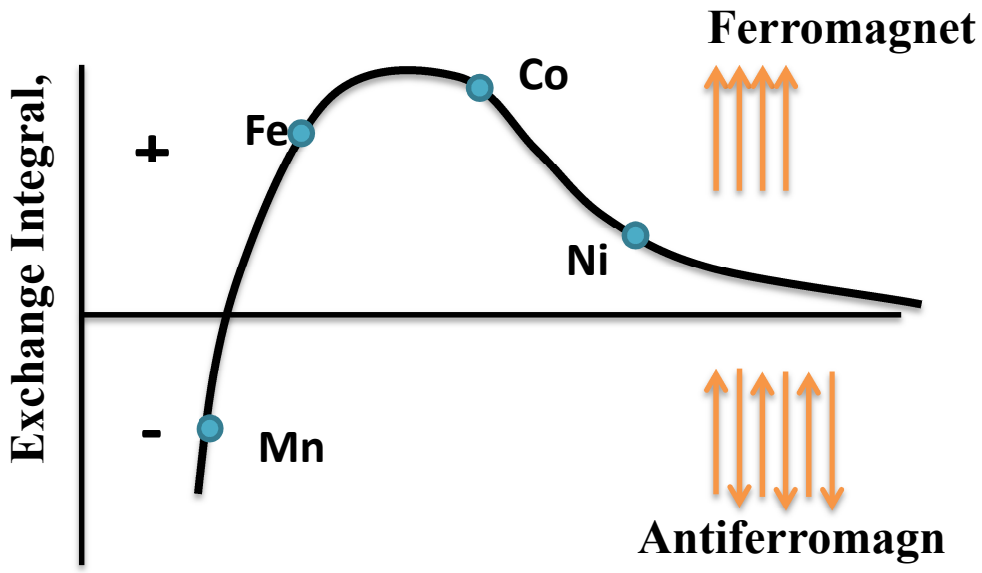

Figure 11: Schematic of Bethe-Slater curve.

responsible for the spontaneous magnetization in ferromagnets. If $J_{ex}<0$, then E_{ex} is minimum when S_i and S_j are antiparallel and this is the case for most atoms including antiferromagnets and ferrimagnets. Exchange interaction is short range and is strongest for nearest neighbors since it decreases rapidly with distance.

In solids, ferromagnetism can be explained through effects of the exchange interaction on the electron band model. This effect is due to delocalization of the electrons, and it is pronounced in Co, Fe, and Ni (transitional metals with partial filled *3d* and *4s* bands). The *3d* and *4s* bands have similar energy levels and they overlap. In

the case of ferromagnets since these levels are partially filled, the exchange force creates spin unbalance which give rise to non-zero magnetic moment.

2.2.3. Demagnetizing Energy

Demagnetizing energy arises from the dipole interaction between magnetic moments within the sample. A magnet produces external magnetic fields which oppose the internal magnetic moment (Fig. 12). This internal magnetic field is called demagnetizing field and depends on the macroscopic shape of the magnet and the magnetic domain configuration. This internal field produces an energy that is often referred to as the magnetostatic energy. The demagnetizing energy is defined as:

$$\vec{E}_d = -\frac{1}{2}\int_V \vec{H}_d . \overrightarrow{M}\, dV \tag{13}$$

$$\vec{H}_d = -N.\vec{M} \tag{14}$$

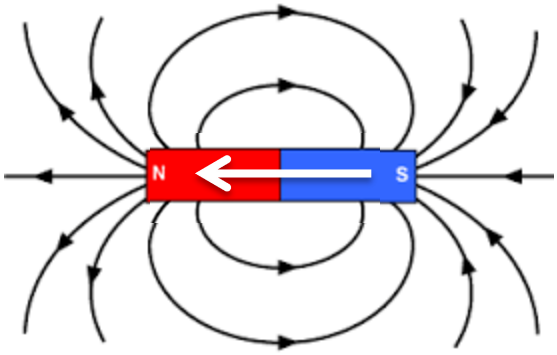

Figure 12: A bar magnet produce field outside and it has a field within itself.The internal magnetic. field has opposite direction compare to the external field, thus it is called demagnetizing field

N is the demagnetizing factor and depends on the geometry of the magnetic sample, and in the case of ellipsoid we can define N tensor as:

$$N = \begin{pmatrix} N_{xx} & 0 & 0 \\ 0 & N_{yy} & 0 \\ 0 & 0 & N_{zz} \end{pmatrix} \quad (15)$$

$$N_{xx} + N_{yy} + N_{zz} = 1 \text{ (SI) or } 4\pi \text{ (cgs)} \quad (16)$$

for sphere: $N_{xx} = N_{yy} = N_{zz} = \frac{1}{3}$ or $\frac{4\pi}{3}$, for infinite thin film which expands in the X-Y plane and has perpendicular magnetization : $N_{xx} = N_{yy} = 0$, $N_{zz} = 1$ or 4π , and for cylinder with its long axis along X axis $N_{xx} = 0$, $N_{yy} = N_{zz} = \frac{1}{2}$ or 2π . Base on the shape and as a result the demagnetization factor for the thin films, the magnetization would prefer to be in the plane of the sample to reduce the demagnetizing energy.

2.2.4. Anisotropy Energy

Anisotropy energies basically define how a magnetic material behaves in certain direction. There are different kinds of anisotropies such as magnetocrystalline, shape (which is a result of the demagnetizing energy sec. 2.2.3), and surface anisotropy. The magnetocrystalline anisotropy reflects the crystal symmetry of the material. The combination of the anisotropy energy defines the easy axis for overall magnetization of a particular material. Easy axis is a direction along which the energy is at minimum and hard axis is perpendicular to the easy axis (Fig. 13). Anisotropy is very important factor in the field of magnetization since by engineering it, new magnetic material systems can be designed for specific applications such as magnetic recording.

Magnetocrystalline anisotropy arises from interaction of the electrons and crystal field. For a cubic crystal the anisotropy energy is given by:

$$E_a = K_0 + K_1(\alpha_1^2\alpha_2^2 + \alpha_2^2\alpha_3^2 + \alpha_3^2\alpha_1^2) + K_2(\alpha_1^2\alpha_2^2\alpha_3^2) \quad (17)$$

where K_0, K_1, K_2 … are anisotropy constants, and α_1, α_2, and α_3 are directional cosines of magnetization with respect to the crystal axes. Orders higher than K_2 are very small and usually ignored, and K_0 is ignored since it is angle independent. A crystal with a single easy axis is called uniaxial crystal and the energy is referred to as uniaxial energy:

$$E_u = k_{u1}\sin(\theta)^2 + k_{u2}\sin(\theta)^4 \quad (18)$$

where θ is the angle between the magnetization and the easy axis. The uniaxial energy is minimized if the magnetization is along the easy axis.

The shape anisotropy is actually the same as the demagnetization energy. As it mentioned in the previous section the demagnetization factor is related to the shape of the sample that is why it is called “shape anisotropy”.

In very thin magnetic films where surface energies becomes more pronounced compare to the volume, surface anisotropies can dominate and causes the easy axis to be perpendicular to the plane of the sample. The surface anisotropy energy is given by K_S and assuming that the film thickness is less than the exchange length the surface anisotropy can be averaged over the film thickness and is given by:

$$E_s = \frac{K_s}{t} \tag{19}$$

In this thesis, the interest is on magnetic films with perpendicular uniaxial anisotropy. Thus, the total anisotropy of a thin-film with uniaxial anisotropy within first order can be calculated once all the anisotropy terms are known. The overall anisotropy constant is expressed as:

$$K_{eff} = k_u + \frac{2K_s}{t} - 2\pi M_s^2 \tag{20}$$

The K_{eff} includes the uniaxial anisotropy, K_u, surface anisotropy,$\frac{2K_s}{t}$ which comes from the top and bottom interfaces, and shape anisotropy, $2\pi M_s^2$. The sample has perpendicular anisotropy if $K_{eff} > 0$, this means the magnetization easy axis is perpendicular to the surface, and if $K_{eff} < 0$, the magnetization lies in the plane of the sample, parallel to the surface.

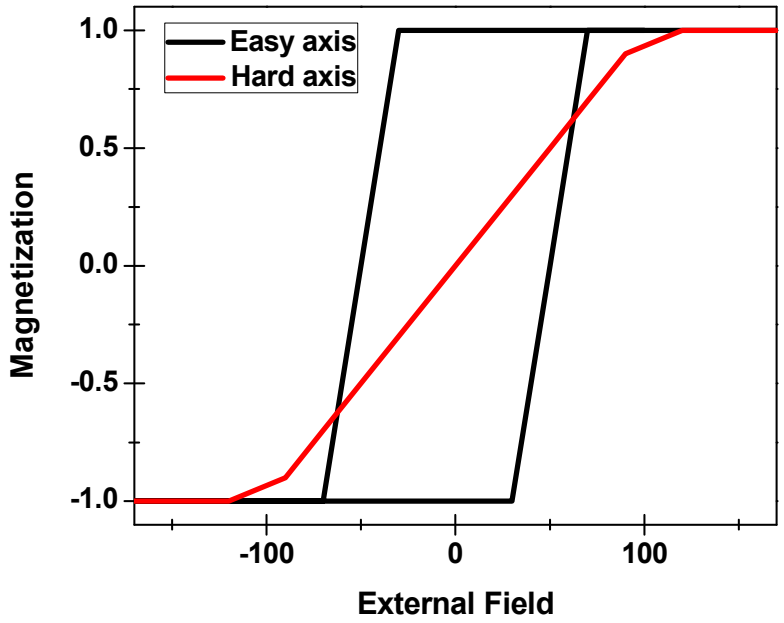

Figure 13: The hysteresis loop in two direction of easy (black) and hard (red)axis are shown. More energy is needed to saturate the magnetization in the hard axis.

2.3. Magnetic Interactions

The focus of this thesis is on magnetic thin multilayers which are patterned into islands. Thus among several magnetic interactions, this section is focused on dipolar interactions which is the dominate interaction between patterned islands and exchange interactions which control the interactions between layers. These interactions have important role in designing magnetic structures for various applications.

2.3.1. Dipolar Interaction

A magnetic moment by itself is a magnetic dipole and creates magnetic field. It is known that when a magnetic dipole is put in a magnetic field there is an interaction between them. Now let's consider two magnetic moments (magnetic dipoles) in vicinity of each other. Base on their relative orientation they exert force on each other to minimize their system total energy also known as the dipole-dipole interaction and depends on the magnitude of their magnetic moments, distance, and orientation. For two magnetic dipoles, the interaction is:

$$\text{Dipole} - \text{Dipole interaction} \propto \left[\frac{\mu_1 \mu_2}{r^3}\right](3\text{Cos}(\theta)^2 - 1) \qquad (21)$$

where μ_1 and μ_2 are the magnetic moment strength for islands one and two, respectively, r is their separation distance and θ is the angle that vector r makes with the Z axis. The strength of the interaction falls off by distance as r^3 as expected for a dipolar field. This interaction is very important in magnetic recording and it will be discussed later in this thesis that how the dipolar interactions will affect the magnetic properties of bit patterned media, since the patterned islands are very close to each other, they experience strong dipole-dipole interactions (Sec. 4.5).

2.3.2. RKKY Exchange Interaction

As it was explained in section 2.2.2., the origin of ferromagnetism is explained through nearest-neighbor exchange interactions. Longer-range exchange interactions explain ferromagnetic and antiferromagnetic coupling in magnetic multilayers. RKKY interaction (named after Ruderman, Kittel, Kasuya and Yoshida) is one type of

exchange that explains coupling between magnetic layers which are separated by a nonmagnetic metal [31,32,33,34]. Such interaction is called indirect because they are mediated through the nonmagnetic layer. The interaction happens through spin polarization of conduction electrons that is created by magnetic ions and is felt by adjacent magnetic layer. The exchange coefficient (j) determine if the neighboring magnetic layers' moments align parallel (ferromagnetically, $j>0$) or antiparallel (antiferromagnetically, $j<0$). The exchange coefficient depends on the thickness of nonmagnetic spacer and has a damped oscillatory behavior with increasing layer thickness.

Chapter 3: Fabrication Methods

3.1. Introduction

In this chapter the fabrication of magnetic thin films and various methods of patterning are discussed. There are many ways to deposit magnetic films such as magnetron sputtering [35], atomic layer deposition [36], molecular beam epitaxy [37,38], electro-plating [39] and chemical vapor deposition [40]. Each one of these methods is capable of creating thin (an atomic layer) of various materials along with creating multilayers and alloys. In this thesis magnetron sputter deposition was mainly used and will be discussed in the next section.

Lithographic methods are used to pattern various materials into different shapes for creating specific devices. These methods are being used vastly in industries such as semiconductors. Photolithography is used to pattern shapes with mostly dimensions larger than few hundred nanometers; for example, in this thesis photolithography was used to pattern hall crosses and wave guides. However, patterning much smaller features like arrays of sub-50nm, for bit patterned media, in a large scale, is challenging. There are different methods being used for patterning these features such as electron beam, self-assembly, nano-imprint, and interferometry lithography. Nevertheless, considering the cost and large scale pattering, self-assembly and nano-imprint lithography draw more attention.

3.2. Magnetron Sputtering

Magnetic thin films in this thesis are grown using magnetron sputtering. The basis of this technique is momentum exchange between high-energy ions and atoms of the target material. This process is done in a vacuum chamber with base pressure typically in the range of low 10^{-7} to 10^{-9} Torr. Figure 14 is schematic of vacuum chamber and shows the basis of deposition process. The target material is mounted on sputtering gun which has water cooled copper plate and a magnet array to confine the resulting plasma and it is negatively biased to be the cathode. The substrate in this process would be the anode. In DC magnetron sputtering to ignite and maintain a plasma, a process gas is needed which is usually an inert gas such as Argon that is introduced into the chamber at a level of a few mTorr. A high negative voltage in order of -1000-1500 volts is applied to the gun. When an Ar atom is ionized in the chamber to form an Ar^+ ion it is accelerated towards the sputter source and collides with target material. On collision a sputtered atom will be expelled from the target was well as some electrons e^-. The freed electrons are accelerated away the target and spiral around the magnetic field generated by the magnets below the target (Fig. 14) and thus are confined above the target surface. These high-energy electrons scatter with Ar atoms creating more ions.

$$e^- + Ar \rightarrow 2e^- + Ar^+$$

This process avalanches and plasma is ignited as result of Ar ionization and confinement of electrons by the magnet above the target surface. Once the plasma is stable the applied voltage drops to ~-300 V and current flows to the gun to replace the electrons. The positive Ar^+ ions continuously bombard the target (cathode) and eject

atoms through momentum transfer and these atoms are collected by the substrate. By controlling the power going to the gun the sputter deposition rate can be controlled. The guns are oriented at an angle toward the substrate and substrate is rotated during the sputtering process which ensures the uniformity of the deposited films. The sputtering parameters such as Ar pressure and voltage can be tuned to vary the sputtering rate and film quality such as roughness.

The thin films for this thesis are grown using an AJA DC magnetron sputtering system that is shown schematically in Fig. 14 (b). This system has eight 2" diameter sputter sources that use either RF or DC power supplies for deposition of insulating or conducting target materials, respectively. The sputter sources are angled to deposit at a single substrate location that readily allows alloys or heterostructures to be formed. The standard substrate size is 3" which can be heated to 850 °C with full DC or RF biasing as well as annealing in vacuum, oxygen or nitrogen atmospheres. With small changes in the transfer configuration, substrates up to 5" in diameter can be deposited. The system is compatible with reactive sputtering with nitrogen or oxygen at elevated substrate temperatures. The load lock holds multiple substrates that can be transferred into the main chamber. The system is computer controlled allowing automatic control of the gas flow, sputtering power supplies, substrate temperature and opening

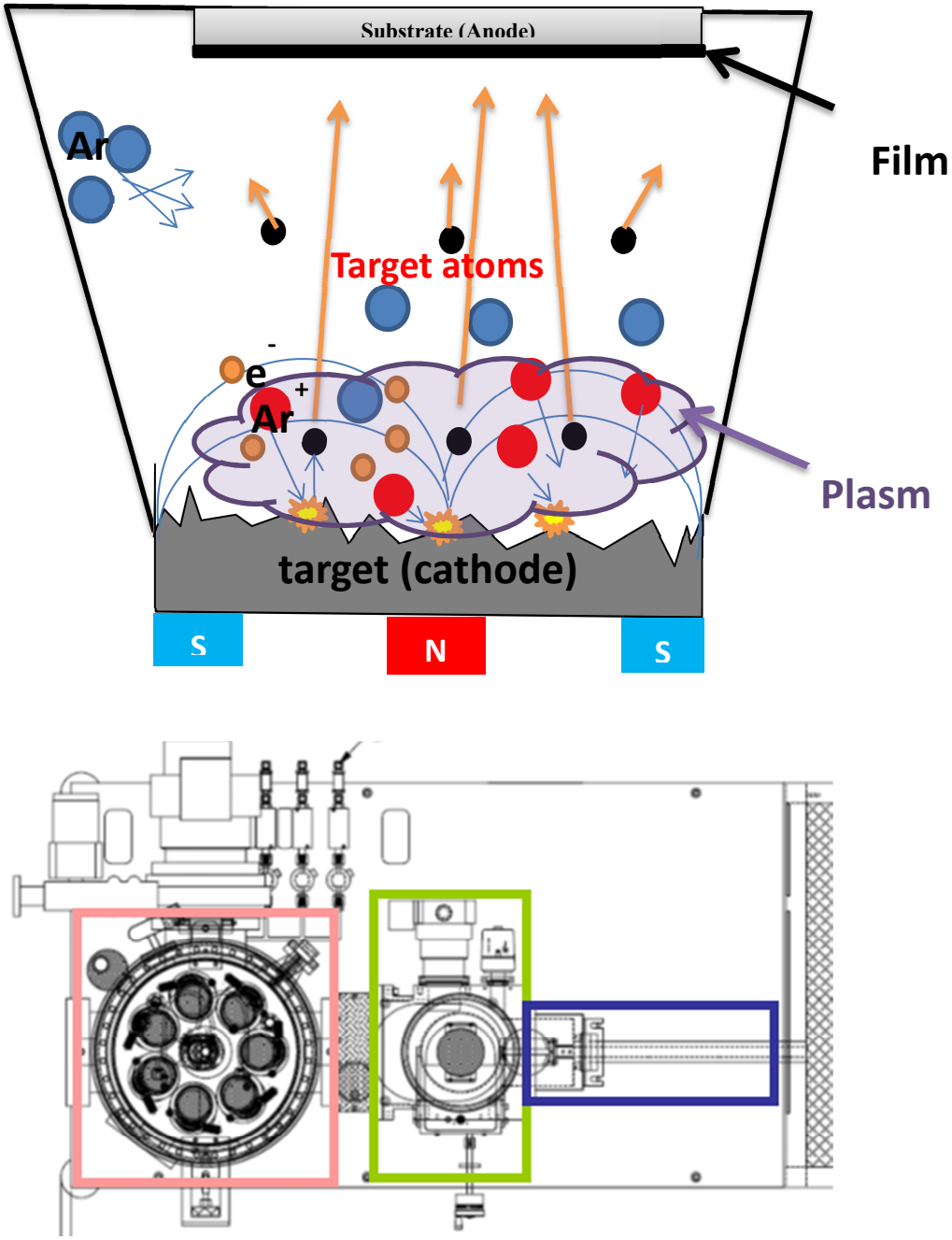

Figure 14: (a) Schematic of a sputter deposition source which shows the atomic interactions whichlead to deposit a thin film on the substrate. (b) Top down schematic of proposed sputter deposition system showing the deposition system chamber with a potential of 8 sources (pink square), the load lock (green rectangle), and the transfer arm (purple rectangle).

of the shutters on the sputtering sources allowing deposition of alloy films and heterostructures.

Sputter deposition is a well-established and industrially used technique, especially for complex heterostructures materials including metals, oxides, nitrides, carbides, etc. We have extensive long standing experience and interest in many of the different classes of systems, especially ferromagnets, antiferromagnets and metallic heterostructures, relevant to this thesis. In sputter deposition the sputtered atoms have relatively high kinetic energy which increases the surface mobility of the deposited atoms. The growth surface can also become bombarded by reflected neutral gas atoms, electrons and negatively charged ions that have significantly higher energy than the deposited atoms and provide the means to modify surfaces and interfaces. These energies can be tuned by the Ar sputter pressure, source power and source-to-substrate distance. Combined with heating the substrate there are numerous ways to tune the microstructural and interface properties of thin films.

3.3. Photolithography

Photolithography is a method to fabricate features and devices in dimensions as low as few hundred nanometers. This method is based on light (UV range) emission on a photosensitive chemical. The light goes through a photomask which includes the desired features, and finally the exposed resist is being developed. The light exposure changes the chemical properties of the resist, and based on the type of the resist either

the exposed or unexposed area is subsequently removed by a developer. The resists are divided on two main groups: positive and negative. The positive resist is chemically designed that the exposed area is dissolved in the developer and the unexposed area remains. The negative resist behaves opposite to the positive one, the unexposed area is dissolved and the exposed area would remain. The UV light emission is done by commercial mask aligner which provides the means to align the desired featured on top of the sample, and then both the sample and photomask are exposed to UV light. The wavelength of light mainly limits the resolution of the patterns that can be transferred.

The basic photolithography steps are shown in Fig. 15. The substrate is first spin coated with a resist to form a uniform coating. The thickness and uniformity of the resist can be controlled through the spin speed and time. In this thesis both the positive (S1818) and negative (NR9- 3000 PY) resists were used. The coated sample is baked (soft bake) to evaporate the solvent within the resist. The Karl Seuss MA6 mask aligner was used to align patterns and the combination of the mask and sample was exposed to the UV light with the wavelength range of 350-450 nm while the photomask and the sample were in hard contact. After exposure the sample is baked (hard bake) to remove the remaining solvents and harden the resist (this part only was used for NR9 resist in this thesis). After hard bake, the sample is soaked in a developer and the resist is developed.

At the end, based on the microfabrication process, the final pattern can be reached by deposition of metal and then lift off the excess resist or by using the resist

as a etch mask to etch the excess metal, and use acetone to remove the remaining resist (Fig.16).

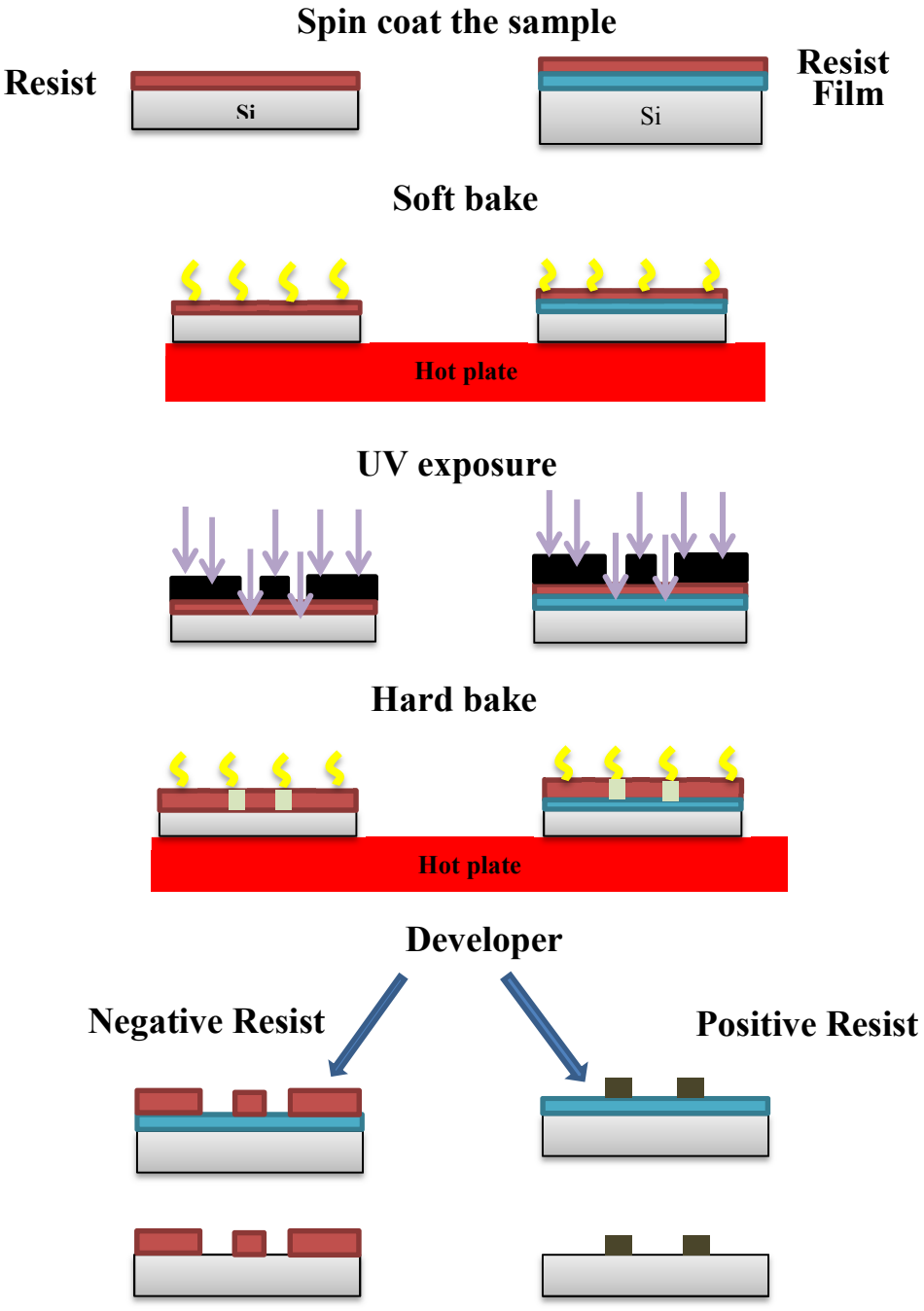

Figure 15: A typical photolithography steps and the difference results based on the positive and negative resist usage.

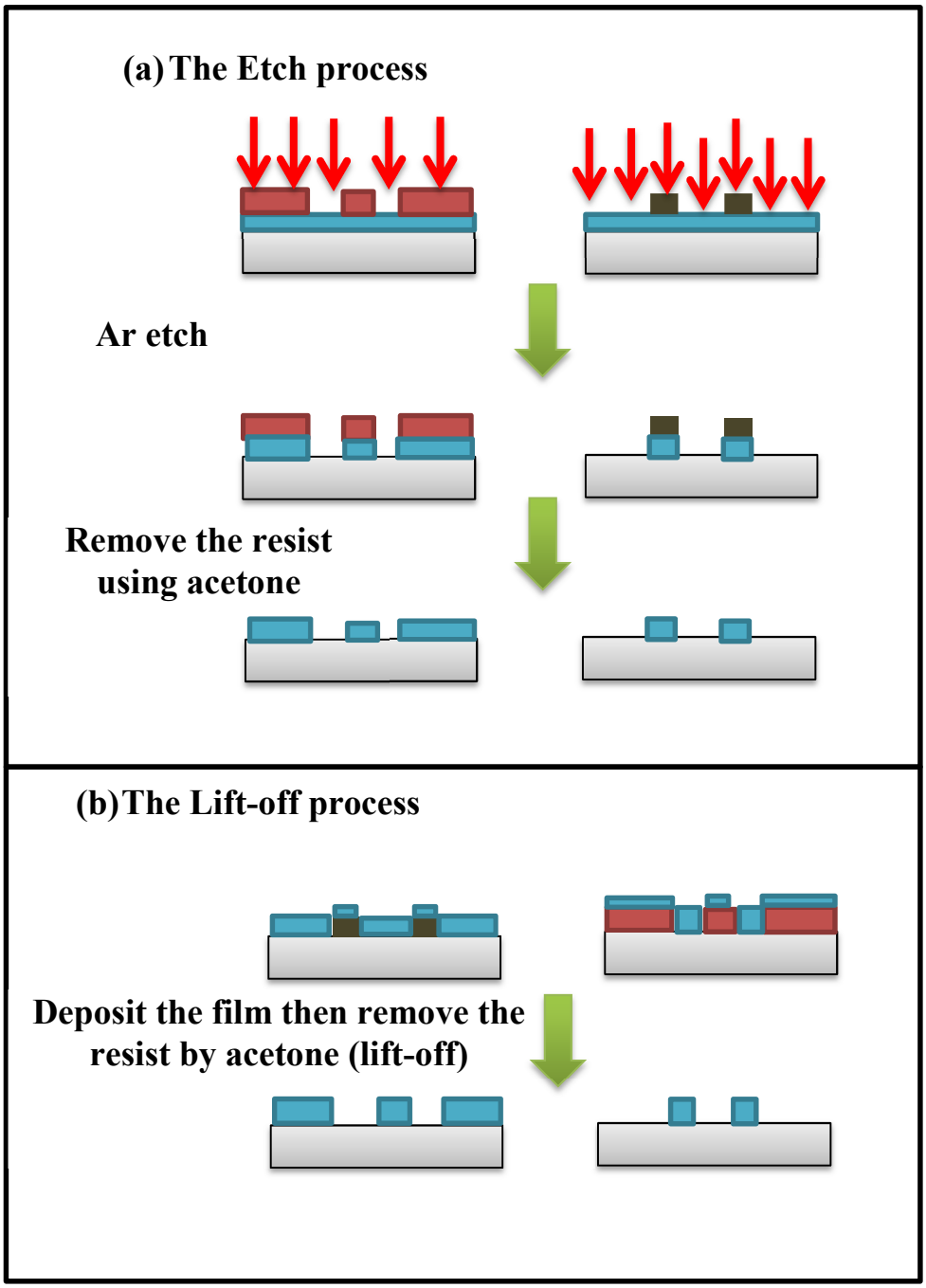

Figure 16: the post process of photolithography which shows two different processes: (a) etch process and (b) lift-off process.

3.4. Electron Beam Lithography

Electron beam lithography (e-beam lithography) uses focused electron beam to write patterns in to an electron sensitive resist. The resists that are usually used for this technique are PMMA (polymethyl mthacrylate, a polymetric material with formula of $(C_5O_2H_8)_n$) or HSQ (Hydrogen silsequioxane, inorganic compound with formula of $[HSiO_{3/2}]_n$). This technique is capable of creating sub-20-nm patterns. However, e-beam lithography is generally only suitable for patterning small areas and it is a very expensive and time consuming technique. This is because the patterning is done with a single electron beam and the features are patterned serially. As a result, usually this technique is combined with other techniques with high throughput such as self-assembly and Nanoimprint lithography which are going to be introduced in the following sections. In this thesis e-beam lithography technique was used to create templates for Nanoimprint lithography (sec. 3.6).

Steps to achieve a simple e-beam lithography pattern are shown in Fig. 17. First the sample is spin coated with a resist (PMMA or HSQ) and then an e-beam writer would write a pre-designed pattern using focused electrons into the resist. After the resist is exposed to the electrons, it needs to be developed (similar to photolithography), and finally the post processes either lift-off or etching is being done to achieve the desired patterned films.

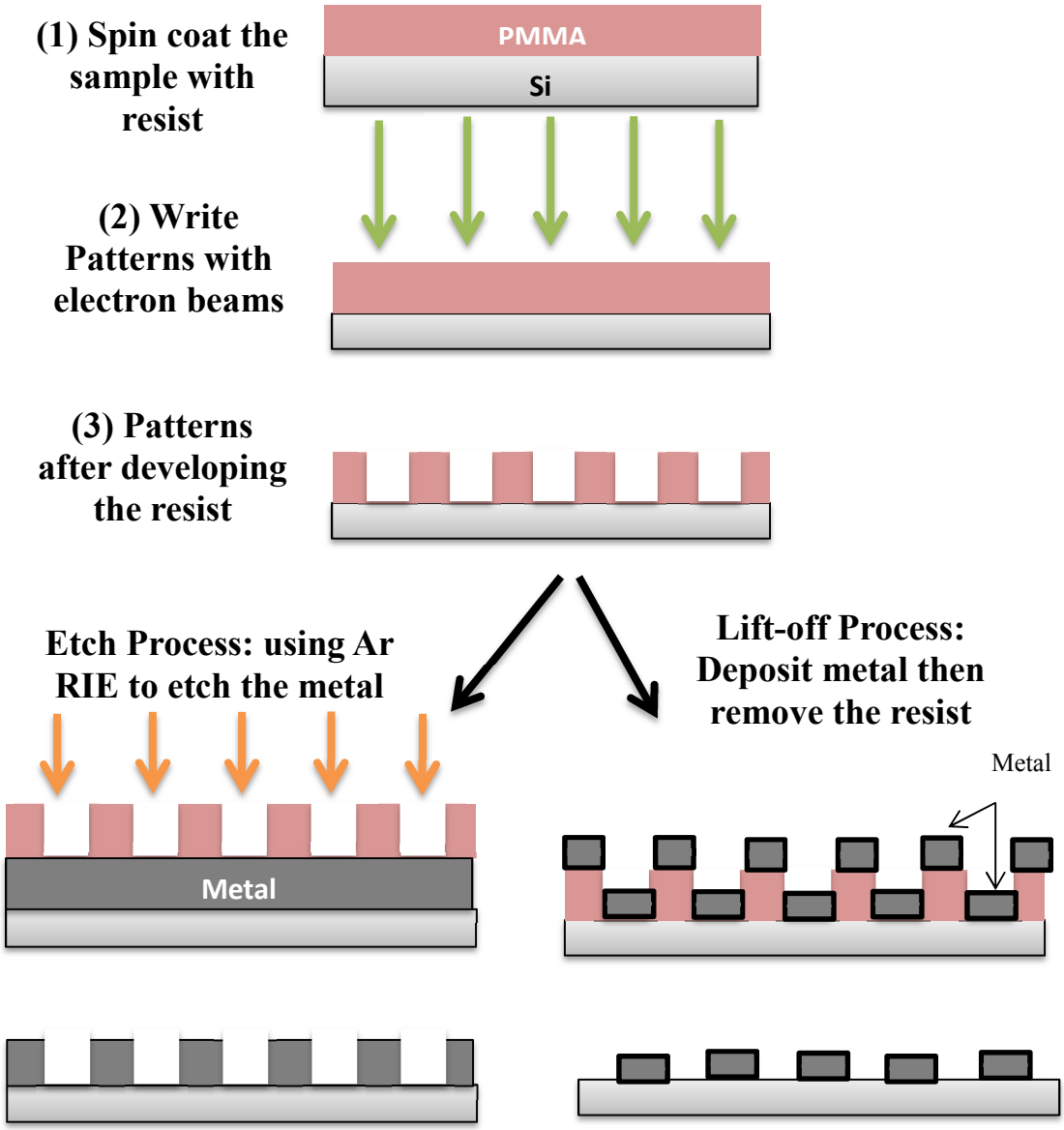

Figure 17: A simple e-beam lithography process steps.

3.5. Self-Assembly

Self-assembly technique utilizes synthesized polymers which form an array of ordered spherical structures on a surface when it is casted and annealed. The ordered polymer layer can then be used as etch mask to pattern a film. The main samples in this thesis are patterned by our collaborators in Toshiba laboratories using a self-assembly diblock copolymer method [41, 42]. Diblock copolymer is made out of two covalently joined polymers (*e.g.* Polymethylmethacryhate (PMMA) and Polystyrene (PS)) with chemically distinct properties.

A typical self-assembly technique is shown in Fig. 18. First the diblock copolymer being spin coated on the sample with a sputtered film (magnetic film) and then the substrate is annealed and spherical shaped PMMA is formed into a hexagonal lattice through phase separation in the PS surrounding film. The dot diameters and spacing can be tuned by varying the PMMA and PS molecular weight (smaller dot diameter is achieved with lower molecular weight). The surface layer of PMMA is removed by CF_4 reactive ion etching (RIE) and then the PS is removed by oxygen RIE which is chemically selective toward PS. The PMMA dots remain to be used as an etch mask to remove the excess magnetic layer by Ar milling and transfer the pattern to the magnetic film. For the samples in this thesis that were patterned through this method, the last step was modified to study the effect of etching. The samples

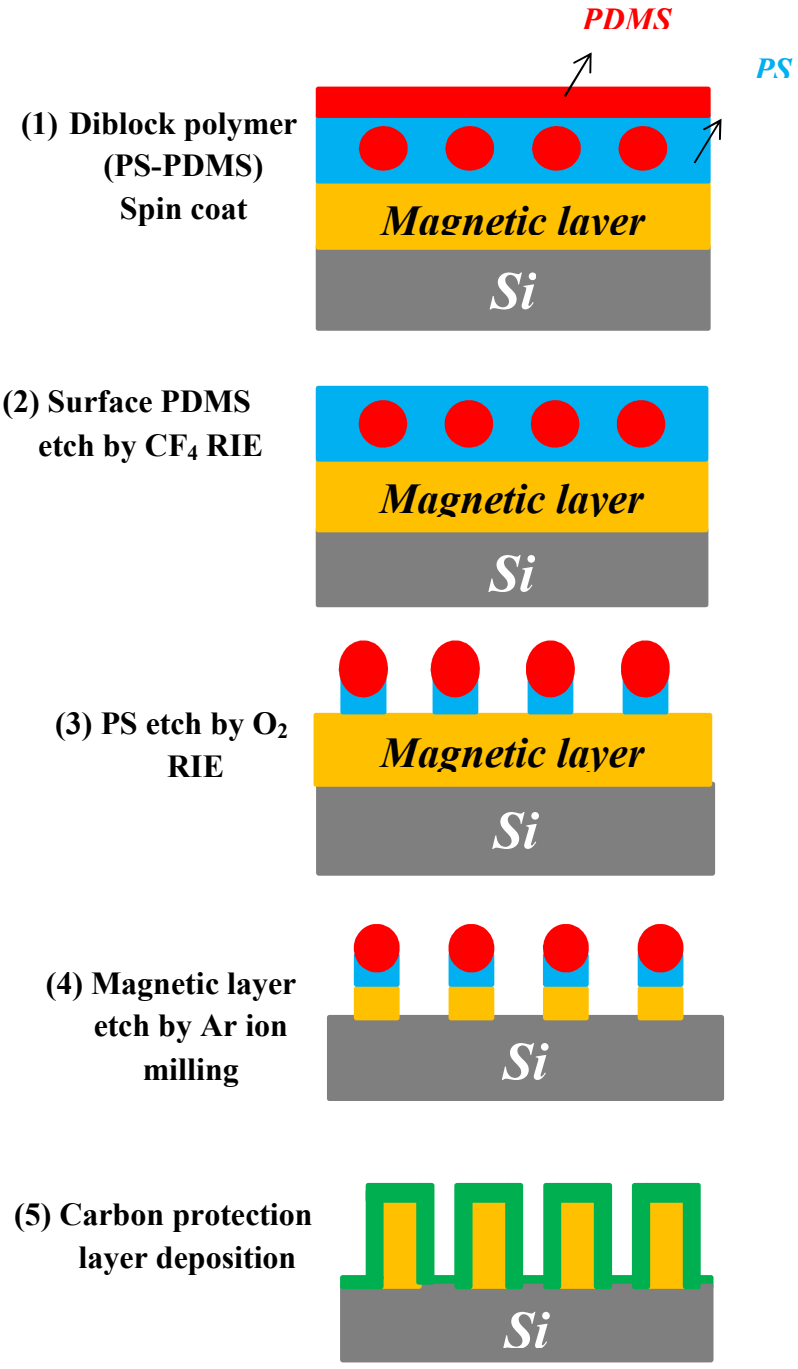

Figure 18: Fabrication method bit patterned media using di-block copolymer self-assembly.

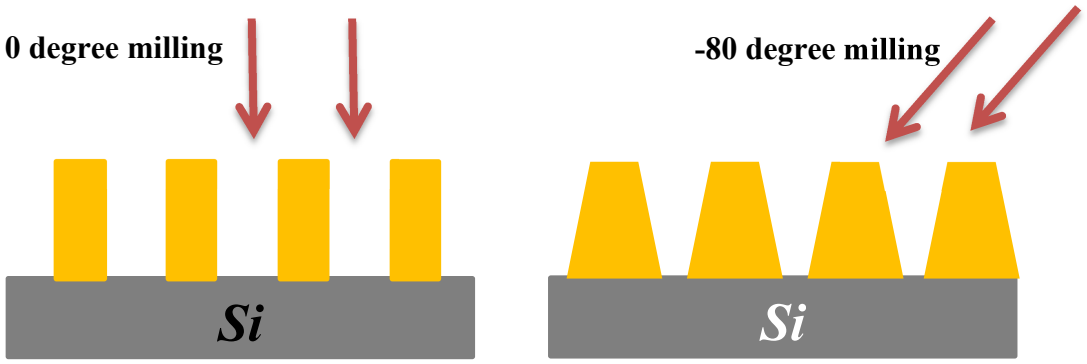

Figure 19: : the ion milling process at two different angles of 0 degree and -80 degreewhich resultsin a different shape of islands.

were etched by angled milling process at two angles of 0 and -80 degrees (Fig. 19).

A limitation with this method of patterning is that there is generally poor long-range order, defects, and distribution in dot's diameter (Fig.20). There are various methods under study to improve this technique, and the directed self-assembly is a promising method which uses pre patterned substrate which was patterned by other lithographic methods such as electron beam lithography. The patterns in substrate guide the formation of the arrays.

The magnetic properties of the samples that were patterned using self-assembly method is going to be discussed further in the following chapters.

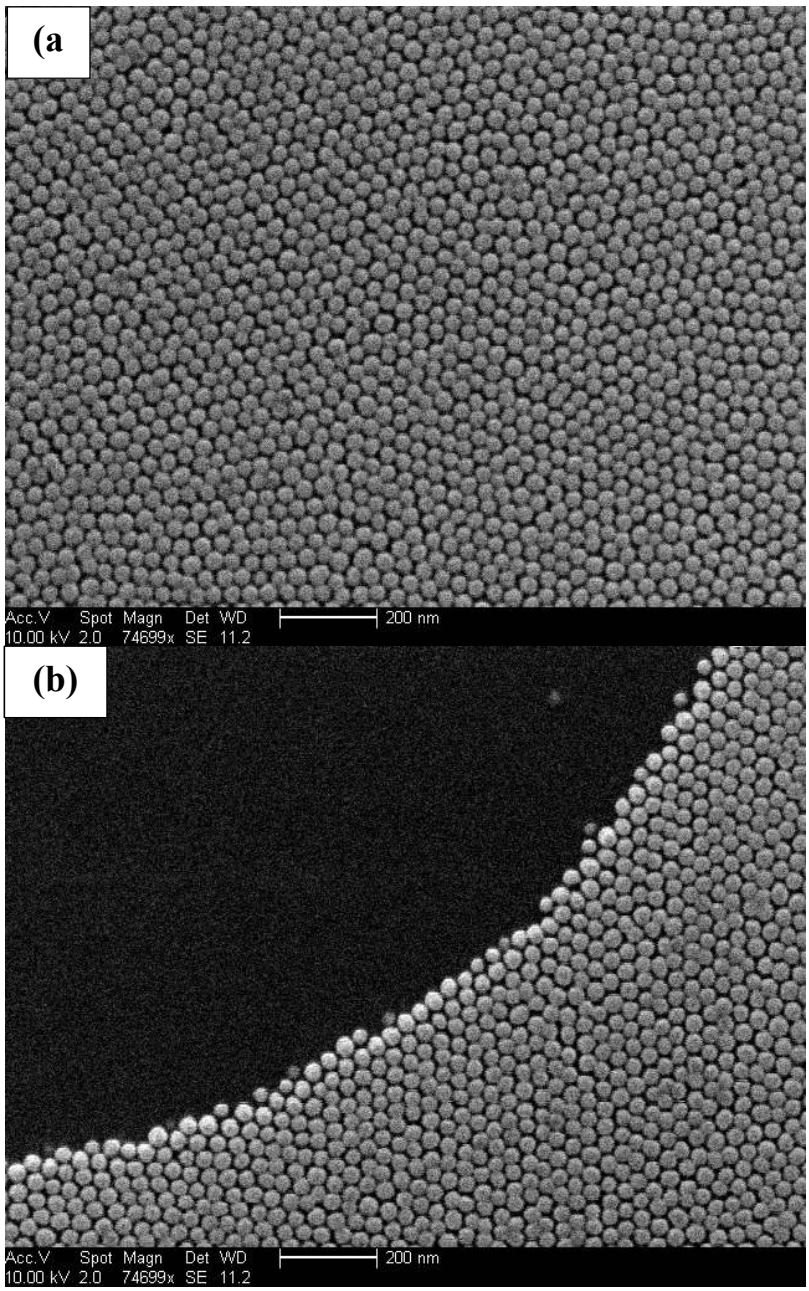

Figure 20: SEM image of a sample which is patterned by self-assembly method. (a) Shows the poor long range order, and (b) shows a defect, area without any dots, in the sample. 3.6. Nanoimprint Lithography

Nanoimprint lithography is a simple, reliable, and low-cost method with high throughput, and the ability to pattern sub-25-nm features. This technique uses a mold with patterns and transfers the patterns to the resist by mechanical compression of mold against the resist. Nanoimprint lithography is a strong candidate for fabricating patterned media, and the resolution of patterns is limited only by the mechanical strength of the resist [(43)].

The pattern master is made by other lithographic methods, among which e-beam lithography is popular. Thus the master template is very expensive, and as a result many copies are made from the master and imprint is being done using the copies to avoid damaging the master. The master templates for the work in this thesis which are 4-inch Si wafers are patterned using a Vistec EBPG5200 Electron Beam writer by the UCSD Nano3 staff, and the imprint is done on 4-inch wafers. The imprint processes that are done to create magnetic pattern islands are divided in 4 steps:

1) Mold/ Stamp fabrication

2) Sample wafer preparation

3) Imprint

4) Etch process

This method was used to pattern sample for MAMR experiments as discussed in Chapter 6.

3.6.1. Mold/Stamp Fabrication

The master mold is usually very expensive, and to increase the lifetime and imprint quality, it is needed to be protected from any defects and contaminations. As a result, usually copies (stamps) of the master are being made and those were used for imprinting. We used two different Polydimethylsiloxane (PDMS) materials based on the feature sizes that needed to be generated, and glass wafers were used as stamp carriers. The steps are explained below for both PDMS materials, but first it is needed to surface treat the master.

Surface treatment: The goal of this step is to chemically treat the surface of the master to be non-sticky for the process of the stamp making. This help the separation step, which master and stamp get separated, by minimizing the friction and avoids damaging patterns. The master template was vapor treated with surfactant and H_2O which coat the surface by a low surface energy (anti-adhesive) layer.

Ordinary PDMS (Fig. 21): For patterns with dimensions larger than 50-nm diameter and 100-nm pitch, the regular PDMS material was used. First a photoinitiater is mixed

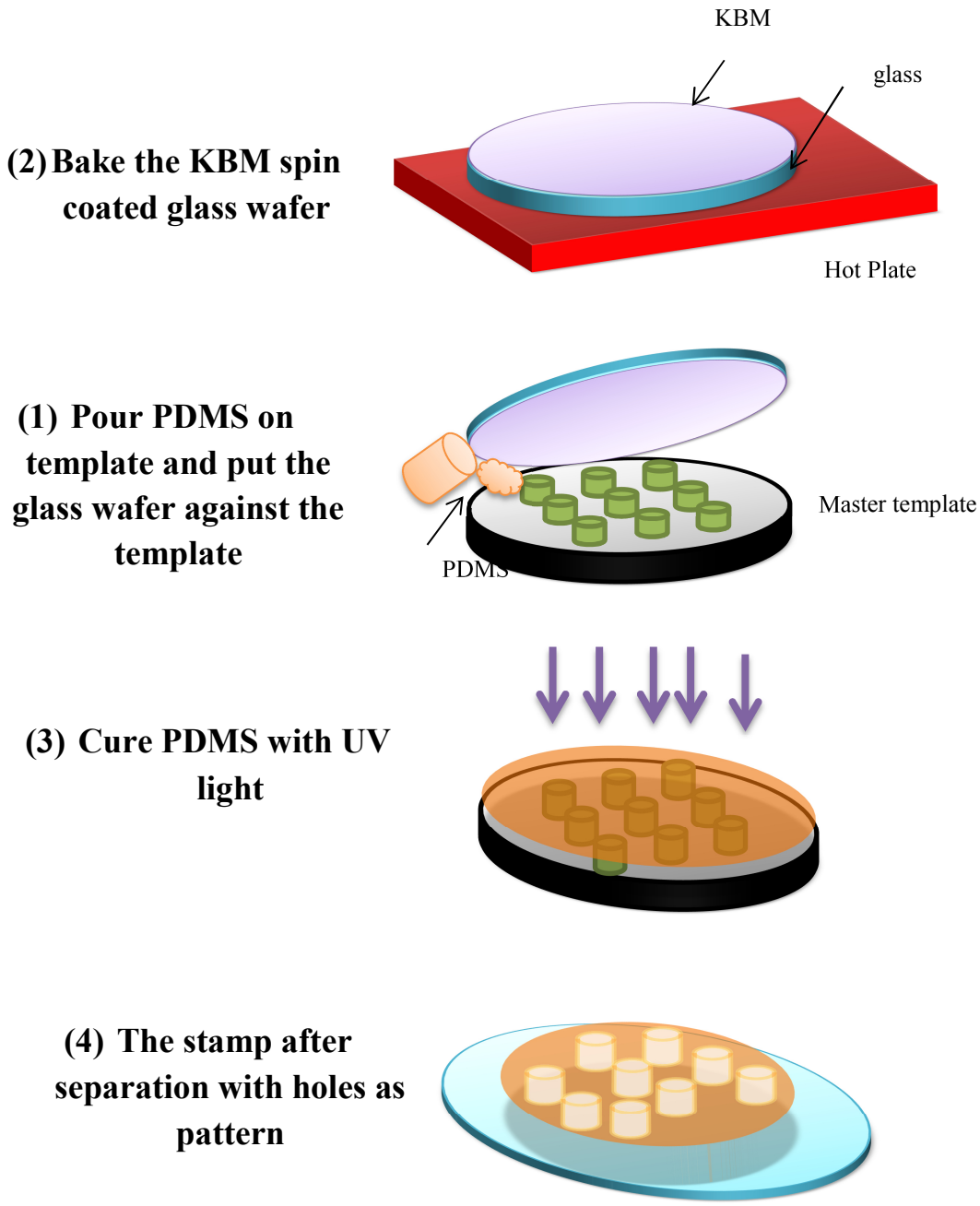

Figure 21: A typical stamp fabrication process using PDMS for Nanoimprint lithography

with PDMS to make it UV sensitive. A 6-inch glass wafer (stamp carrier) is spin coated with 1ml of KBM (silane coupling agent) and baked to form an adhesion layer for PDMS to be glued to the glass. The prepared PDMS material is poured on the surface treated master template then the prepared glass wafer with KBM side down is put against the template and PDMS as squeezed out fill the pattern area. This step should be done carefully to avoid trapping any air bubble which would influence the quality of imprint. After the PDMS liquid covered the master evenly, then the whole unit is UV cured and the PDMS is hardened. The last step is the separation of the glass wafer from the template. The thickness of the stamp can be controlled by amount of the PDMS and the spacer between the glass carrier and the template.

X-PDMS Mold: For sub-50-nm patterns and smaller pitch sizes, it is needed to use modified PDMS material with better mechanical strength. X-PDMS is modified PDMS that is developed by PHILIPS for sub 50-nm features. The surface treated master template is spin coated by X-PDMS and baked to harden the layer then the X-PDMS intermediate material is spin coated and the template is baked in the oven for at least 15 hours or more (for better resolution baking can be extended to 2-3 days). After the template is ready, a soft PDMS material is used to connect the 6” glass wafer to the template. This step is similar to the ordinary PDMS method, the PDMS material is poured on the template and the glass wafer is put against the template which causes the PDMS to squeeze out. The combination of the template and glass while are placed against each other is baked overnight (at least for 15 hr.). Then the glass wafer is separated from template and the stamp is ready for imprint.

3.6.2. Wafer Preparation

Two layer resists method are used in this step. The underlayer's purpose is to create a good adhesion between the imprint resist and the sample wafer to ensure no damage to the patterns at the separation step of imprinting. The top layers used here are UV sensitive and have low viscosity. The resists that are used are ULP/UVP and PMMA/Sol-Gel. Both sets of resist are suitable for high-resolution samples; however, due to their different characteristic, they behave differently in post imprint process (etching or lift-off). The ULP/UVP set is preferable for lift-off process since UVP is not good as an etch mask as it doesn't have good selectivity in Ar milling. On the other hand, sol-gel is a good etch mask resist since it behaves like SiO_2 after UV cure. However, since sol-gel is a porous material, heating during the UV cure and etch process causes the pours to shrink and as a result the dimension of the patterns changes.

For both sets of resists, first the underlayer is spin coated on the sample wafer, and then the top layer is spin coated on the sample.

3.6.3. Imprinting

For imprinting (Fig. 22) an EVG 620 was used. The mold and the sample are first being aligned and then they are pressed at room temperature against each other by a vacuum which force the resist to form the patterns. While the mold and the sample

are pressed against each other, both are exposed to the UV light. The UV hardens the imprint resist and the patterns are formed on the sample and the last step is the separation of the mold and the sample. Figure 25 is an example of SEM image of imprinted holes, and Fig. 26, is an example SEM image of pillars.

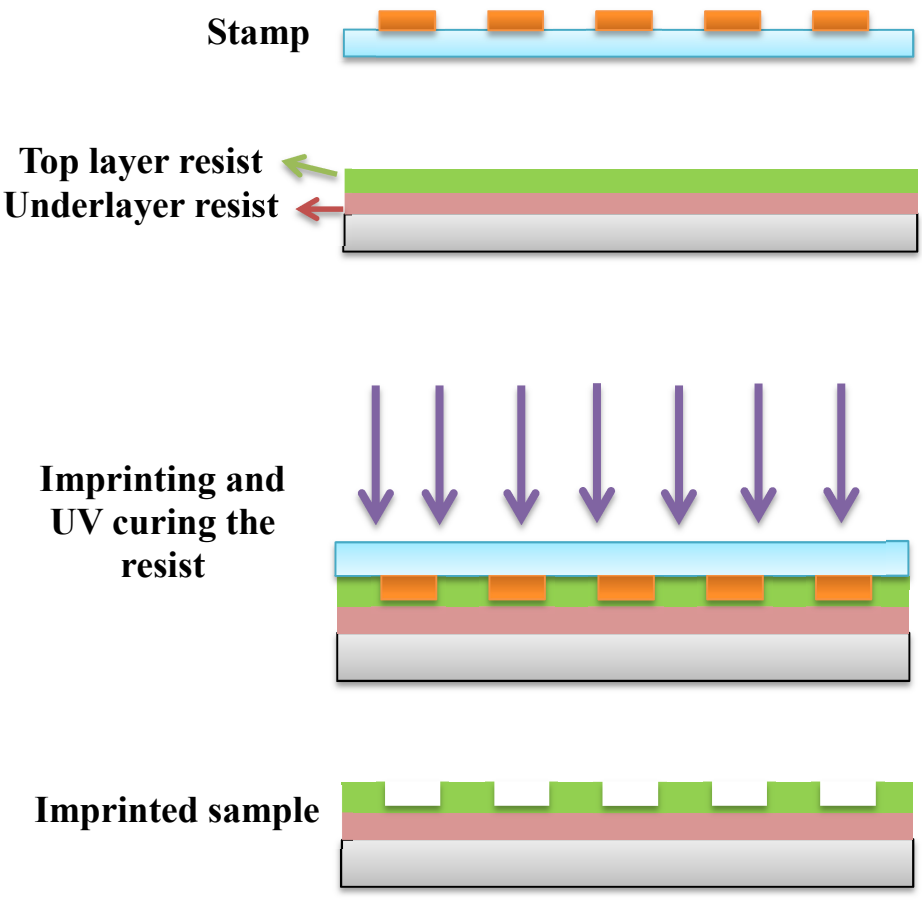

Figure 22: Simple Nanoimprint process using two layer UV sensitive resists.

3.6.4. Post processing

Both lift-off (Fig. 23) and etch processes (Fig. 24) have been done to create patterns. For the ULP/UVP set, the excess resist is removed. The UVP excess layer was first etched by CF_4 and O_2 and then the ULP layer is etched by Ar and O_2 (Fig.23). Then, the metal was sputtered on the patterned substrate, but since the sputtering as it was mentioned in section 3.2, is being done at an angle and due to the size of the holes, the metal either didn't fill the holes completely or the walls effect was very pronounced which caused the lift-off process to be unsuccessful (Fig. 27). However, if more directional metal deposition methods such as evaporation are used, the lift-off problem can be solved (Fig. 28).

For the PMMA/Sol-Gel set, the pillars are made on the Sol-Gel layer and the excess Sol-Gel layer is removed by SF_6 and O_2. The PMMA layer in the next step is removed by Ar and O_2, and in the end the magnetic layer is removed by Ar milling.

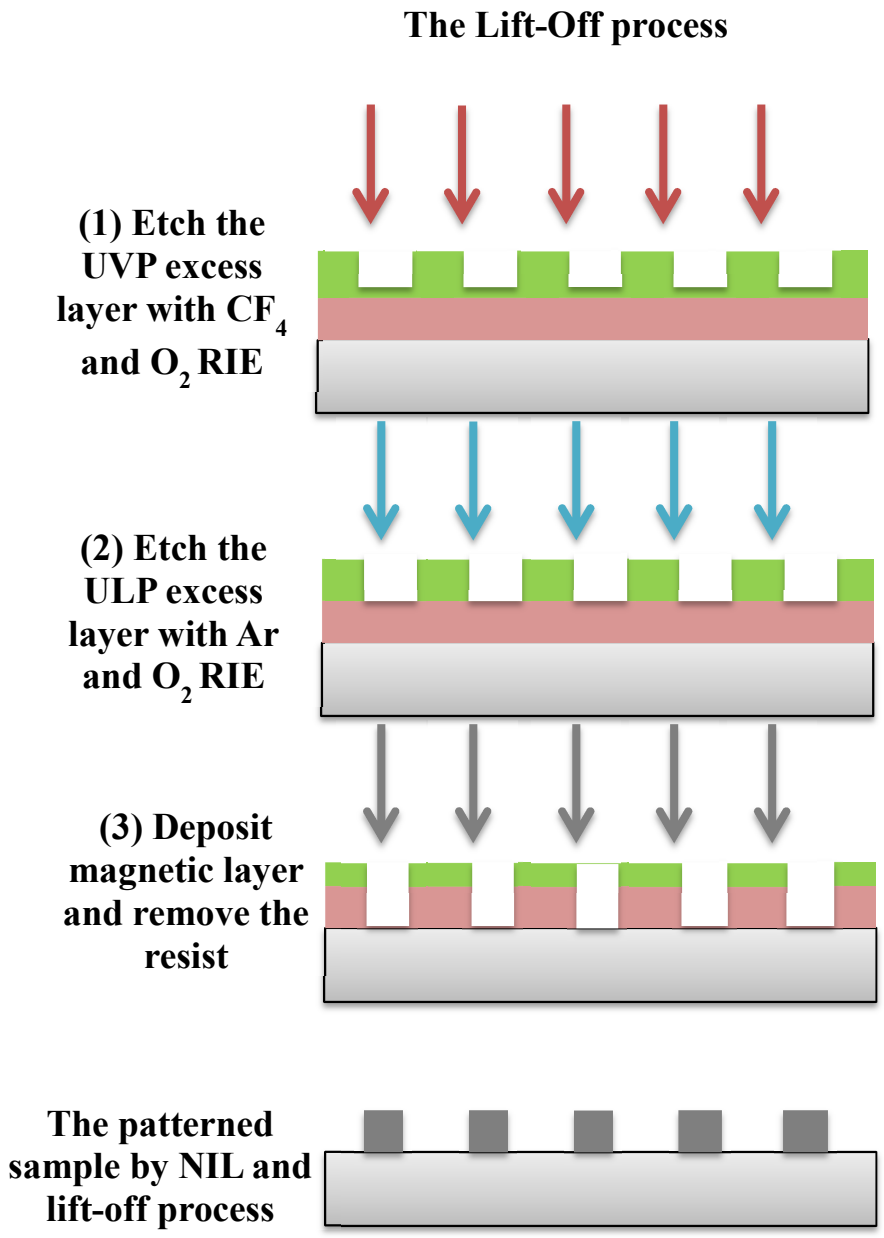

Figure 23: The lift-off process is shown after the sample is imprinted. For the etch process the ULP/ UVP resists are used.

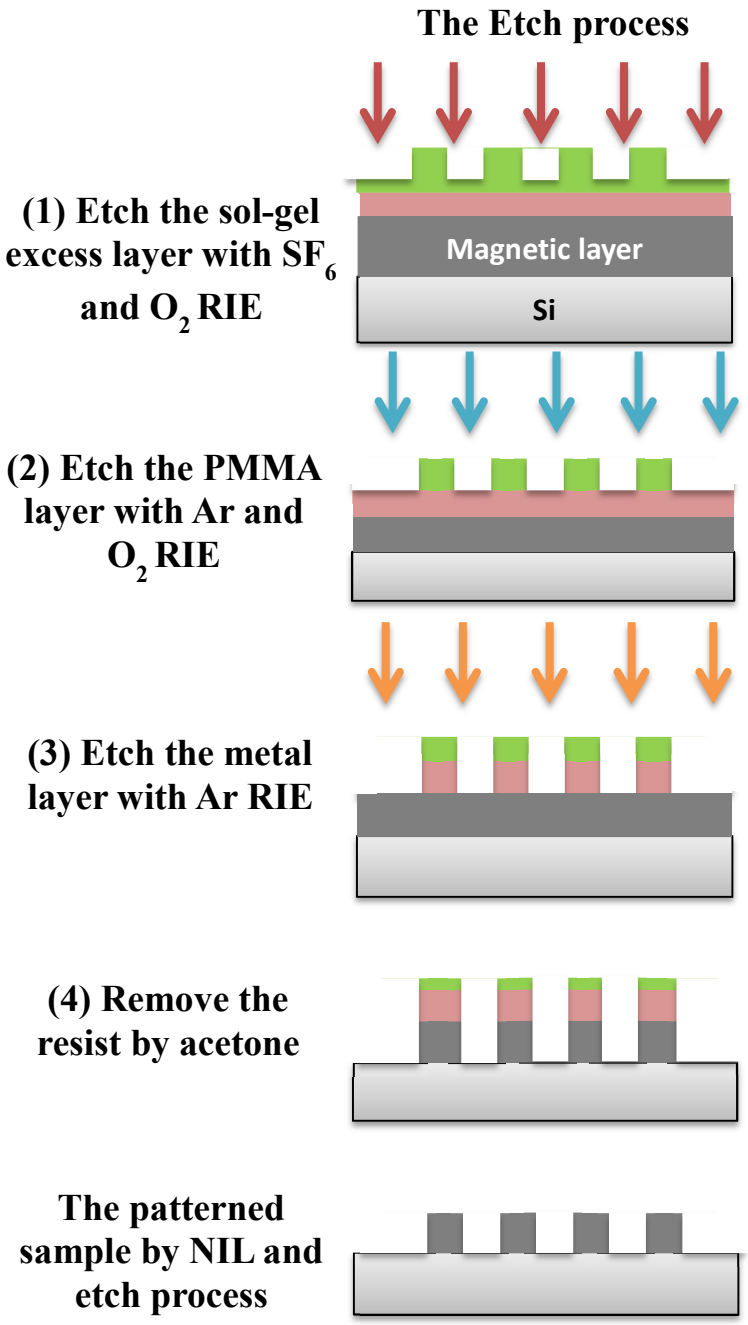

Figure 24: The etch post process is shown after the sample is imprinted. For the etch process the PMMA/ Sol-gel resists are used.

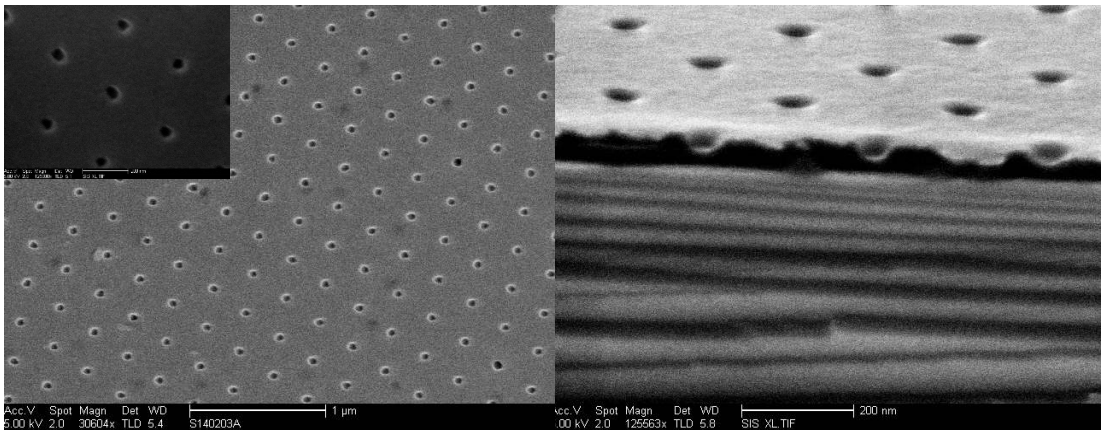

Figure 25: (a) SEM image of imprinted holes with average diameter of40nm and 250nm spacing. (b) The SEM cross view image of holes with average depth of 41nm.

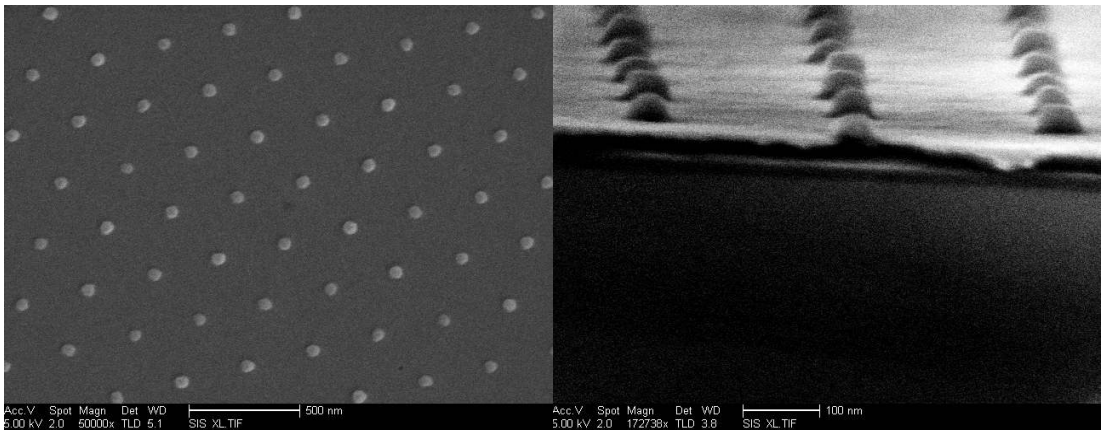

Figure 26: (a) SEM image of imprinted pillars with average diameter of 50 nm and 250nm spacing. (b) The SEM cross view image of pillars with average height of 40nm

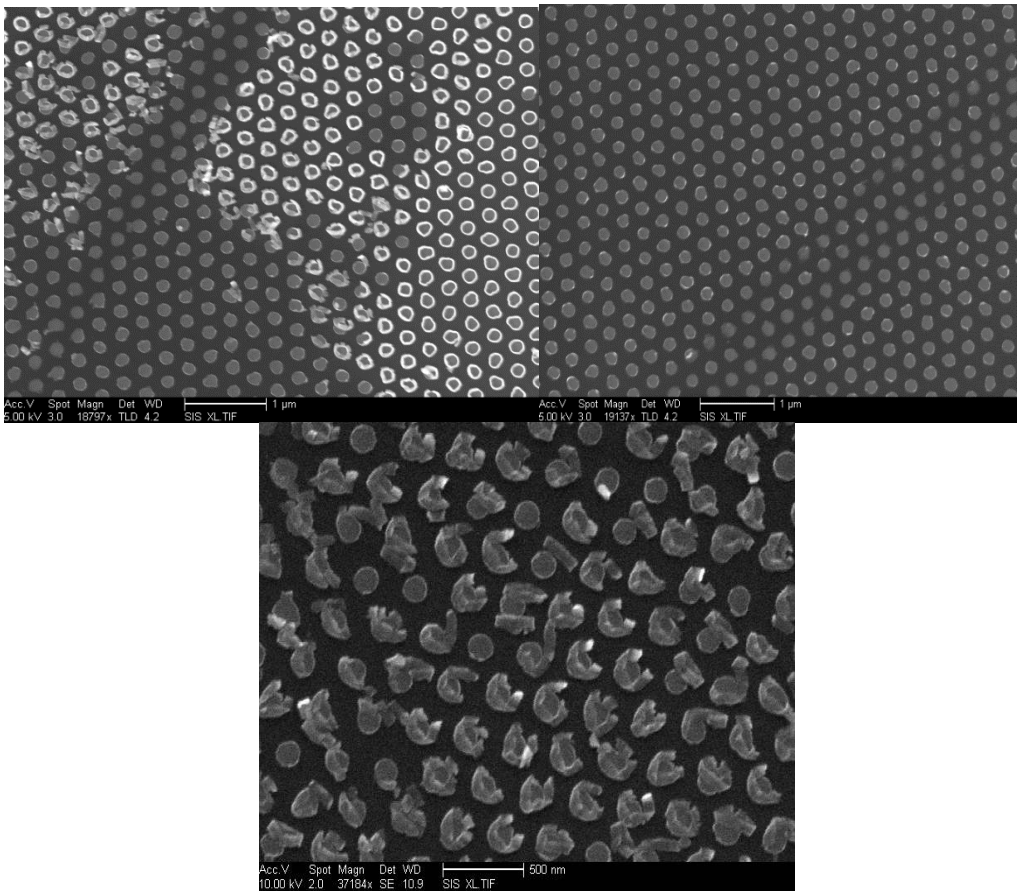

Figure 27: The SEM images show the result after DC sputtering metal into holes and lift-off. . Due to sputtering at the angle the defects are caused by depositing into the walls of the holes

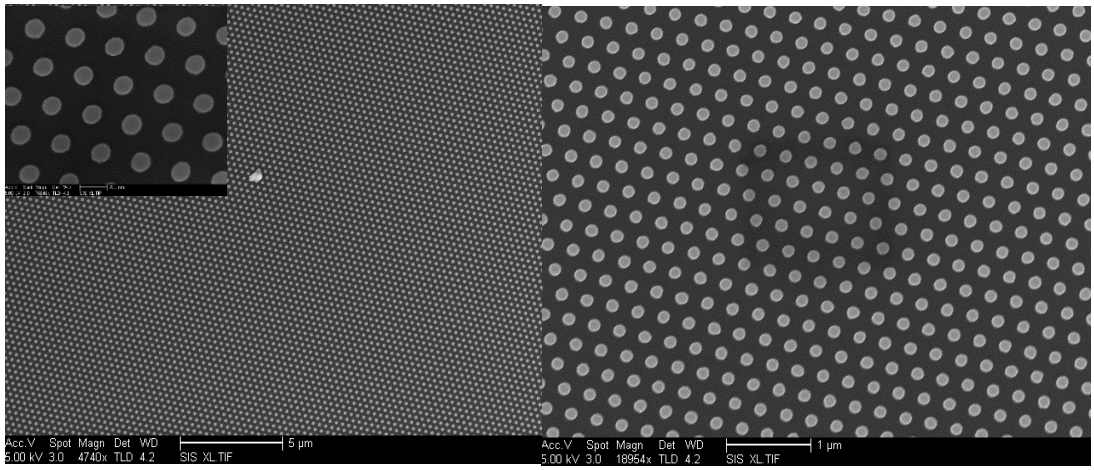

Figure 28: The SEM images shows the result of post process of lift-off after evaporating metal into the holes (a directional deposition method)

Chapter 4: Bit-Patterned Media with Perpendicular Composite Structure

4.1. Perpendicular Magnetic Anisotropy in [Co/Pd] Multilayers

Thin films with perpendicular magnetic anisotropy (PMA) have their magnetic easy axis normal to the film plane. In thin films the competition between the shape and surface anisotropy defines the easy axis either to be in-plane or out-of-plane of the sample. Due to a great interest in this topic a large variety of materials, alloys and structures have been studied such as Co-Cr alloys [44] and FePt [45] for granular magnetic media, Co/Pt or Co/Pd multilayers[46, 47, 48] for bit-patterned media and reference layers in spintronic devices and CoFeB/MgO[49] for spintronic devices. Here we will focus the discussion on Co/Pt and Co/Pd multilayers. Magnetic anisotropy arises from the spin-orbit interaction and the coupling of the orbital moment to the lattice. As such magnetic anisotropy reflects the symmetry of the lattice. For thin films the anisotropy can arise both from the volume of the films (K_V) and from the broken symmetry of the surface (K_S) which provide an easy axis that it normal to the surface. The effective PMA of thin films (K_{eff}) can be calculated through a weighted average anisotropy of the system (as long as the thickness is less than the exchange length) which is expressed as:

$$K_{eff} = K_v + \frac{2K_s}{t} \tag{22}$$

The volume term is a combination of the magneto-crystalline anisotropy (K_C) and the thin-film shape anisotropy ($-2\pi M_S$). For many cases the shape term will dominate. The form of the interface contribution in Eq. (22) assumes from two interfaces of the magnetic film contribute equally. However this is easily generalized

to have the top and bottom interfaces having distinct contributions. The measured K_{eff} for a series of Co/Pd multilayers is shown in Fig. 29.[42] In this case the Pd thickness was held constant at 1.1 nm and the Co layer thicknesses (t_{Co}) was varied from 0.2 to 2.0 nm. Figure 29 is plotted as $K_{eff}*t_{Co}$ vs. t_{Co} where the positive K_{eff} refers to perpendicular anisotropy and the negative K_{eff} refers to in-plane magnetic anisotropy, the slope of the curve is K_V and the intercept of the vertical axis is $2K_S$. As seen the transition from in-plane to perpendicular anisotropy occurs for a Co thickness of 1.2 nm.

In Co/Pt and Co/Pd multilayers the thin layers of Co are ferromagnetically exchange coupled through nonmagnetic layers of Pd or Pt forming a ferromagnetic film. The nature of this exchange coupling is due to direct ferromagnetic exchange from an induced magnetic moment in Pt and Pd at the interface with the Co and RKKY interactions.

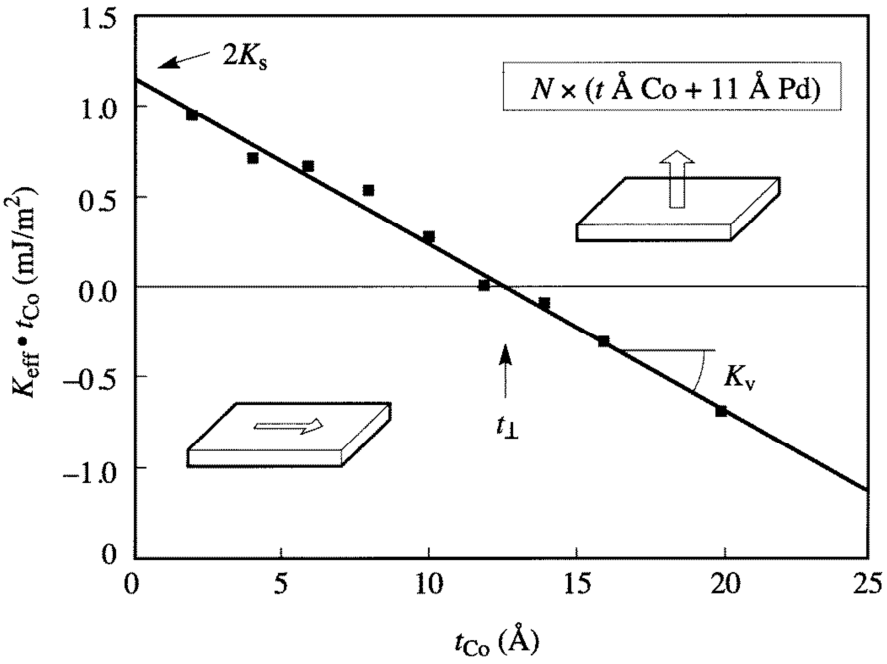

Figure 29: The effective anisotropy times thickness of Co layers vs. the Co thickness while the Pd thickness is kept constant. The Co thicknesses for which the multilayer has perpendicular anisotropy is determined [46].

To optimize the PMA in this class of magnetic multilayers, a series of Co/Pd samples were grown using an AJA magnetron sputtering tool with the base pressure of less than 5×10^{-8} Torr, and an Ar sputter pressure of 3mTorr. Each gun deposition rate is calibrated using X-ray reflectivity technique to measure the thickness of a deposited calibration thin films. The multilayers are grown computer controlled sequential opening of the sputter gun shutters. The sample structures are SiO_x / Pd (5nm) / [Co (x) / Pd (0.7nm)]$_6$ / Pd (2nm). A Pd layer is used for both the buffer and capping layers in addition to as a nonmagnetic spacer in the multilayer. The buffer layer helps PMA by introducing texture to the film. The Pd thickness in the multilayers is kept constant at 0.7nm, but the Co thickness is varied, x = 0.2, 0.3, 0.4, 0.5, 0.6, 0.7 nm.

The magnetic hysteresis of these samples are measured using vibrating sample magnetometer (VSM) both parallel (in-plane) and perpendicular (out-of-plane) with respect to sample's surface. Figure 30 shows the in-plane and out-of-plane loops for Co thickness of x = 0.2 nm. The comparison between the in-plane and out-of-plane loops confirms the PMA in the sample. The samples with various Co thickness hysteresis loops are measured with VSM and compared (Fig.31). As Co thickness increases the coercivity of the out-of-plane loops (Fig.31 (a)) decreases since the shape anisotropy increases and as a result the in-plane susceptibility increases (Fig. 31(b)).

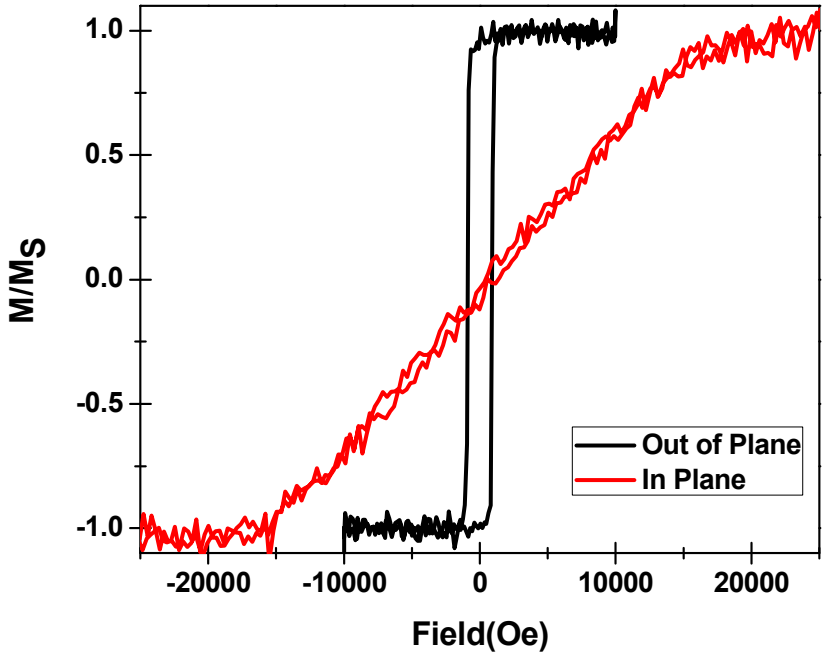

Figure 30: The magnetic hysteresis loops for Pd (5nm) / [Co (0.2nm)/ Pd (0.7nm)]$_6$ / Pd (2nm). in both in-plane and out of plane configurations in-plane susceptibility increasesIt is concluded that sample with x= 0.2 and 0.3 nm has the strongest PMA.

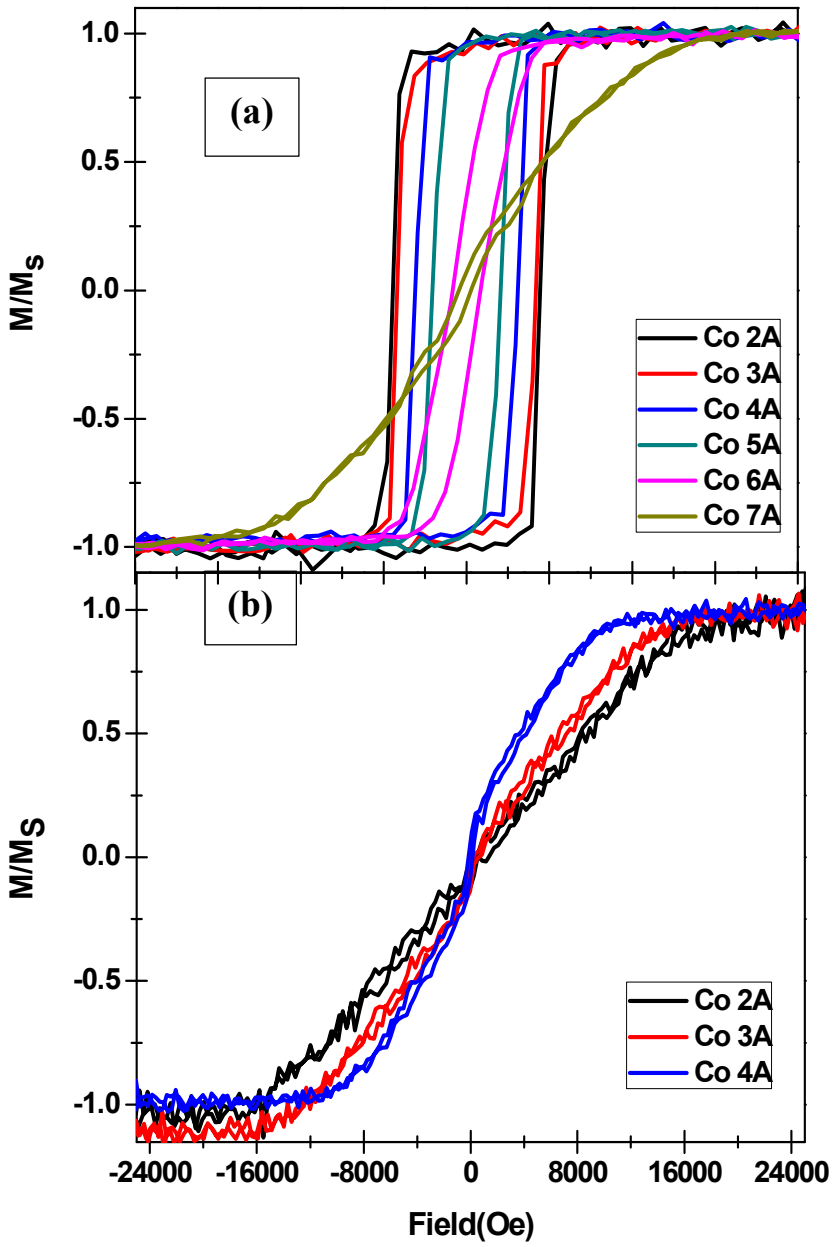

Figure 31: (a) shows the out of plane loops for the different Co thickness that is measuredby VSM. As Co thickness increases, the PMA decreases. (b) Shows selected in-plane loops which confirms as Co thickness increases the in-plane susceptibility increases.

4.2. Exchange Coupled Composite Structure

Magnetic exchange-coupled composite structures, in their simplest form, consist of two exchange-coupled regions of magnetically hard and soft sections. The magnetically hard region has strong PMA with its easy axis is perpendicular to the film surface. This section's high anisotropy ensures thermal stability of the structure. The soft region with lower anisotropy, works against the hard layer, and helps to decrease the switching field for writing the structure with an external magnetic field. These two regions are exchange coupled at their interference. When an external magnetic field is applied to such structure, the reversal domain nucleates in the soft region and it propagate to the hard layer thorough the interfacial exchange and cause incoherent switching which decrease the switching field of the structure[24, 50,51,52]. If designed correctly composite structure can lower the write field more than the thermal stability of the media. R.H. Victora, defined a figure of merit for magnetic recording media [53]:

$$\xi = \frac{2\Delta E}{M_S H_S V} \tag{23}$$

where ΔE is the energy barrier, M_s is the average saturation magnetization, H_s is the switching field, and V is the volume of a grain. The ratio is $\xi \sim 1$ for the ideal conventional perpendicular recording media. However, ξ can theoretically approach to 2 or 3 for composite structures which provide a chance to decrease the grain volume while increase the anisotropy which would not challenge the writability of the media. Figure 32 shows a simple schematic of a composite structure. M_1 and M_2 are the saturation magnetization of soft and hard layers respectively. It is shown that the ratio

of $\frac{M_2 t_2}{M_1 t_1}$ has a significant influence on the ξ, where t_1 and t_2 are the thickness of the soft and hard layer [53]. The value of the figure of merit is higher if the saturation magnetization ratio be smaller. The anisotropy constant of soft and hard layers are K_1 and K_2 respectively. The ratio of $\frac{K_2}{K_1}$ is not very significant as long as the ratio is greater than 30[53].

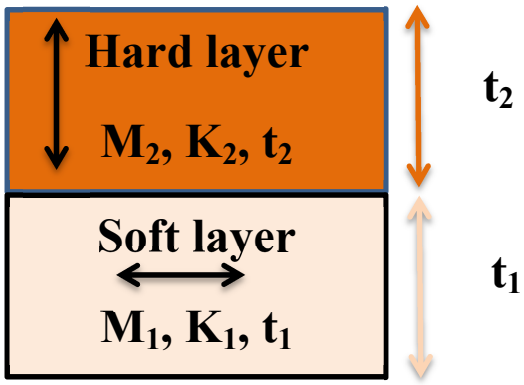

Figure 32: A typical structure of magnetic composite structure is shown, where a hard magneticlayer is exchange coupled to a soft layer. M is magnetization, K is anisotropy constant, t is the thickness, and the indices 1 and 2 refer to soft and hard layer respectively.

4.3. Bit-Patterned Media with Composite Structure

Bit-patterned media (BPM) is the top candidate for magnetic recording media to extend the areal density beyond what is achievable by PMR[35,54,55,56,57]. Also it is mentioned in the previous section; the complex heterostructures like exchange-coupled composites (ECC) media provide unique magnetic properties such as reversal mechanism, and it can be a good candidate to replace the conventional perpendicular

media. In this thesis the ECC structure is implemented in BPM to explore their properties for potential applications in the magnetic recording industry and potentially in magnetic memory applications such as magnetic random access memory (MRAM).

We fabricated magnetic thin-film heterostructures of the structure Ta (2_{nm}) / $[Co(0.25_{nm}) / Pd(y)]_5$ / Fe (x) / $[Pd(y) / Co(0.25_{nm})]_5$ / Pd (1_{nm}) (Fig. 33) , where the thicknesses of Fe, x = 1, 1.5, 2, 4, 6 nm and Pd, y = 0.7, 0.9 nm are varied at Ar sputtering pressure of 3mT onto SiO_x coated substrates. In this structure, [Co/Pd] multilayers have perpendicular anisotropy (section 4.1) and behave as the magnetically hard region. The layer of Fe, however has high M_S (and negligible magneto-crystalline anisotropy) and therefor much higher shape anisotropy (since it scales as M_S^2) and acts as the magnetically soft region. The Fe layer is sandwiched between the multilayers and it is exchange coupled to the hard regions from two sides through the Pd inter-layers (Fig. 33). While slightly more complex than the structure shown in Fig. 32 the basic concepts hold. The magnetic hysteresis loops of the films with thicker Fe as measured by VSM are shown in Fig. 34. For thick Fe layers there are two components to the hysteresis loop. At low fields the Co/Pd layers saturate and then the Fe layers requires significantly higher fields to saturate the film. For the 6-nm Fe sample the saturation field is consistent with the expectation for the shape anisotropy of a Fe thin film. However, as the Fe layer thickness decreases the saturation field decreases as the exchange coupling of the Co/Pd layers to the Fe layer helps to compensate the demagnitization field. Further it is shown by tuning the Pd

thickness from 0.9 to 0.7 nm, the coupling of the Fe layer to the Co/Pd layers becomes stronger.

For the thicker Fe film results in Fig. 34 we apply a simple model to the Fe layer for the purpose of determining the interface exchange energy. In this model, one assumes that H_{ex} arises from the exchange coupling at each Fe interface, formulated as follows:

$$4\pi M_s - H_{ex} = \frac{2J_{exchange}}{M_s d_{Fe}} \tag{24}$$

The left side of Eq. 24 corresponds to the saturation field in Fig. 34. Assuming bulk Fe M_s, one obtains rather large, out-of-plane exchange energies for each of the samples as indicated in Table 1.

Table 1: Analysis of data shown in Fig. 34 where the effective. exchange parameter across the Pd layer is extracted by Eq.24.

Sample	Saturation field (Oe)	J_{exch} (erg/cm^2)
d_{Fe} = 2 nm	3,760	3.0
d_{Fe} = 4 nm	10,700	3.6
d_{Fe} = 6 nm	14,100	3.7
d_{Fe} = 2 nm + $Pd_{0.9}$	5,870	2.3

The strong ferromagnetic coupling across the Fe layer is consistent with the properties of Pd which is nearly ferromagnetic with an anomalously large susceptibility. This results in the Pd atoms at the Fe/Pd interface being strongly polarized by the Fe atoms. This polarization has been observed as an enhanced magnetic moments and strong ferromagnetic interlayer coupling for Pd thicknesses of 4 atomic layers or less. Note that from Fig. 34 and Table 1 that modifying the Pd thickness adjacent to the Fe provides additional tunability to the interfacial exchange. The values for the coupling across the 0.7-nm Pd layer are consistent with previous studies of domain wall states in Co/Pd multilayers.

For applications in BPM the purpose of having Fe layer at the center of the stack and being coupled at two interfaces is to have greater variability of Fe thickness while maintaining the PMA of the whole stack. Having the Fe layer in the center of the stack has another advantage in BPM structures as it separates the two hard layers and may help improve the switching field distribution of the structures if the

anisotropy distributions of the two layers are statistically independent. The samples with the Fe thickness of x= 1, 1.5, and 2nm, and Pd thickness of y=0.7nm which have strongest PMA are patterned into islands using the self-assembling approach. As it is explained in section 3.4, our collaborators in Toshiba used diblock copolymer as the etch mask and patterned magnetic films with Ar milling at two angles of 0 and -80 degree to create patterns. Scanning electron

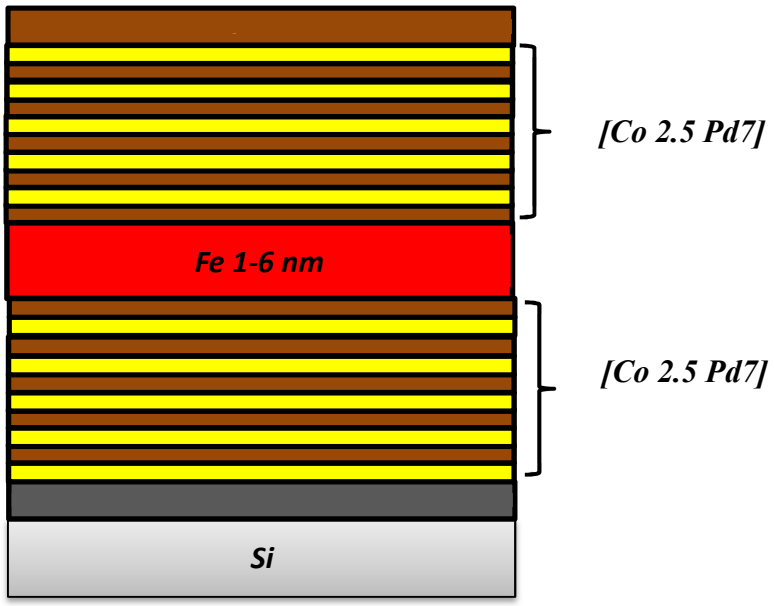

Figure 33: The schematic of the Film with Composite structure of SiOx/ Ta (2nm) / [Co(0.25 nm) / Pd (0.7 nm)]$_5$ / Fe (1-6 nm) / [Pd (0.7 nm) / Co (0.25 nm)]$_5$ / Pd (1 nm).

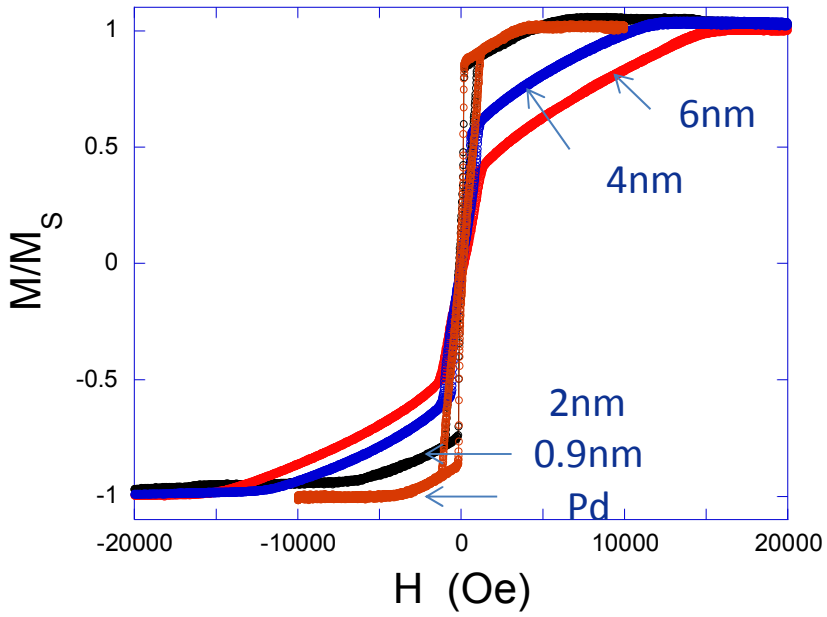

Figure 34: VSM measurement of out of plane magnetic hysteresis of magnetic films with structure of SiOx/ Ta (2nm) / [Co(0.25 nm) / Pd (0.7/0.9 nm)]$_5$ / Fe (2,4,6 nm) / [Pd (0.7/0.9 nm) / Co (0.25 nm)]$_5$ / Pd (1 nm).

microscopy (SEM) was used to image the patterns (Fig. 35). The average diameters of the dots are 25 nm with a 35nm pitch (center to center distance). This corresponds to the areal density of 0.5Tbit/ in^2. As it is shown in Fig. 35, the pattern lacks long range order; however, it shows short range order in a hexagonal lattice. The hysteresis loops of these samples for both in-plane and out-of-plane orientations are measured with VSM at room temperature and compared (Fig. 36 (a,b,c)). The comparison between the out-of-plane loop and the in-plane loops for each sample confirms that all three samples have a net perpendicular anisotropy. However, it is noticeable that as the Fe

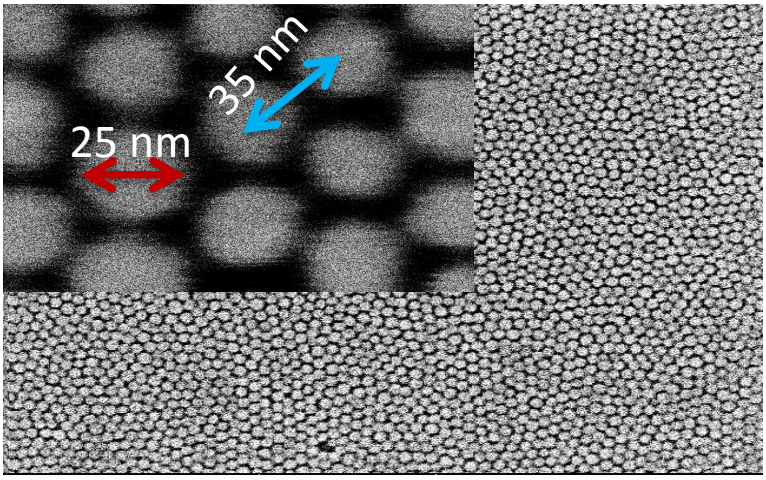

Figure 35: SEM image of the patterned sample using self-assembly method which shows the average island diameter of 25 nm and 35nm pitch.

thickness increases from 1 nm to 2 nm, the in-plane susceptibility is increasing within the Fe thickness. Figures 36 (d,e,f) are simplified sketches of sample's structures, and as it shown, as the Fe layers get thicker the shape anisotropy increases. As a result the magnetization of the Fe layer would prefer to lie more in the plane of the sample. Thus the effective anisotropy and the PMA of whole system decrease. The coercivity of the out-of-plane loops decreases as Fe thickness increases (Table. 2).

The previous loops are measured at room temperature; to study the temperature effects, the major loops at four different temperature of 390, 300 (room temperature), 180, and 60 K are measured for each samples and the resulted loops for 2-nm Fe is shown in Fig. 37. As temperature decreases, the coercivity increases and this is due to

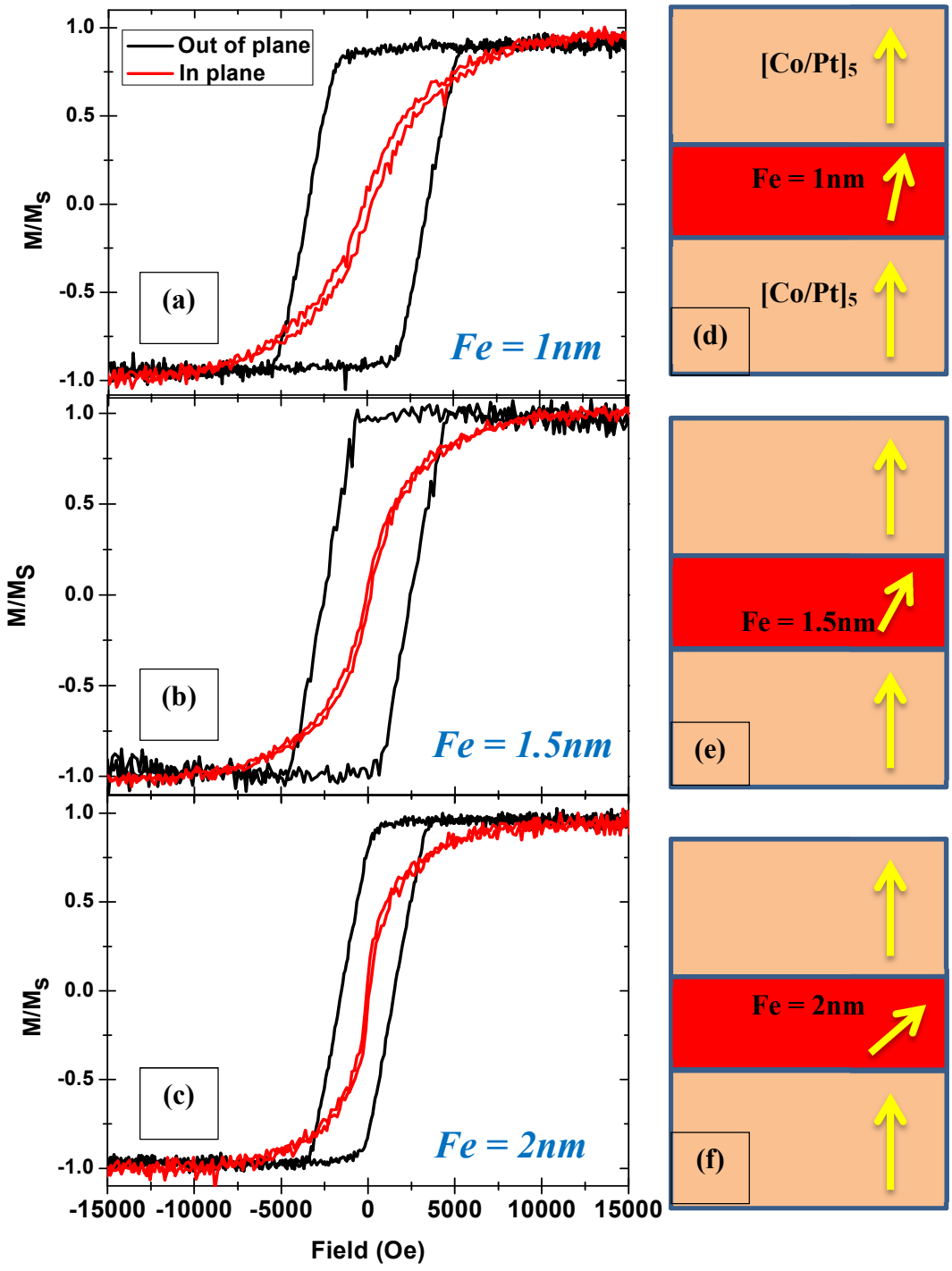

Figure 36: The in-plane and out of plane magnetic hysteresis loops for patternedsamples with structure of Ta (2nm) / [Co(0.25 nm) / Pd (0.7 nm)]5 / Fe(x) / [Pd (0.7 nm) / Co (0.25 nm)]5 / Pd (1 nm) where (a) x =1nm, (b) x= 1.5nm, and (c) x= 2nm and their corresponding magnetization behavior of Fe layer with respect to [Co/Pd] multilayer is shown (d,e,f).

reduction in the thermal fluctuations which assist the switching and an increase in the magnetic anisotropy with temperature. The value of coercivity at each temperature and the rate at which the coercivity changes with respect to temperature, $\frac{dH_c}{dT}$, are given for each sample in the Table.2.

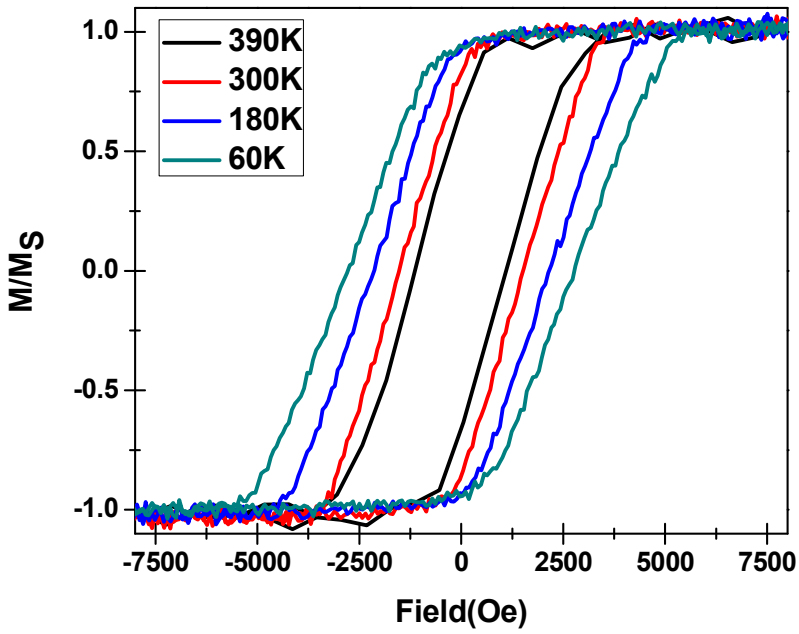

Figure 37: Out of plane hysteresis for patterned sample with structure of Ta (2nm) / [Co(0.25 nm) / Pd (0.7nm)]$_5$ / Fe(2 nm) / [Pd (0.7 nm) / Co (0.25 nm)]$_5$ / Pd (1 nm) at 4 different temperatures of 60,180,300, and 390 K

Table 2: The magnetic properties for patterned composite structure of Ta (2nm) / [Co(0.25 nm) / Pd (0.7nm)]$_5$ / Fe(x) / [Pd (0.7 nm) / Co (0.25 nm)]$_5$ / Pd (1 nm) where x= 1, 1.5, 2 nm.

Properties	Fe = 1nm	Fe = 1.5nm	Fe = 2nm
H_c (Oe)	3400	2400	1400
$\frac{dH_c}{dT}$ (Oe/K)	8.4	6.7	5.8

4.4. Switching-Field Distribution Using the ΔH(M,ΔM) Method

The switching-field distribution (SFD) is one of the most important parameters in designing magnetic recording media. The SFD is the distribution of the coercive field of individual grains in granular film and bits (islands) in BPM. One of the challenges in implementing BPM is ensuring a narrow SFD to secure the addressability of individual bits during gradient-field writing. The source of SFD is due to both intrinsic and extrinsic properties of the media. The intrinsic SFD, $\sigma_{intrinsic}$, originates from local variations of individual dot properties such as variations of the uniformity of the magnetic layer thicknesses, variations in the local magnetic anisotropy and lithographic irregularities like islands' shape, size and distance[56,57,58]. The extrinsic SFD, $\sigma_{extrinsic}$, is due to magnetic interactions such as dipolar interaction between an island and its neighbors. The dipolar interaction for perpendicular media tends to broaden the SFD [59] and also is expected to broaden the thermal stability parameters.[60] The areal density, material properties and the architecture of the media

are critical in determining the strength of interactions which affects the SFD, thermal stability and system performance.

As it mentioned in pervious section the Fe is placed in the center of the stack which decouples the reversal of the top and bottom multilayer structures. The Fe layer can also reduce the $\sigma_{intrinsic}$ although there are variations in size and shape of the islands (Fig.35). Since the samples have high density of islands, the dipolar interaction would affect the $\sigma_{extrinsic}$. The out-of-plane major loops have a broad transition during reversal (Fig.36) where a derivative of these loops gives the distribution for total SFD, σ_{total}, (Fig. 39 (c)). The total SFD width for all three samples is almost unaffected by the variation of the Fe thickness (Table. 3). The total SFD is the combination of intrinsic and extrinsic SFDs:

$$\sigma_{total} = \sigma_{intrinsic} + \sigma_{extrinsic} \quad (25)$$

To quantify the $\sigma_{intrinsic}$ for each sample, the $\Delta H(M, \Delta M)$ [59] method was used. This approach is an extension of the Tagawa and Nakamura approach [61] which has been shown to be well-suited for perpendicular recording media [59] as well as patterned media [62,63] as long as interactions can be treated within the mean field approximation. This method is based on the comparison of the minor and major loops at different magnetization points. In Fig. 38 a major and a minor loop for a typical recording media is shown, and at different points of these loops the distribution of

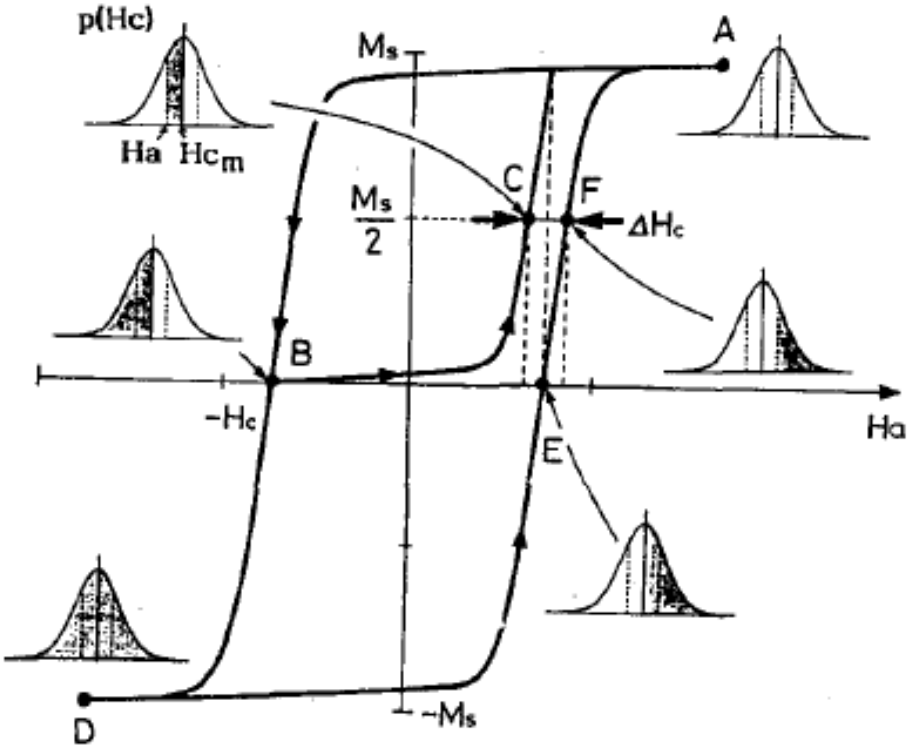

Figure 38: A magnetic hysteresis loop and a minor loop is shown. At different points of the majorand minor loop, the distribution of magnetic moments with either up,1,or down, 0(hatched area), are shown[61].

particles at different magnetization state, hatched for down magnetization and clear for the up magnetization, is shown. Point A and D are the saturation points where all the particle magnetization is either up, A, or down, D. Points B and E are the coercivity points where the particles with coercive field less than the average coercivity, H_c are switched. The minor loop starts at point B where the particles with switching field of less than H_c are switched and pointing down. These are half of the total particles. By increasing the field toward positive saturation, the same particles start again switching back to up position. At point C, half of these particles that have switching field less

than H_a are switched. Point C is the coercivity of the minor loop and it is where magnetization is half of the saturation magnetization and 1/4th of particles have negative saturation while 3/4th have positive magnetization. At point F, the magnetization is also at half of the M_S, and the same number of particles with up and down magnetization, but different population of the particles. The fields at the point C and F can be defined as[61] :

$$H(C) = H_C - 0.675\ \sigma_{hc} \quad (26)$$

$$H(F) = H_C + 0.675\ \sigma_{hc} \quad (27)$$

$$\sigma_{hc} = \frac{\Delta H_C}{1.35} \quad (28)$$

where σ_{hc} is the intrinsic distribution. The effects of dipolar interaction between the islands is eliminated with this method, since ΔH is being calculated at the point with the same value of the average magnetization. Therefore within a mean field model the average interactions will be the same. Based on the Tagawa and Nakamura method [61], the intrinsic distribution can be extracted only relying on one data point. However there is no restriction within the method that it can't and shouldn't be expanded. Instead of one minor loop, many minor loops can be measured at different points within the major loop and ΔH can be calculated at any point of the minor loop not only at its coercive point. With this method, ΔH data points can be defined as a function of magnetization, M and return point with respect to the saturation magnetization, $\Delta M = M_S - M_{rev}$, which gives data sets of ΔH(M, ΔM) [55]. To relate the intrinsic distribution, $D_i(H_s)$ to ΔH values, the branch of major loop with decreasing field can be formulated as[55] :

$$M = 1 - 2\int_{-\infty}^{-(H_M + H_i(M))} D(H_S)\, dH_S \tag{29}$$

where H_M is the external field at which the magnetization value of M is reached, $H_i(M)$ is the average interaction fields, and $D_i(H_S)$ is the normalized SFD which is centered at the positive H_c. A distribution integral can be defined as:

$$I(-(H_M + H_i(M)) = \int_{-\infty}^{-(H_M + H_i(M))} D(H_S)\, dH_S \tag{30}$$

The magnetic field at magnetization M can be defined:

$$H_M(M) = -I^{-1}\left(\frac{1-M}{2}\right) - H_i(M) \tag{31}$$

From this, the magnetic field for a minor loop can be defined as magnetization starts from Mrev = 1- ΔM as:

$$H_m(M) = -I^{-1}\left(\frac{1-(M+\Delta M)}{2}\right) - H_i(M) \tag{32}$$

Based on the mean field approximation, $H_i(M)$ is only depended on M and as a result its' value is same in both Eqs. 31 and 32. Thus, in calculating $\Delta H = H_M(M) - H_m(M)$, the interactions are removed from ΔH data sets. :

$$\Delta H(M, \Delta M) = I^{-1}\left(\frac{1-M}{2}\right) - I^{-1}\left(\frac{1-(M+\Delta M)}{2}\right) \tag{33}$$

To achieve the final distribution, a certain parameterized distribution can be considered such as Lorenzian, Gaussian, or a combination of them:

Lorenzian:

$$D(H_S) = \frac{2W}{\pi}\frac{1}{W^2 + 4(H_S - H_C)^2} \rightarrow$$

$$\Delta H(M, \Delta M) = \frac{W}{2}\left(\tan\left(\frac{\pi}{2}(M + \Delta M) - \tan\left(\frac{\pi}{2}M\right)\right)\right) \tag{34}$$

Gaussian:

$$D(H_S) = \frac{1}{\sqrt{2\pi}.\sigma} . \exp\left[-2\left(\frac{H_S - H_C}{2\sigma}\right)^2\right] \rightarrow$$

$$\Delta H(M, \Delta M) = \sqrt{2}.\sigma(\mathrm{erf}^{-1}(M + \Delta M) - \mathrm{erf}^{-1}(M)) \quad (35)$$

For the three patterned samples with structure of Ta (2_{nm}) / [Co(0.25 $_{nm}$) / Pd (0.7_{nm})]$_5$ / Fe(x) / [Pd (0.7 $_{nm}$) / Co (0.25 $_{nm}$)]$_5$ / Pd (1 $_{nm}$), where x = 1, 1.5, and 2 nm, the intrinsic distribution was calculated using this method (Table.3) [(64)] to analyze minor loop data. VSM measurements was used to determine three minor loops in addition to the major loop, and combination of two Gaussians was considered as a parameterized distribution:

$$D(H_S) = \sqrt{2}\sigma_1 \frac{\mathrm{erf}^{-1}(M)}{(1+\alpha M)} + \sqrt{2}\sigma_2 \frac{\mathrm{erf}^{-1}(M)}{(1+\beta M)} \quad (36)$$

where α and β are parameters that account for potential asymmetric shapes of the curves [(62)]. The calculated ΔH(M, ΔM) data sets for the patterned samples was fitted to Eq. 36 (Fig. 39(b)) and the extracted parameters was used to the corresponding intrinsic distribution and compares it to its' total SFD (Fig. 39(c)). The intrinsic distribution is quite narrow compare to total SFD, which indicates that the primary contribution to the SFD in the sample is through the dipolar interactions of the closely packed islands.[(64)] Base on the $D(H_S)$, the hysteresis loop of the islands in the absence of dipolar interactions can be calculated (Fig. 39(a)). The average dipolar interaction also can be calculated by subtracting the calculated intrinsic loop from the major loop.

Table 3: Calculated SFD for patterned sample with structure of [Co/Pd]5/Fe(x)/[Pd/Co] for different Fe thicknesses using ΔH(M,ΔM) method.

Properties	Fe = 1nm	Fe = 1.5nm	Fe = 2nm
σ_{Total} (Oe)	1300	1330	1250
$\sigma_{Intrinsic}$ (Oe)	365	265	205
$\sigma_{Intrinsic}$ (Oe)/H_c	10%	11%	14%

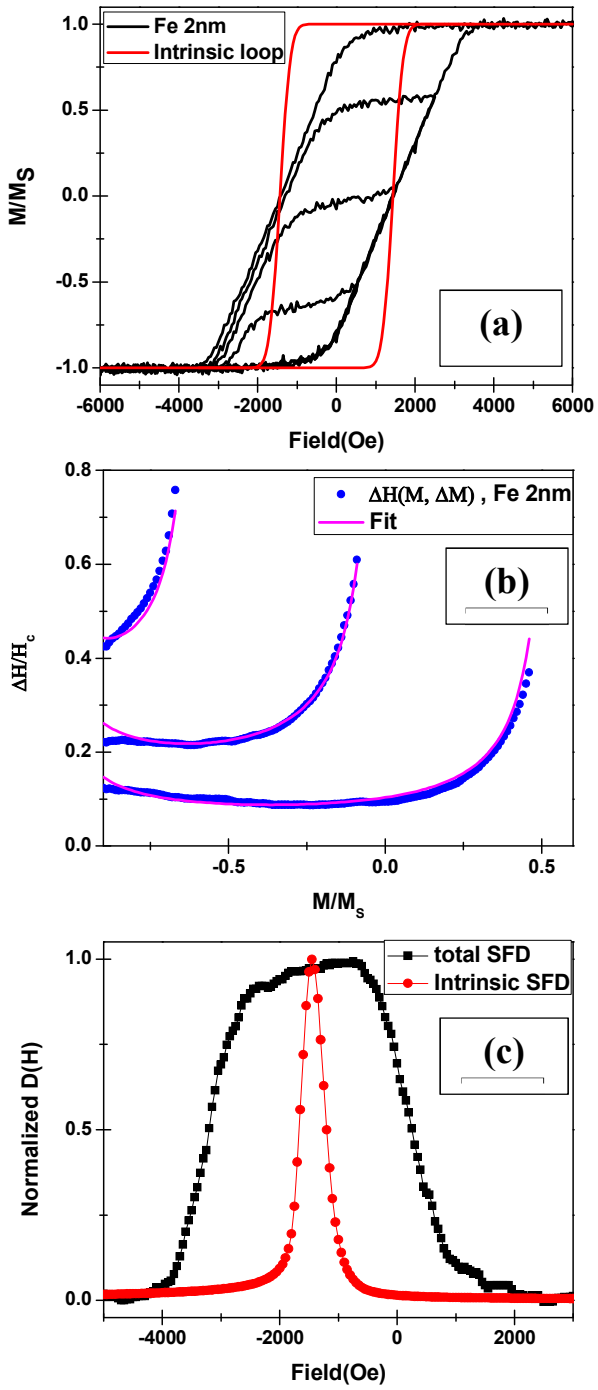

Figure 39: (a) The measured major loop and minor loops for a sample with structure of Ta (2nm) / [Co(0.25 nm) / Pd (0.7nm)]5 / Fe(2 nm) / [Pd (0.7 nm) / Co (0.25 nm)]5 / Pd (1 nm) is measured by VSM to extract the intrinsic distribution from which the intrinsic loop (the red loop) is calculated. (b) the ΔH(M, ΔM) data is fitted to a asymmetric Gaussian distribution.(c) The intrinsic distribution (red dots) and the total distribution (black squares) are compared. 4.5. Thermal stability

4.5. Thermal Stability

In a uniaxial magnetic materials, the energy profile has two stable minima which refer to either magnetic direction down, 0, or up 1, and these two minima are separated by energy barrier (Fig. 40). The value of the energy barrier, E_B, depends on the magnetic particle's volume and its' anisotropy constant in zero external magnetic field:

$$E_B = K.V \tag{37}$$

where, K is the anisotropy constant, and V is the volume of the particle. This assumes that the particle volume V is sufficiently small that it can be treated as a single-domain particle. This energy should be compared to the thermal energy is defined as:

$$E_T = k_B.T \tag{38}$$

where, k_B is the Boltzmann constant, and T is the temperature in Kelvin. In particular cases such as superparamagnetism, where the volume of a particle is very small, thermal fluctuations would overcome the energy barrier, and the magnetization of the particle becomes unstable. To ensure the magnetic thermal stability, the ratio of E_B to E_T , $\frac{KV}{k_BT}$ is an important parameter in industry and it is set that it should have the minimum value of :

$$\frac{K.V}{K_BT} > 60$$

to ensure the stability for archival storage.

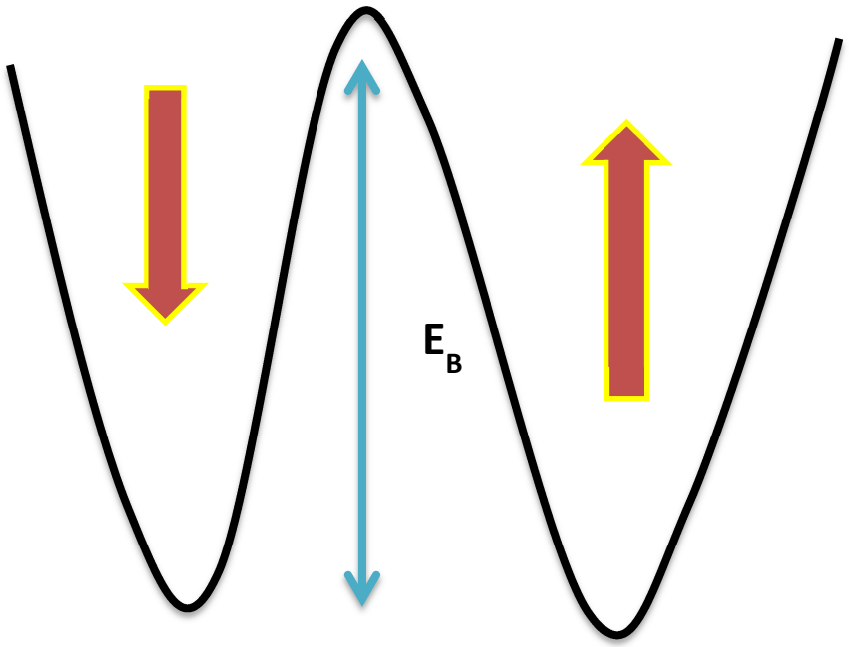

Figure 40: A simple energy profile for a magnetic material. The two minimums, the up and down magnetization is separated by an energy barrier.

Due to existence of the thermal energy a magnetic sample's moment is time dependent. A magnetic sample with initial magnetic moment of M_0 is considered. The rate at which the magnetic moment decreases by time is:

$$\frac{dM}{dt} = -f_0 \, M \, e^{\frac{-KV}{K_B T}} \tag{39}$$

where , f_0 is frequency factor with a value of 10^{10} sec^{-1}, M is the magnetization of the sample at time t, and the $e^{\frac{-KV}{K_B T}}$ states the probability of particle switching by thermal energy. This assumes that there is no external magnetic field applied to the sample. As a result we can define the time-dependent magnetization as:

$$M(t) = M_0[2e^{-rt} - 1] \tag{40}$$

$$r = f_0 e^{-\frac{KV}{K_B T}} \tag{41}$$

The total energy of a magnetic sample in an external magnetic field H_{ex} with uniaxial anisotropy and the field applied parallel to the anisotropy axis can be expressed as:

$$E = H_{ex} M_S \cos(\theta) + K \sin(\theta)^2 \tag{42}$$

where θ is the angle between magnetization the applied field and anisotropy axis.

For any applied field the energy barrier of the sample can be calculated as:

$$E_B = E_{max} - E_{min} \tag{43}$$

$$E_B = KV\left(1 - \frac{H_{ex} M_S}{2K}\right)^2 \tag{44}$$

E_B decreases as external field increases, and $E_B = 0$ when $H_{ex} = H_0 = \frac{2K}{M_S}$. H_0 is the coercivity in the absence of thermal energy. However, when thermal energies are considered the coercive field is time dependent, and its value decreases as the external field sweep rate, $\frac{\Delta H}{\Delta t}$ decreases. That is, the slower the field is swept the more likely thermal energy can switch the particle. Based on the Stoner-Wolfrath model [65], Sharrock formulated the time dependence of the coercive field as [66]:

$$H_C(t) = H_0\left\{1 - \left[\left(\frac{K_B T}{KV}\right)\ln(f_0 t)\right]^n\right\} \tag{45}$$

Where t is the time a field pulse is applied the sample and n =2 for the simple case for the field applied parallel to the anisotropy axis. More generally n can take on a range of values $1 \leq n \leq 2$.

Later, Chantrell et al. rewrote this formula to show the dependence of the coercive field on field sweep rate explicitly [67]:

$$H_c(R) = H_0\left[1 - \left(\frac{1}{a}\ln\left(\frac{f_0 H_0}{2a}\frac{1}{R}\right)\right)^{\frac{1}{n}}\right] \quad (46)$$

where f_0 is the attempt frequency of about 10^{10} Hz, the exponent n = 3/2 is used to account for possible incoherent reversal processes that arise from the Fe layers [appendix] [68], R = dHex/dt is the magnetic field sweep rate, H_c and H_0 are the coercive field and the short time switching field respectively, and $a = \frac{E_B}{k_B T}$ is the ratio of energy barrier to thermal energy.

Thermal stability is an important topic in bit patterned media since the bit size has decreased and strong interactions exist between bits that can alter the local stability. To quantify this we use the dependence of the coercive field to the applied field sweep rate to determine the thermal stability in our samples. Polar magnetic optical Kerr effect (MOKE) was used to measure hysteresis loops for all three samples with structure of Ta (2_{nm}) / [Co(0.25_{nm}) / Pd (0.7_{nm})]$_5$ / Fe (x) / [Pd (0.7_{nm}) / Co (0.25_{nm})]$_5$ / Pd (1_{nm}) where x= 1, 1.5, and 2nm, at four different magnetic field sweep rates, R, ranging from 4 to 4000 Oe/sec (Fig. 42). There is a distribution in physical properties of islands and magnetic interaction between islands which as it shown in the previous section result in distribution in SFD. These distributions also is expected to affect thermal stability. For the purpose of extracting the energy barrier, Eq. 46 can be modified and be rewritten for each $\frac{M}{M_S}$:

$$H_c\left(\frac{M}{M_S}\right) = H_0\left(\frac{M}{M_S}\right)\left[1 - \left(\frac{1}{a}\ln\left(\frac{f_0 H_0\left(\frac{M}{M_S}\right)}{2a}\frac{1}{R}\right)\right)^{\frac{1}{n}}\right] \quad (47)$$

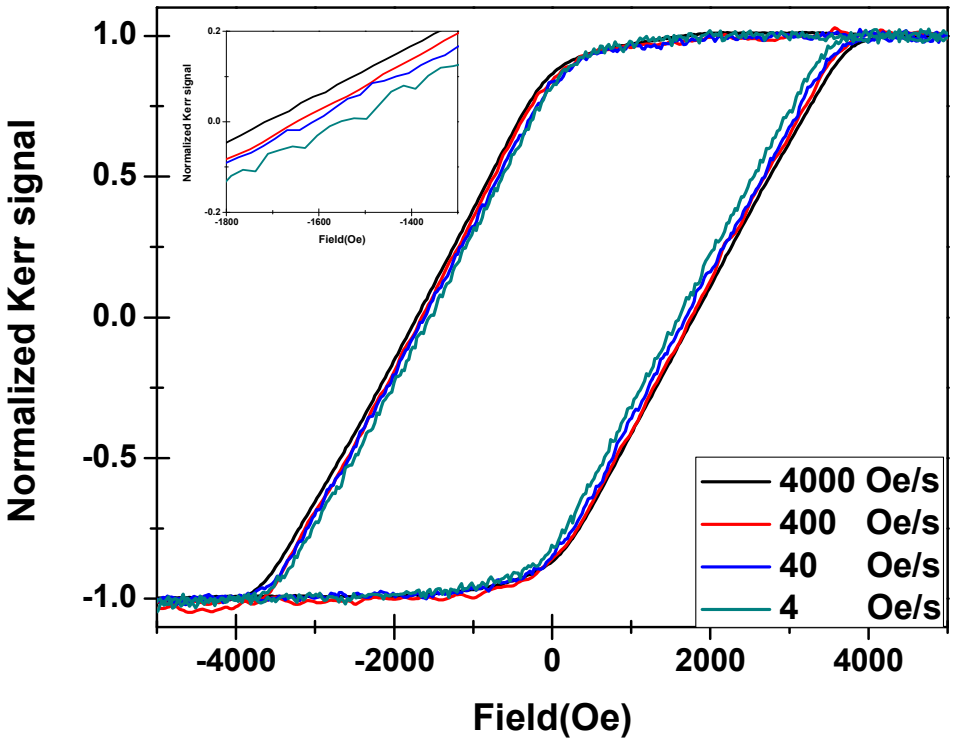

Figure 41: The measured major loops for Fe=2nm at various sweep rates by MOKE. The insetshows the time dependence near the coercive field.

The measured field sweep rate dependence of switching field was fitted to the Eq. 47 and thermal stability parameters can be extracted for different $\frac{M}{M_S}$ values. The extracted H_0 values at $\frac{M}{M_S}$ values are plotted along with the hysteresis loop for Fe = 2nm (Fig. 42). As $\frac{M}{M_S}$ decreases from 0.9 to -0.9 you see the switching fields increase

and represent the expected loop shape for fast times switching in the absence of thermal excitations. The values of H_{c0} that are extracted from fitting the coercive fields for all three samples are shown in Table. 4, and they behave like H_c and decreases as Fe thickness increases which is caused by reduction in effective anisotropy of the system. In Table 4 also is shown that $\frac{\sigma_{intrinsic}}{H_{co}}$ is relatively constant as also shown for [Co/Pd] –[Co-Ni]-based composite structure BPM [69]. In Fig. 43, the time dependence of field at selected $\frac{M}{M_S}$ values is plotted for the sample with Fe thickness of 2-nm and the values of energy barrier for island reversing at a given

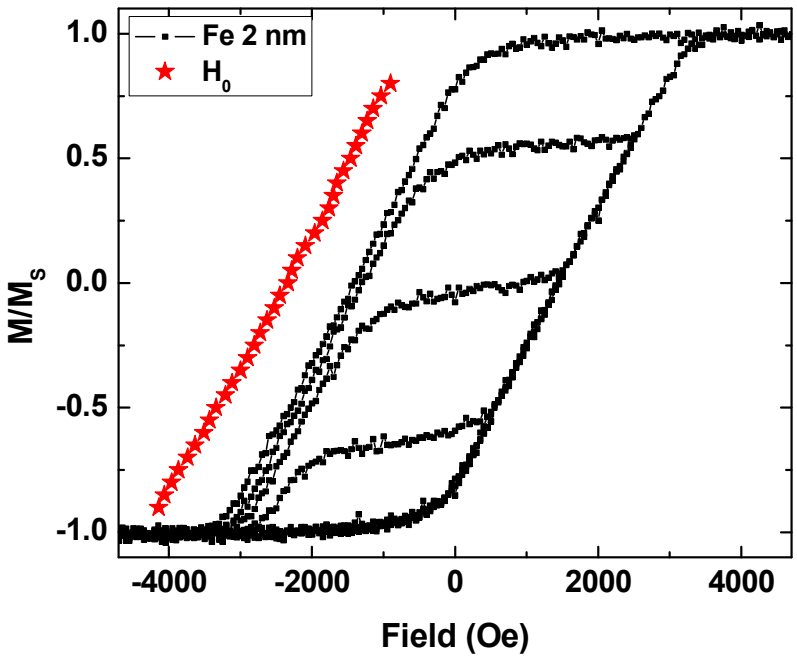

Figure 42: The hysteresis loop for the sample with structure of Co(0.25 nm) / Pd (0.7 nm)]$_5$ / Fe (2 nm) / [Pd (0.7 nm) / Co (0.25 nm)]$_5$ along with extracted H_0 values using equation 47

$\frac{M}{M_S}$ are extracted from Eq. 47 and shown. As $\frac{M}{M_S}$decreases the energy barrier increases meaning the first islands to reverse (near $\frac{M}{M_S}$=1) have a much lower effective E_B compared to the last islands to reverse. This behavior can be explained based on intrinsic properties but, as we will see, is primarily arising from dipolar interactions. The intrinsic properties depend on physical properties, so the islands with the lowest anisotropy and/or volume have the lowest E_B, hence would be expected to switch first. The dipolar interaction affects the effective field on each island in a way that for positive$\frac{M}{M_S}$, the dipolar fields is in favor of reversal and therefore lowers the effective

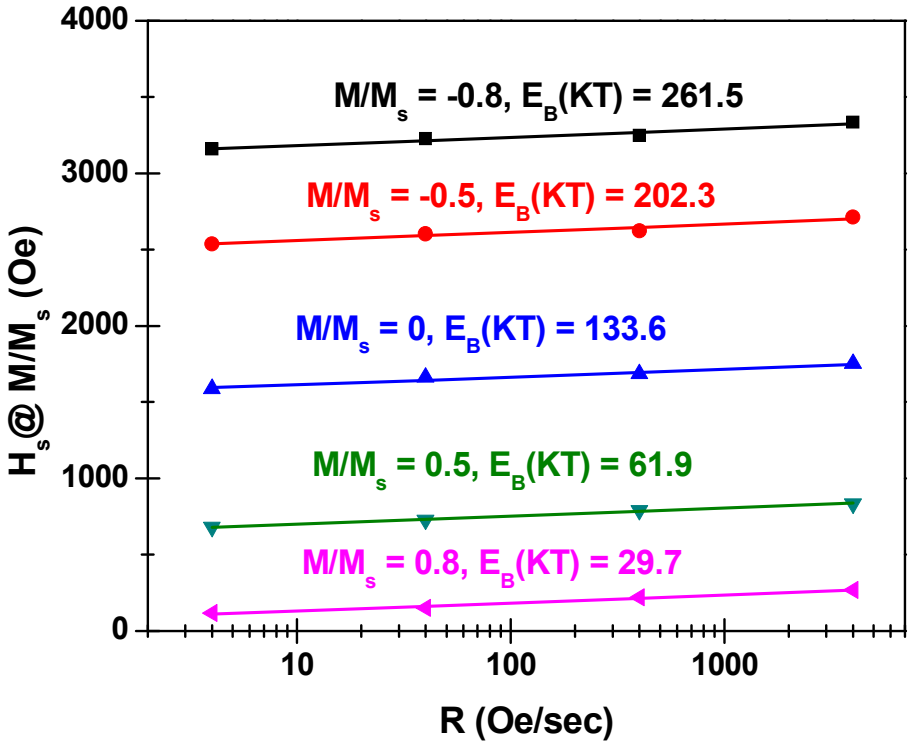

Figure 43: The time dependent switching field for a Fe=2nm sample. at selected M/M_S valuesThe solid lines are fit to Eq. 47. The values of energy barrier and short time switching field are extracted.

E_B. However, for negative $\frac{M}{M_S}$ the dipolar interactions oppose reversal and increase the E_B. It should be noted that the energy barrier at $\frac{M}{M_S} = 0$ which is extracted by fitting the coercive field, represents the average island stability, and it is shown in Table 4 for all three samples. The average E_B values confirm that the islands are thermally stable for all three samples although the E_B decreases as Fe thickness increases, as expected. However, considering the different regions of dots, there is a distribution of E_B for the three samples as a function of $\frac{M}{M_S}$ which is extracted using the time dependent loops and Eq. 47 and it is shown in Fig. 44. There is a broad range of E_B for all three samples, but the range increases as Fe layer become thicker. For the 1-nm Fe layer sample the E_B ranges from 150 to 250 k_BT while for the 2-nm Fe sample this range increases to 20 to 300 k_BT more than an order of magnitude distribution in values of E_B for the range of $\frac{M}{M_S}$ values. In the previous section, it was confirmed that the dipolar interaction is the primary source for SFD. As a result, it can be assumed that the dipolar interaction is also responsible for the energy barrier distribution. The average dipolar field at each $\frac{M}{M_S}$ value, $H_d(\frac{M}{M_S})$, can be extracted from the field difference of the intrinsic loop and the measured hysteresis loops at each $\frac{M}{M_S}$. Based on the mean field interaction the dipolar field is roughly linear with $\frac{M}{M_S}$. In Table 4 the ratio of $H_d(\frac{M}{M_S})$ is given which increases with increasing Fe thickness. Using the Stoner-Wohlfarth model for a single domain particle, the E_B values for all $\frac{M}{M_S}$ relative to mean value of $E_B(0)$ which are given in table 4 and can be calculated using the :

$$E_B\left(\frac{M}{M_S}\right) = E_B(0)\left[1 - \left(\frac{H_d\left(\frac{M}{M_S}\right)}{H_{CO}}\right)\right]^n \quad (48)$$

where we use the exponent n = 3/2 in correlation with Eq. 47. The expected E_B distributions calculated using Eq. (48) and shown in Fig. 44 assuming no intrinsic E_B distributions. The calculated values agree with the measured ones quantitatively and it confirms that dipolar interactions are the primary origin of the distribution in energy barrier in this case of dense BPM. It can be concluded that the intrinsic distribution in E_B is small compared to the distributions arising from the dipolar interactions and can be ignored. It is worth mentioning that the result is independent of the chosen value of the exponent n in Eqs. 47 and 48, as long as the same n value is used in both equations so that the calculated and measured energy barrier distributions are self-consistent (see the appendix for a detailed description of this).

The broad distribution in E_B is based on the dipolar interaction (Fig.44), and it can have a dramatic impact on the thermal stability of patterned media particularly for high density patterns. To avoid the coercive field limitation, the material design should consider limiting the dipolar interactions. Some examples of such structures are antiferromagnetically-coupled BPM [70] and capped bit patterned media. In capped BPM, a continuous capping layer is coupled to the islands [60,67]. Micromagnetic models have shown that the exchange interactions introduced through coupling with a continuous capping layer can effectively offset the energy barrier distribution arising from dipolar interactions.

Table 4: Magnetic properties and thermal stability for sample with ECC structure of [Co/Pd]5/Fe(x)/[Pd/Co] for different Fe thicknesses.

Properties	Fe = 1nm	Fe = 1.5nm	Fe = 2nm
H_{c0} (Oe)	4650	3450	2330
$\frac{\partial_{\text{Intrinsic}}}{H_{Co}}$	7.8%	7.7%	8.8%
E_B @ H_c (K_BT)	190	160	135
Hd / $(\frac{M}{M_S})$ (Oe)	1235	1470	1495
ξ	2.2	1.9	2.9

In Table 4, the figure of merit is calculated using Eq. 23 (Section 4.2.) for all three samples. Each bit, cylindrical pattern, can be assumed as one grain, and for each sample the average energy barrier is used to calculate the figure of merit, ζ. The values are in agreement with prediction for composite structures.

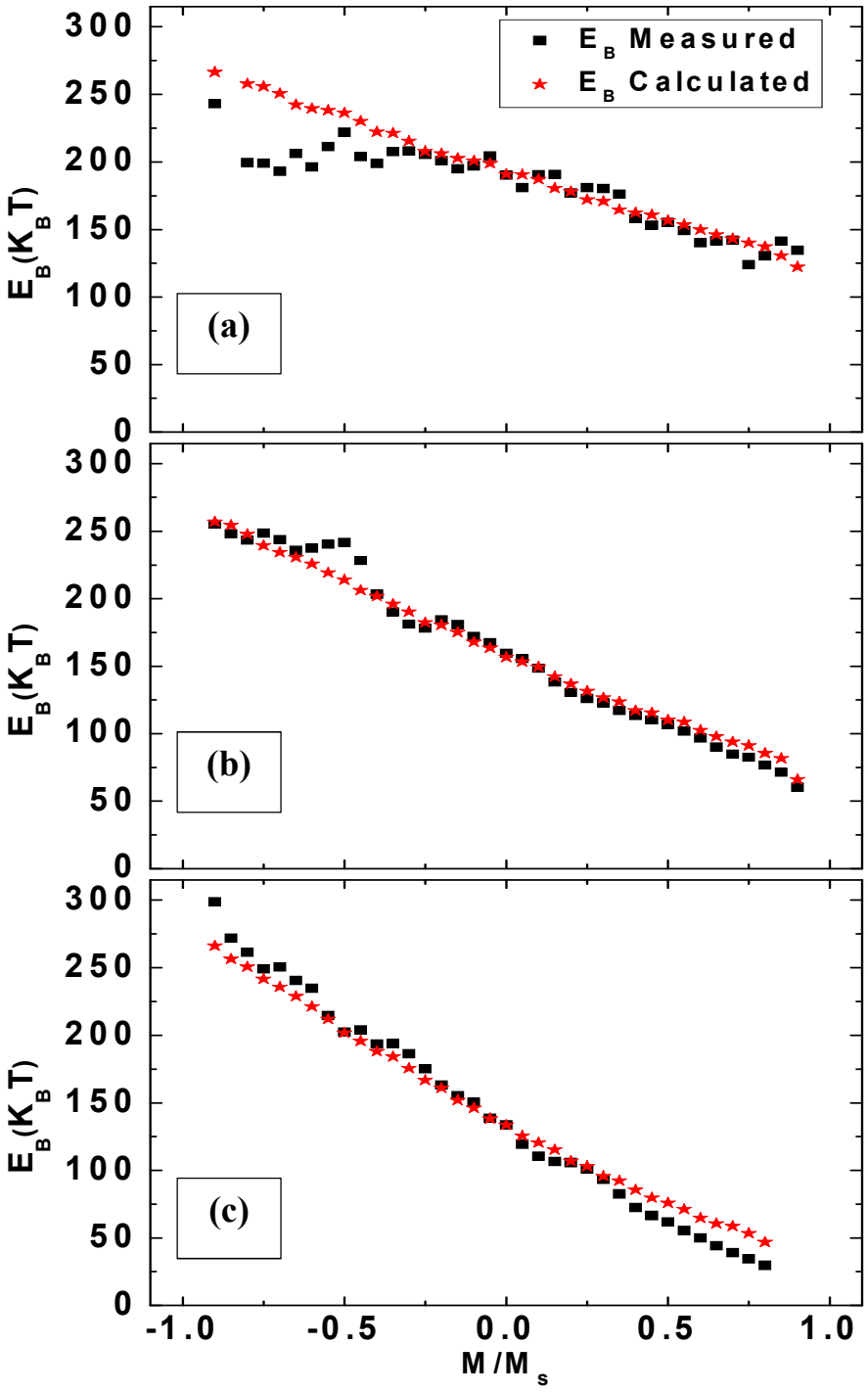

Figure 44: The distribution of energy barriers for $[Co/Pd]_5/Fe(x)/[Pd/Cp]_5$ BPM samples: (a) x=1nm,(b) x=1.5nm, and (c) x=2nm. The squares show the measured values of energy barrier for each M/M_S . The stars are the calculated values using eq. 44, the contribution from dipolar interaction. 4.6. Temperature Dependent SFD

4.6. Temperature Dependence of Switching Field Distribution

The SFD of the sample at room temperature was studied thoroughly in section 4.4 and in the previous section 4.5 the thermal stability of the samples were studied. Due to importance of the effect of temperature, this section analyzes the temperature dependence of total and intrinsic switching field distribution.

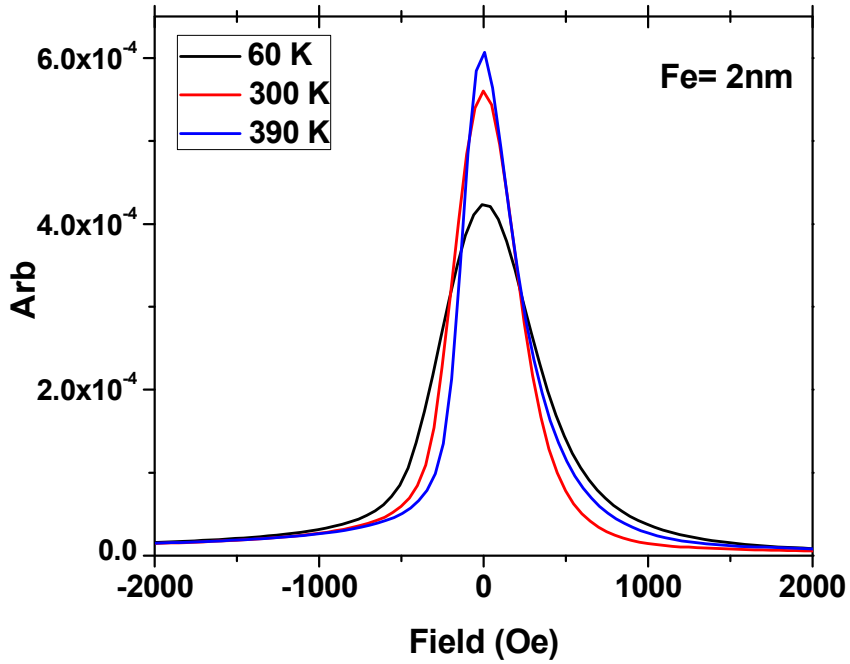

Figure 45: Intrinsic SFD for sample with Fe=2nm at 3 different temperatures are compared. As temperature increases the distribution decreases.

Table 5: Calculated SFD at 3 different temperatures for patterned samples with structure of [Co/Pd]5/Fe(x)/[Pd/Co] with different Fe thicknesses using ΔH(M,ΔM) method is compared.

Sample	Fe = 1nm			Fe =1.5 nm		Fe = 2 nm		
Temperature(K)	60	300	390	60	300	60	300	390
H_c (Oe)	5500	3400	1800	4200	2400	2640	1400	960
σ_{total} (Oe)	1660	1300	1115	1720	1330	1670	1250	1190
$\sigma_{intrinsic}$ (Oe)	545	365	200	370	265	305	205	195
σ_{total} / H_{c0}	0.36	0.38	0.48	0.37	0.39	0.36	0.36	0.51
$\sigma_{intrinsic}$ /H_{c0}	0.12	0.11	0.09	0.08	0.08	0.07	0.06	0.08

The method of ΔH (M, ΔM) [55] that is explained in detail in section 4.4 is used to calculate the total and intrinsic SFDs. The major loop along with minor loops at two temperatures of 60 K and 390 K was measured and compared to the room temperature measurement. The total SFD, σ_{total}, is extracted by calculating the derivative of the major loop, and this corresponds to the broadening of the loop. The intrinsic SFD, $\sigma_{intrinsic}$, is calculated by fitting the ΔH (M, ΔM) data to the combination of two Gaussians (same as section 4.4.) and extract the distribution parameters. Figure 45 shows the $\sigma_{intrinsic}$ for the sample with 2 nm of Fe at three different temperatures of 60, 300, and 390 K. The switching field distribution values for all three samples are shown and compared in Table 5. As the temperature increases, the intrinsic and total SFD decreases for each sample. However, at each temperature the value of total SFD

stays constant for three samples, but the $\sigma_{intrinsic}$ decreases as Fe thickness increases. Figure 46 compares the intrinsic distribution of three samples at each temperature. Although the distribution decreases as temperature increases the ratio of SFD/H_{c0} stays constant (Table 5) which strongly suggests that the thermal fluctuations doesn't have overall effect on broadening the switching fields in this patterned composite structure samples.

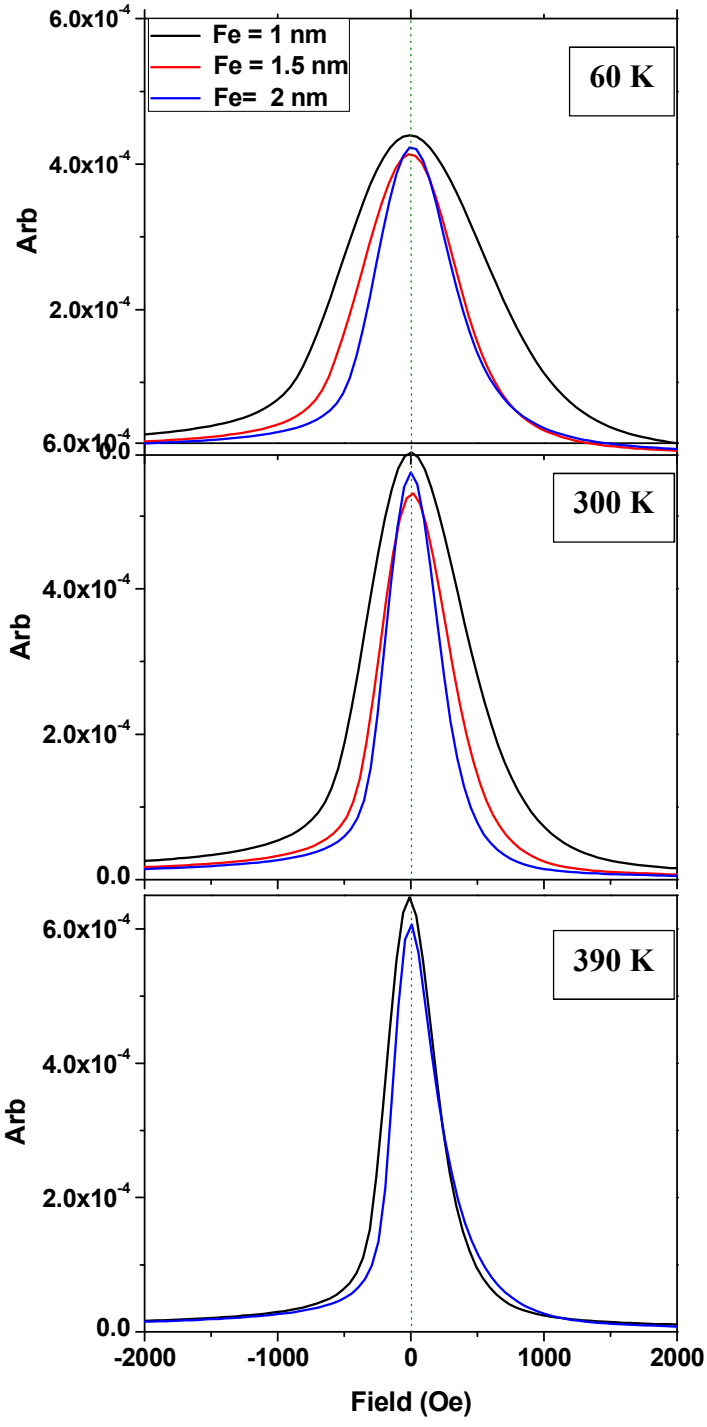

Figure 46: Intrinsic switching field distribution of patterned samples with structure of [Co/Pd]5/Fe(x)/[Pd/Co] where x= 1, 1.5, and 2 nm at three different temperatures of 60,300, and 390 K are compared

Chapter 4, in part, is published: N.Eibagi, J.J. Kan, F.E. Spada, and E.E. Fullerton, “Role of dipolar interaction on the thermal stability of high density bit-patterned media”, IEEE Magnetic Letters (2012). I also would like to thank Fred Spada for giving me access to the polar MOKE for data that is represented in chapter 4.

.

Chapter 5: Depth Dependent Magnetization Study of Bit-Patterned Media with Composite Structure

5.1. Polarized Neutron Reflectometry

Polarized neutron reflectometry (PNR) is often used to study magnetic thin films and interfacial coupling in multilayers [72, 73]. Neutrons are particles that weakly interact with matter, therefore they are not destructive and have high penetration, so they are used to determine the depth nanostructure of materials. Neutrons scatter at the vicinity of the nucleus and their scattering parameters depend on the particular isotope, through which neutrons can probe the composition of structures. Neutrons are Fermions and have half integer spin, ±½, and through their spins, they also interact with materials' unpaired electrons and thus probe local magnetization.

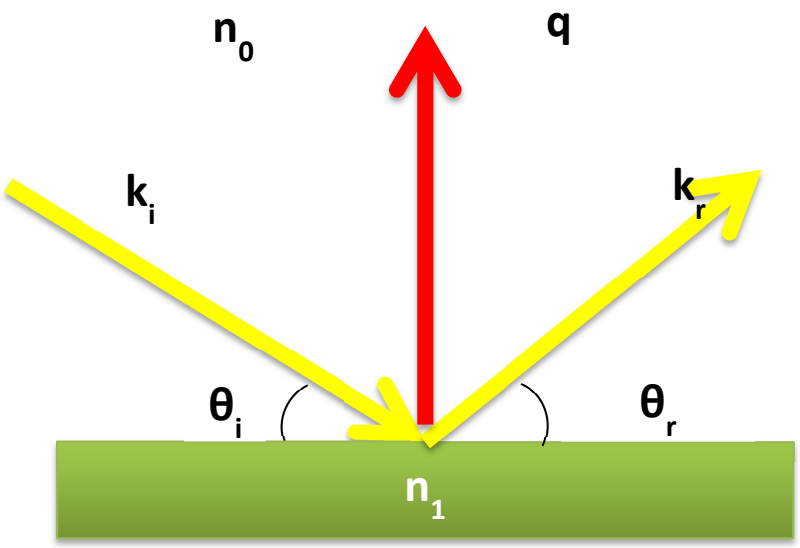

Figure 47: Specular reflection off of sample's surface.

Specular reflection (Fig.47) is coherent scattering with conservation of momentum. Neutron specular reflection can be treated similarly to optical reflection where Snell's law is applied:

$$n = \frac{n_i}{n_r} = \frac{\cos\theta_i}{\cos\theta_r} \tag{49}$$

$$n = \frac{k_r}{k_i} \tag{50}$$

where n is the index of refraction, θ is the angle of beam with respect to the normal of the surface, k is the wave vector, and the indices of i and r refer to the incident and reflected beam respectively. For specular reflection, $\theta_i = \theta_f = \theta$, and the scattering vector is defined as:

$$q = k_f - k_i = \frac{4\pi}{\lambda}\sin(\theta_i) \tag{51}$$

where λ is the wavelength of the neutrons. The q can be varied through the incident angle and the wavelength of the neutrons. Reflectivity is defined as the ratio of the reflected and incident intensities, I:

$$R = \frac{I_r}{I_i} \tag{52}$$

As mentioned neutrons interact with nucleus and their interaction can be defined by the nuclear potential [74]:

$$V_n(r) = \frac{2\pi\hbar^2}{m} b\, N \tag{53}$$

where N is the number of atoms per volume, b is scattering length, and m is the mass of the neutrons. Scattering length density (SLD) is defined for multicomponent materials as:

$$\rho = \sum_{j=1}^{M} N_j b_j \quad (54)$$

where j refers to each type of isotopes, and M is the total number of distinct isotopes. The nuclear SLD, ρ, is a unique value for each nuclei and its value is experimentally determined. Neutrons also interact with magnetization and the magnetic interaction can be defined as:

$$V = -\mu . B(z) \quad (55)$$

where μ is the magnetic moment of the neutrons and B is magnetic induction at a distance z from the surface. Thus, the magnetic SLD is [74]:

$$\rho_{\pm M} = \mp \frac{m}{2\pi\hbar^2} \mu B \quad (56)$$

the + and – signs refer to the spin up and spin down of the neutrons, respectively (their polarization status). As a beam of neutrons illuminates a magnetic sample, the beam interacts with a potential that is the sum of the nuclear and magnetic potential.

PNR proves the depth profile of the absolute value of the magnetization vector distribution in contrast to conventional magnetometer which determines the total magnetic moment averaged over the entire volume. For reflectivity measurements the reflected intensity is measured as a function of the scattering vector, q. To vary q, either the incident angle, θ, is changed at a fixed wavelength λ or a broad wavelength band is used through a time-of-flight at a fixed incidence angle. The current neutron experiments were performed using the time-of-flight technique. To define the time of flight, the de Broglie equation needs to be considered:

$$\lambda = \frac{h}{mv} \quad (57)$$

where λ is the wavelength, m is the mass of neutron, ν is the velocity, and h is Planck's constant, $h=6.626\times10^{-34}$ Js. The velocity can be measured by measuring the time, t, during which a neutron travels a path with a length of L:

$$v = \frac{L}{t} \tag{58}$$

The time of flight is t, considering the known and fixed length of the neutrons' path between the neutron source and the detector. In spallation neutron source, pulsed neutron beams are generated as a result of strike of accelerated pulsed protons to a heavy metal target. The moderated neutrons from produced pulse have range of energy that can be resolved with the time of flight. The wavelength of neutrons is calibrated and can be measured by knowing the time-of-flight and using Eqs. 57 and 58. Thus, in time of flight technique, the incident angle is kept fixed while the wavelength is varied base on the neutrons' energy determined from the arrival time to the detector. In PNR, there are four different reflectivity configurations, two non-spin-flip and two spin-flip, which are based on the incident and reflect neutron's polarization [75]. The two non-spin-flip configurations are R^{++} and R^{--}, where the first superscript refers to the polarization state of the incident neutron, and the second one refers to the polarization of the reflected neutrons. The + and – signs refer to the direction of neutron spin parallel and antiparallel to the direction of the external magnetic field. The two spin-flip configurations are R^{+-} and R^{-+}, that again the superscripts like the non-spin-flip configurations refer to the polarization of the incident (first) and reflected (second) neutrons. The spin-flip configurations are generated by the component of magnetic

moment (or flux) within sample that is perpendicular to the polarization axis of neutrons and which are significant in chiral magnetic structures.

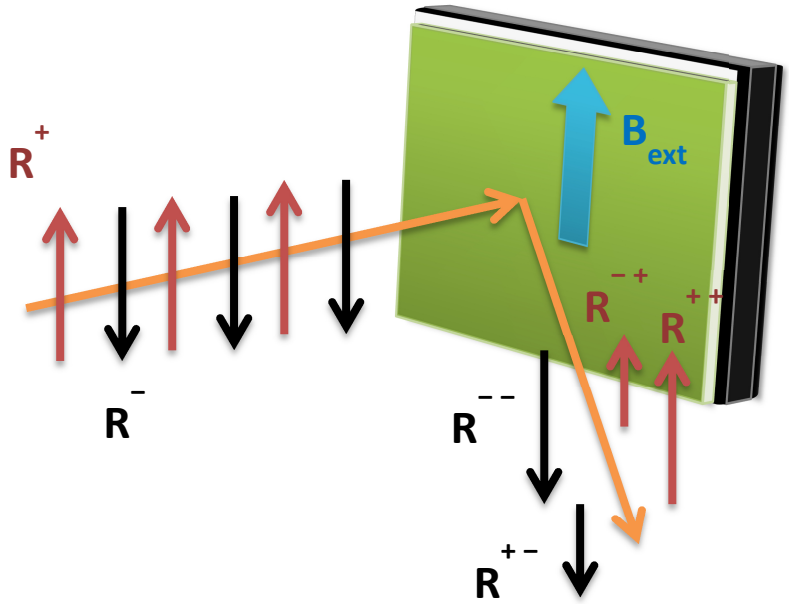

Figure 48: Configuration of PNR experiment. The sample ismagnetized in the plane of the sample using an external field. While the polarized neutrons are reflected from the sample's surface, the detector measures the reflected neutrons in four configurations, two non-spin-flip(R^{++} and R^{--}), and two spin-flip(R^{+-} and R^{-+}).

5.2. Neutron Reflectivity Experiments on Bit-Patterned Media

To better understand the vertical exchange coupling and the reversal mechanism, the PNR method was used to study the nuclear and magnetic depth profile of the ECC structure of the sample with Fe=2nm (Fig. 48). The Magnetism Reflectometer at beamline 4A, (Fig. 49), in the Spallation Neutron Source located at

Oak Ridge National Laboratory was used to measure the PNR from the sample [76]. In this beam line, the neutron beam gets polarized with polarizer mirrors, and the neutron spins always kept parallel (spin-up, +) or anti parallel (spin-down, -) to the applied field [77]. The experiment measured all spin configurations, R^{++}, R^{--}, R^{+-}, R^{-+} with respect to the scattering vector, q. The neutrons' wavelength is determined through the time of flight. Based on the reflection geometry, the neutron's transfer vector is only sensitive to the in-plane magnetization moment. As it mentioned previously, the sample has strong PMA, so the external field is required to rotate the magnetization in the plane of the sample for neutrons to interact during the experiment. Figure 50 show the hysteresis graph of the sample for both out-of-plane and in-plane configurations. To understand the reversal mechanism, the reflectivity experiment is carried out at three different fields of, A= 11.5, B=4, and C=0.5 kOe along the in-plane hysteresis loop (Fig.50).

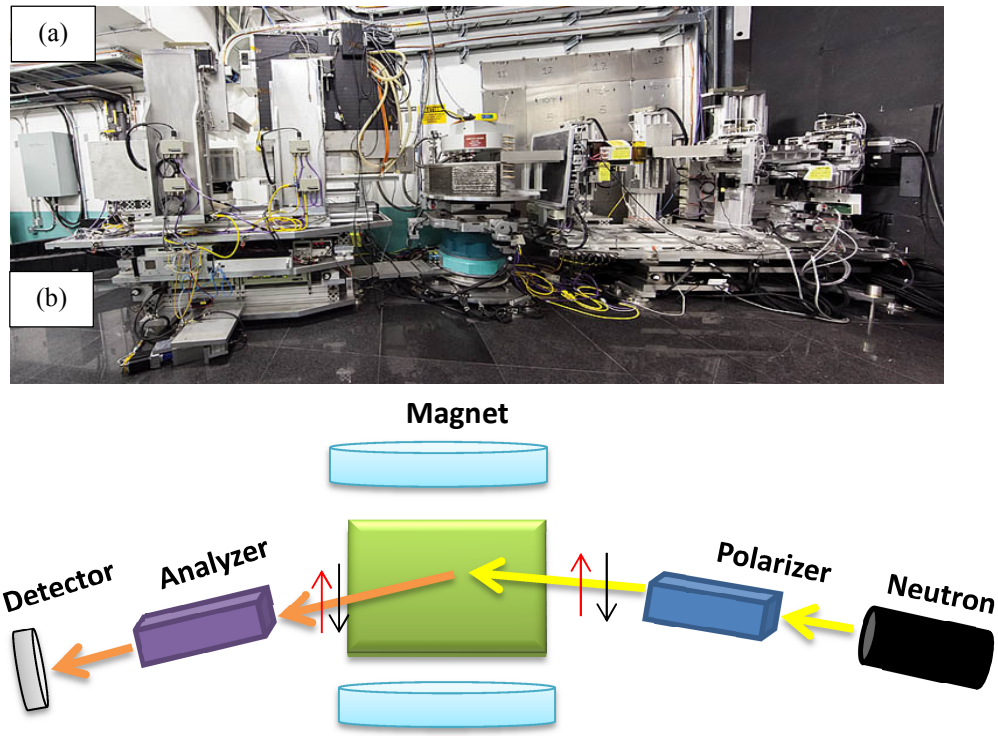

Figure 49: (a) panoramic view of the Magnetism Reflectometer, beamline 4A at the Spallation neutron Source in Oakridge National Laboratory. (b) Simplified schematic of the beam line setup.

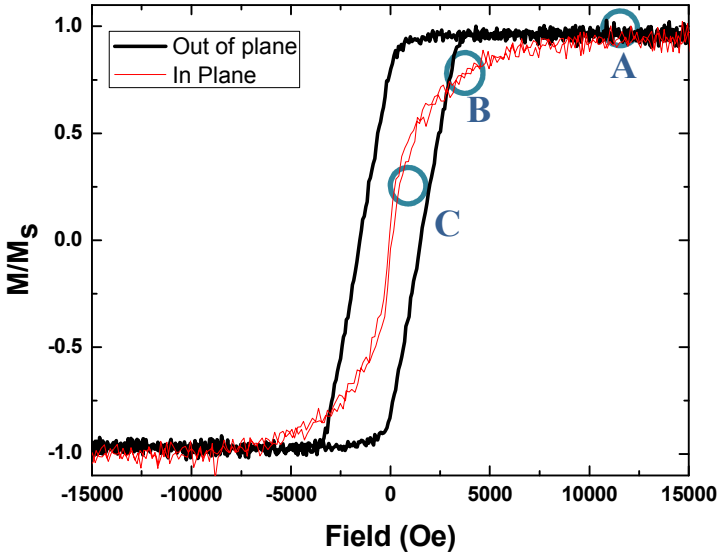

Figure 50: The measured hysteresis loops of sample with structure of Co(0.25 nm) / Pd (0.7 nm)]$_5$ / Fe (2 nm) / [Pd (0.7 nm) / Co (0.25 nm)]$_5$ for both out of plane and in-plane configurations. The points A, B and C refer to the external fields of 11.5, 4, and 0.5K respectively along the in-plane loops where the PNR experiment was carried out.

The results of the reflectivity measurements are corrected for the background signal. The spin-flip scattering was insignificant and was not included in the analysis. The reflectivity data for all three fields are shown in Fig. 51; where for each field the reflectivity of spin-up and spin-down neutrons with respect to q is plotted. The separation between the R^{++} and R^{--}, curves indicates a net magnetization within the sample. The solid reflectivity curves represent the result simultaneous fitting of R^{++} and R^{--}curves to a Parratt-type formalism [78, 79]. The 24 layers of structure were considered individually in fit to acquire an accurate fit. From the resulted fitted data, both nuclear and magnetic SLDs, $\rho_n(Z)$ and $\rho_m(Z)$, were extracted. The SLD of spin-up and spin- down as function of depth can be written as:

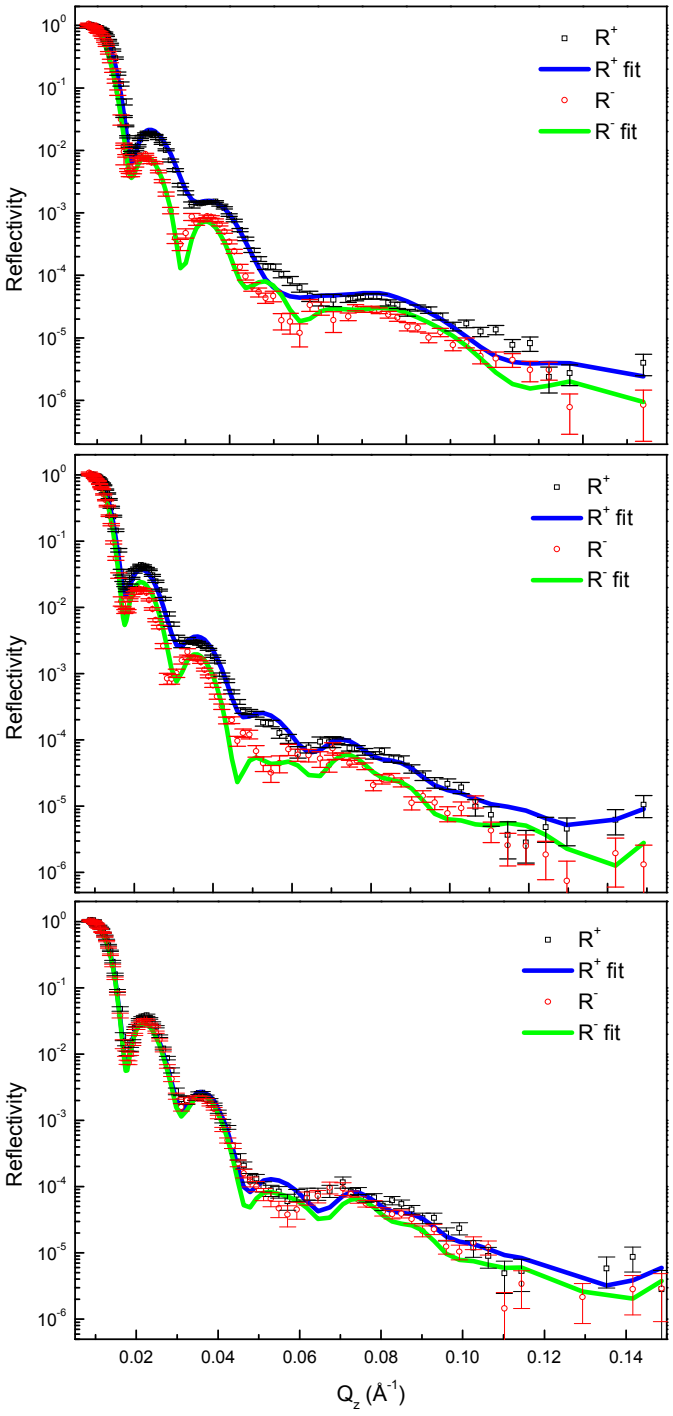

Figure 51: The reflectivity data vs. scattering vector for the sample with structure of Co(0.25 nm) / Pd (0.7 nm)]$_5$ / Fe (2 nm) / [Pd (0.7 nm) / Co (0.25 nm)]$_5$ that shows both R^{++} (black squares) and R^{--} (red dots) reflectivity and the solid lines are the fit to the data at 3 different fields: (a) 11.5 KOe, (b) 4KOe, and (c) 0.5 KOe.

$$\rho^{\pm\pm}(z) = \rho_n(Z) \pm C\rho_m(Z) \quad (59)$$

$$C = 2.853 \times 10^{-9}\ A^{\circ -2}\ \frac{cm^3}{emu}$$

By minimizing the χ^2 of the simulated reflectivity curves, the nuclear (Fig. 52) and magnetic (Fig. 53) was obtained. The nuclear SLD present the chemical composition profile and all layers can be identified as function of depth, Z. The 30nm of Carbon that is shown in the profile is to protect the islands from oxidation after patterning and it has no significant role in magnetic properties of the sample. At H=11.5 kOe, it can be concluded from the hysteresis loop that the magnetization of the sample is saturated in the plane of the sample and each layer magnetization is rotated into the sample plane, and this can be confirmed from the magnetic SLD as it shown in Fig. 53(a). This provides a measure of the saturation magnetization of each layer. At the intermediate field of H = 4 kOe, however as it shown in the magnetic SLD (Fig.53 (b)) the magnetization is non-uniform and there is a gradient in the magnetization of Co layers. As the Co moment rotates out-of-plane, the in-plane projection of the magnetic moment of the Co layers, as seen by neutrons will go down. Because of the high moment and low anisotropy of the Fe layer it tends to maintain its in-plane moment. The strong exchange coupling at the interface of Fe to the adjacent Co layers results in more in-plane magnetization in that region, but each successive Co layer rotates more out of plane in a structure similar to a domain wall. Finally at H=0.5 kOe (near zero field), the R^{++} and R^{--} does not show significant separation in their values except for a small amount in the higher q values which represent partial in-plane magnetization

which is confirmed in the magnetic SLD by showing that Fe layer is slightly tilted in-plane.

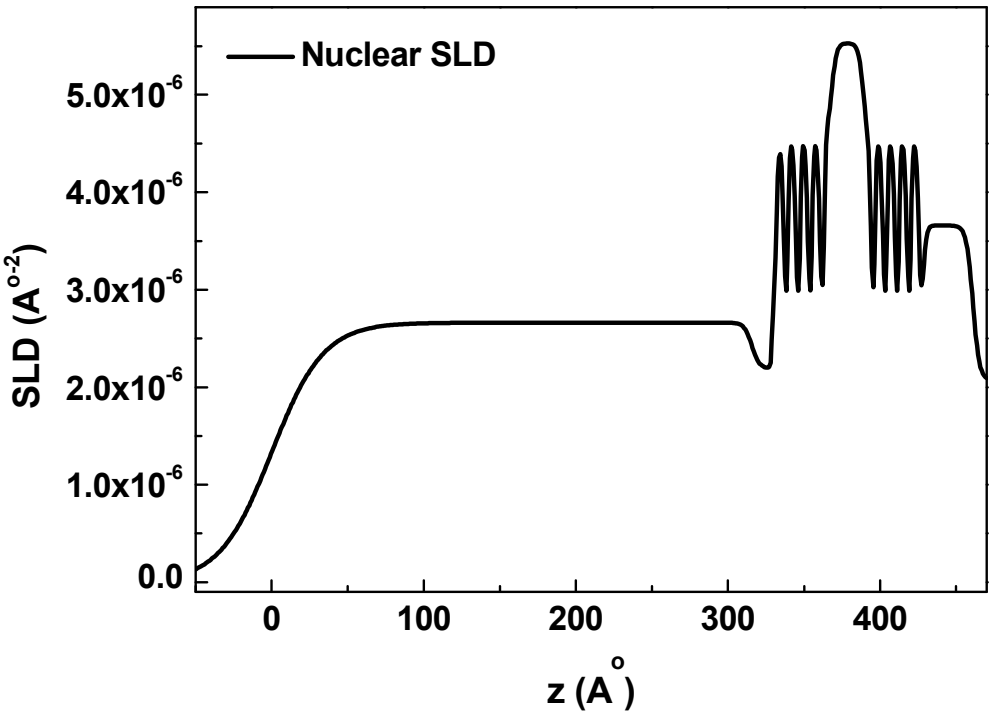

Figure 52: The nuclear SLD of sample with structure of Co(0.25 nm) / Pd (0.7 nm)]$_5$ / Fe (2 nm) / [Pd (0.7 nm) / Co (0.25 nm)]$_5$ which shows all the layers.

The PNR results at three different fields determined the behavior of magnetization structure of each layer at each corresponding fields. In particular at 4 kOe the result showed that the magnetization in Co layers is not uniform with a gradient in the out-of-plane Co anisotropy increasing with a distance from the central Fe layer. Further, from the data at 0.5 KOe it can be concluded that the shape anisotropy of the Fe layer is counteracted by the out of plane anisotropy of Co/Pd multilayer and results in Fe become nearly magnetically isotropic. The Fe layer does

not having a significant anisotropy and this layer can be pointed in any direction with a relatively small external field.

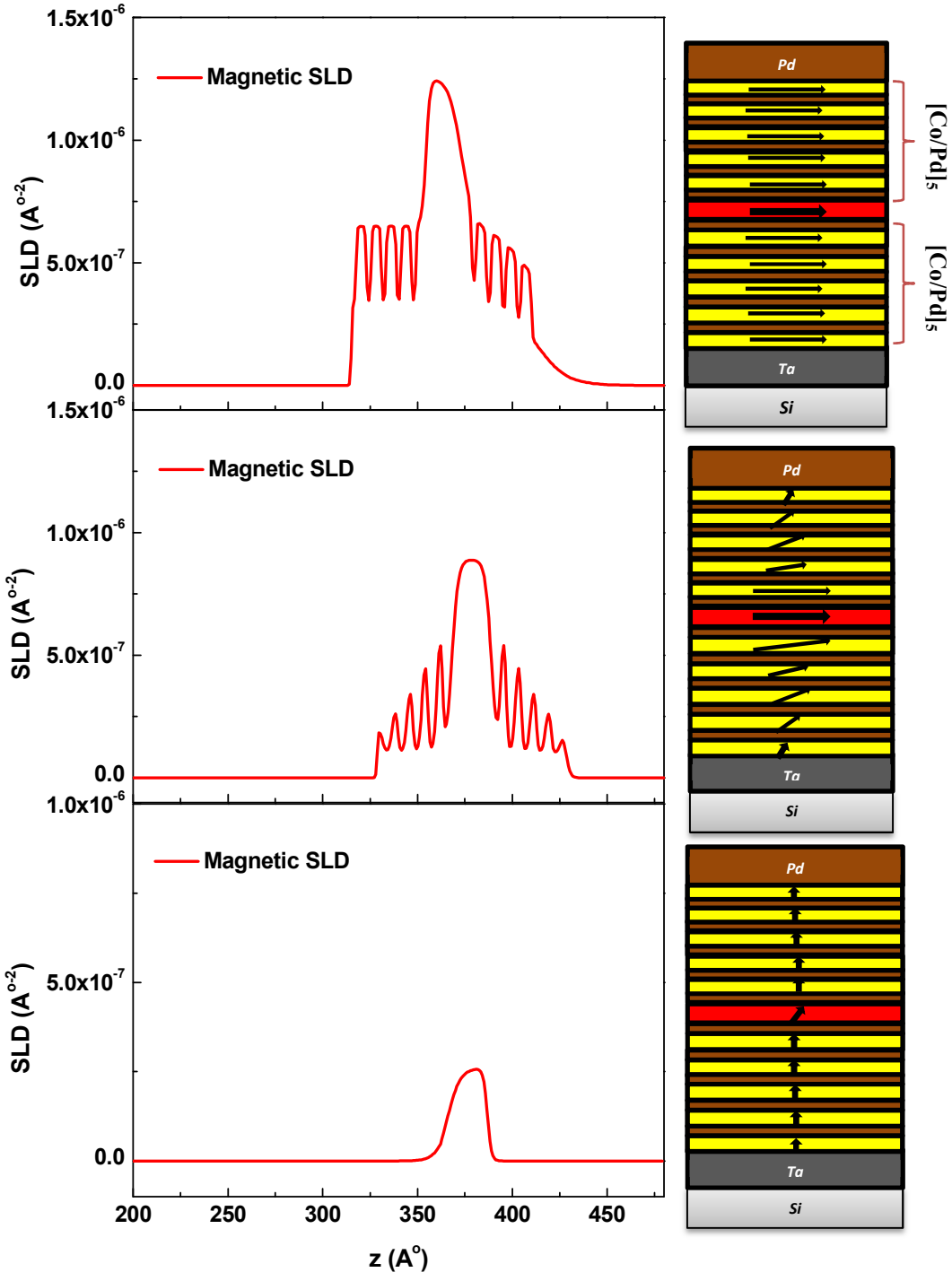

Figure 53: The magnetic SLD of sample with structure of Co(0.25 nm) / Pd (0.7 nm)]$_5$ / Fe (2 nm) / [Pd (0.7 nm) / Co (0.25 nm)]$_5$ at three fields: (a) 11.5, (b)4,and (c) 0.5 Koe and their corresponding schematic of the sample and the orientation of Co layers' magnetization, e, f,g respectively.

To complement the experiment, micromagnetic simulation of the sample was done using Fastmag, a finite element micromagnetic code [80]. The model has 10 layers of Co which are separated by layers of air (Pd layers) and the exchange field is included between adjacent Co layers. A layer of Fe is placed in between the Co stacks and separated by layers of air from the adjacent Co layers. While the sample is saturated out-of-plane (Z direction), an external magnetic field of 4 kOe is applied in the direction of in-plane (Y direction) and the magnetic moments are allowed to stabilized in the field. The first simulation included one island with diameter of 25 nm and the relaxed state showed a gradient in magnetic moment's angle of Co layers with regard to in-plane direction while the Fe layer tends to have mostly in-plane magnetization (Fig. 54. a). This simulation was repeated for five islands in a hexagonally-close-packed geometry (35 nm pitch) which showed similar results (Fig. 54.b). The simulation result is in agreement with the neutron experiment. In Table 6, the angles of Co layers with respect to in-plane magnetization are calculated and compared for both experiment and simulation results. The angles are calculated by comparing the magnetic moment of each layer at 4 kOe in plane field with it's out of plane saturation moment. Considering the fact that the neutron data reflects the average of magnetic islands and include the effect of dipolar field, the results are in good agreement.

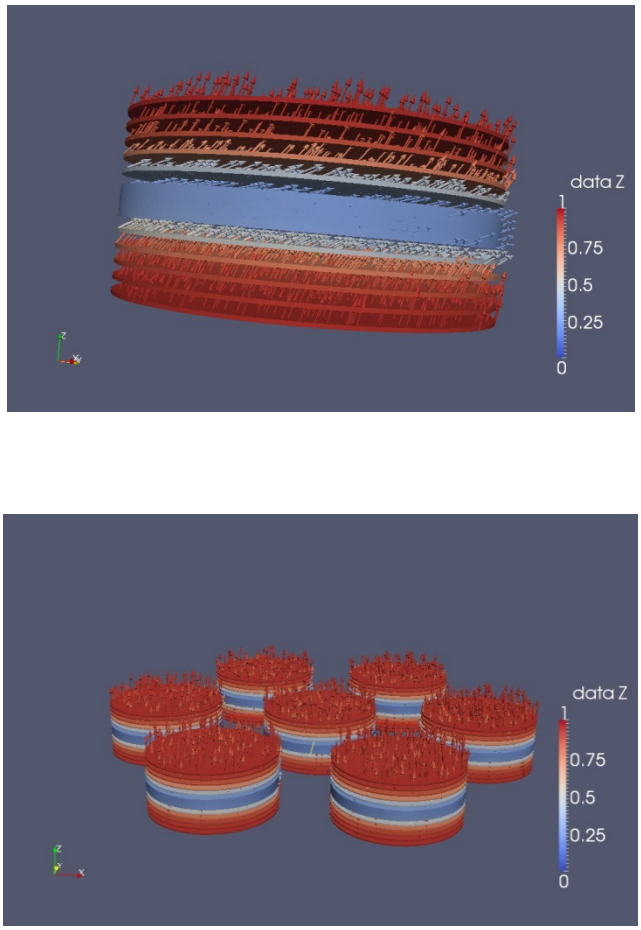

Figure 54: Micromagnetic simulation images of (a) 1 bit, and (b) multiple bits in form of hexagonal packed geometry. The images shows the magnetic islands at 4KOe in plane field and as it is shown there is a gradient in magnetic moment of Co layers.

Table 6: The Co layers magnetization angle with respect to in-plane magnetization at 4 kOe in-plane external field is calculated for neutron experimental data and is compared to the simulation results.

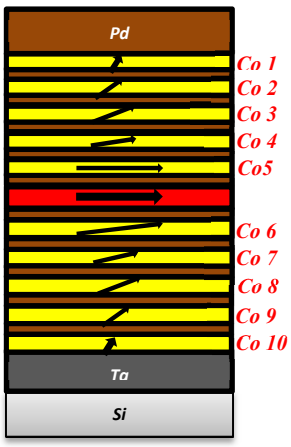

Co layers	Experimental angle (deg)	Single Bit Angle (deg)	Multiple Bits angle (deg)
Co 1	64	70	67
Co 2	44	68	66
Co 3	36	61	60
Co 4	21.5	48.5	47
Co 5	2	25	24
Co 6	16	25	24
Co 7	19	48.5	47
Co 8	23	61	60
Co 9	39	68	66
Co 10	59	70	67

Chapter 5, in part is currently being prepared for publication. N. Eibagi, S.W. Chen, H. Guo, S. Sinha, V. Lauter, and E.E. Fullerton. Smith, Laura; Smith, Jane D. I also would like to thank H.Ambaye, R. Goyetter and V. Lauter who helped me with neutron experiments in chapter 5. Research at Research at the ORNL Spallation Neutron Source ORNL was sponsored by the Scientific User Facilities Division, Office of Basic Energy Sciences, US Department of Energy. ORNL is managed by UT-Battelle, LLC, under contract DE-AC05-00OR22725 with the US Department of Energy.

Chapter 6: Dynamic Properties of Bit Patterned Media with Composite Structure

6.1. Ferromagnetic Resonance

Ferromagnetic Resonance (FMR) is a spectroscopic method to study magnetic systems at high frequencies and characterize their dynamic properties. Specifically this technique is being used to study thin magnetic films to probe their properties such as Gilbert damping, magnetic interactions and anisotropy [81, 82]. This method is very useful in the studying complicated magnetic systems and multilayers [83, 84].

6.2. Magnetization Dynamic

Magnetization dynamic is explained by the Landau and Lifshitz (LL) formula[83]:

$$\frac{d\vec{M}}{dt} = -\gamma\vec{M} \times \vec{H}_{eff} \tag{60}$$

$$\gamma = \frac{g|e|}{2m_e} \tag{61}$$

where M is magnetization vector and H_{eff} effective field that includes all interactions that contribute to the magnetic energy such as dipolar, exchange and anisotropy in addition to the external field and is given by:

$$E_{total} = \int \left(E_{external} + E_{stray} + E_{exchange} + E_{anisotropy}\right) dV \tag{62}$$

The effective field is then given by the curvature of the energy minimum:

$$H_{eff} = -\frac{\partial E_{tot}}{\partial \vec{M}} \tag{63}$$

γ is gyromagnetic ratio and it can be calculated based on Eq.61, where g is g-factor , e is electron charge and m_e is electron mass. Throughout this thesis the value of γ is considered constant, and the value for the isolated electron, $\gamma = 1.7609 \times 10^{11}$ rad/ s. T was used. If a single isolated electron is considered in a static field $H = H_{ext}\,\hat{z}$ the

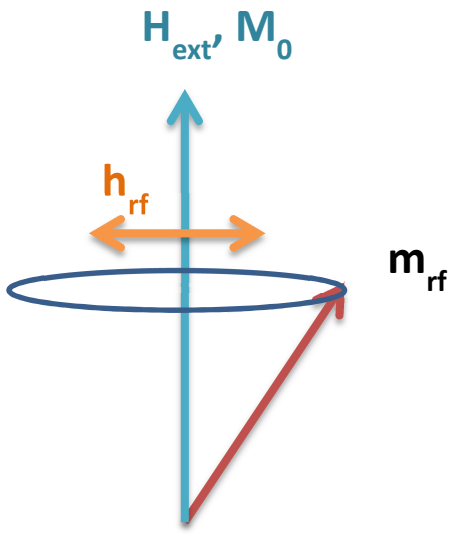

Figure 55: The schematic shows the processional motion of magnetization along the direction ofrf field which is perpendicular to the direction of the external field.

LL formula (Eq. 60) describes precessional motion about the direction of the field. The behavior results from the fact that magnetization has a corresponding angular momentum and a change of magnetization (left side of Eq. 60) results in a torque (right side of Eq. 60). The equation of motion can be solved for this system which results in three sets of equations:

$$\frac{d\overrightarrow{M_z}}{dt} = 0 \qquad (64)$$

$$\frac{d\overrightarrow{M_x}}{dt} = \gamma H_{ext}.M_y \quad (65)$$

$$\frac{d\overrightarrow{M_y}}{dt} = \gamma H_{ext}.M_x \quad (66)$$

The solution for this sets of equations represent that magnetization in $\hat{x}$ and $\hat{y}$ have oscillatory motion with frequency equal to:

$$\omega = \gamma H_{ext} \quad (67)$$

where ω is called Larmor frequency.

To understand the effect of the resonance, a small RF field, h_{RF}, is considered perpendicular to the H_{ext} as it shown in Fig. 55, The contribution of the RF field should be considered in the total field and magnetization in the equation of motion:

$$\vec{H}_{eff} = \vec{H}_{ext} + \vec{h}_{RF} \quad (68)$$

$$\vec{M}_{eff} = \vec{M}_{\circ} + \vec{m}_{RF} \quad (69)$$

It should be considered that $h_{RF} << H_{ext}$ and as a result $m_{RF} << M_o$. Equation 60 can be solved for the system:

$$\frac{\partial \vec{M}_{\circ}}{\partial t} = 0 \quad (70)$$

$$\frac{\partial \vec{m}_{rf}}{\partial t} = -\gamma(\vec{m}_{RF} \times \vec{H}_{ext} + \vec{M}_{\circ} \times \vec{h}_{RF}) \quad (71)$$

Equation 71 suggests that the solution for m_{RF} and h_{RF} both have sinusoidal time dependence form ($\sim e^{i\omega t}$) . Considering the form of the solution the Eq. 71 can be rewritten as:

$$i\omega m_x = -\gamma\left(m_y H_{ext} + M_{\circ} h_y\right) \quad (72)$$

$$i\omega m_y = -\gamma\left(m_x H_{ext} + M_{\circ} h_x\right) \quad (73)$$

Equations 72 and 73 can be rearranged and solved for magnetization to have the form of:

$$m = \chi h \tag{74}$$

where χ is dynamic susceptibility and it has a complex form:

$$\chi = \chi_{re} + i\chi_{im} \tag{75}$$

$$\chi_{re} = \frac{\gamma^2 M_\circ H_{ext}}{\gamma^2 H_{ext}^2 - \omega^2} \tag{76}$$

$$\chi_{im} = \frac{\gamma M_\circ \omega}{\gamma^2 H_{ext}^2 - \omega^2} \tag{77}$$

When the frequency of the oscillating field equals to Larmor frequency, resonance occurs and the susceptibility diverges. At resonance, the magnetization absorbs energy from the oscillating field and starts to precess at a larger angle around H_{ext}, this phenomenon is called ferromagnetic resonance [85].

6.2.1. Magnetic Thin film

As it mentioned earlier FMR is a technique that is often used for studying magnetic thin films. A magnetic thin film sample with in plane magnetization in an external field is considered (Fig. 56). Within the magnetic sample, the effective field, H_{eff}, is the sum of the external field, H_{ext}, demagnetization field, H_d, and anisotropy field, H_a:

$$H_d = N.M\,,\ H_a = \frac{2k}{M_S},\ H_{ext} = H_{ext}\hat{y}$$

The demagnetization factors, N, as discussed before (Sec. 2.2.3) can be determined based on the geometry of the sample. The LL equation (eq.60) can be written for the film as[86] :

$$\frac{dM_z}{dt} = 0 \tag{78}$$

$$\frac{dM_x}{dt} = \gamma\left[H_{ext} + \frac{2k}{M_S} + (N_y - N_z)M_S\right]M_y \tag{79}$$

$$\frac{dM_y}{dt} = \gamma\left[H_{ext} + \frac{2k}{M_S} + (N_x - N_z)M_S\right]M_x \tag{80}$$

A sinusoidal solution is considered and it can be concluded that the resonance frequency is:

$$\omega_{res} = \gamma^2\left[H_{ext} + \frac{2k}{M_S} + (N_y - N_z)M_S\right]\left[H_{ext} + \frac{2k}{M_S} + (N_x - N_z)M_S\right] \tag{81}$$

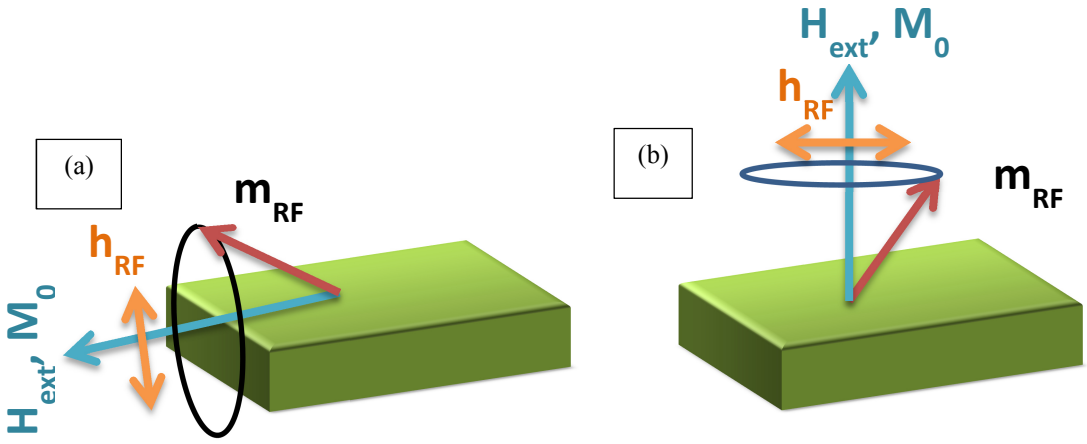

Figure 56: The schematic shows the configuration for FMR in thin films: (a) In-plane anisotropywhere shape anisotropy affects the resonance frequency and (b) Out-of-plane anisotropy where the PMA increases the resonance frequency while the shape anisotropy decreases it.

The demagnetization factors can be defined based on the geometry and the magnetization of the sample. For a film with in-plane magnetization and external field parallel to the surface of the film (Fig.56 (a)), the demagnetization factors are $N_x=N_z = 0$, and $N_y =4\pi$, and as a result:

$$\omega_{res} = \gamma\sqrt{(H_{ext} + \frac{2k}{M_S})(H_{ext} + \frac{2k}{M_S} + 4\pi M_S)} \quad (82)$$

For a sample with perpendicular magnetization and external field perpendicular to the surface of the sample (Fig. 56 (b)), the demagnetization factors are $N_x=N_y=0$, and $N_z = 4\pi$, and as a result:

$$\omega_{res} = \gamma(H_{ext} + \frac{2k}{M_S} - 4\pi M_S) \quad (83)$$

In the sample with PMA, the effective anisotropy is defined as:

$$H_{k_{eff}} = \frac{2k}{M_S} - 4\pi M_S \quad (84)$$

If the value of H_{keff} is positive, $H_{keff} > 0$, then the sample has perpendicular anisotropy and if $H_{keff} <0$, then the sample has in plane anisotropy, the same as sec.2.2.4 . As a result the effective anisotropy of a complicated sample can be determined by solving the equation of motion.

6.2.2. Damped Motion

Based on the LL formula (eq.60), the precessional motion of magnetic moment would continue forever unless the magnetization starts from the direction of H_{ext}. However, in experiment the magnetization would align with the direction of the

applied field eventually to minimize the energy independent of the relative position of the initial magnetization with respect to the external field. This suggests that the processional motion of the magnetization is actually damped. Gilbert modified the LL formula by adding an additional term to account for dissipation yielding the modified equation of motion is the LLG formula [87]:

$$\frac{d\vec{M}}{dt} = -\gamma\vec{M} \times \vec{H}_{eff} + \frac{\alpha}{M_s}(\vec{M} \times \frac{d\vec{M}}{dt}) \quad (85)$$

where α is dimensionless positive damping constant (known as the Gilbert damping constant) and represents dissipation of energy with motion of the magnetization. The damping parameter affects the resonance characteristics of the sample under the study such as the linewidth (full width at half maximum FWHM) of the resonance peak. However, α doesn't significantly affect the resonant frequency which is mostly neglected in calculation of resonant frequency in many cases and throughout this thesis. The resonant peak can be shown based on the dynamic susceptibility which was solved for a simple case of the isolated electron. However, for a complicated system, magnetic thin films, the full LLG equation can be solved and the complete dynamic susceptibility tensor can be extracted [88]. The χ would not diverge at resonance but the imaginary part would show a peak at the resonance and the linewidth is defined as FWHM of this peak. The relation of the damping parameter and the resonance linewidth, ΔH, is expressed as [89]:

$$\Delta H = \Delta H_{\circ} + \frac{4\pi\alpha}{\gamma} f \quad (86)$$

where f is the frequency , and ΔH_o represent the sample inhomogeneities that provides a frequency independent contribution to the linewidth in addition to α. The value of α for ferromagnetic thin films is in the range of 0.001-0.3[90].

6.3. Ferromagnetic Resonance Experiment

There are many ways to carry on an FMR experiment. In this thesis the FMR experiment was done using a Vector Network Analyzer (VNA) and coplanar waveguide (CPW) technique [91]. A VNA is used to generate RF current which through a coplanar waveguide to produce RF magnetic fields. The experimental method was based on fixed frequency and DC field sweep. In this way we can extract the field linewidth of the resonance for various frequencies an fit them to Eq. (86). The VNA is a signal generator that can generate range of low to high frequency signals by setting both amplitude and frequency while it can measure both amplitude and phase properties in addition to scattering parameters (s parameters). S parameters relate the incident and reflected powers of RF current. A two port VNA is able to measure four s parameters through which the incident and reflected powers would be analyzed. The s parameters are two transmitted (S_{12} and S_{21}) and two reflected (S_{11} and S_{22}) powers, which are represented as a matrix:

$$S = \begin{bmatrix} S_{11} & S_{12} \\ S_{21} & S_{22} \end{bmatrix}$$

The indices represent the port numbers and the first index represents the outgoing power from that port and the second represent the input power. The value of S is the

ratio of these two powers. S parameters are proportional to the dynamic susceptibility that the resonant and damping parameters can be extracted from them.

The experiment setup is sketched in Fig. 57. The VNA is A two port VNA, Agilent E8363B, which generate frequency span of 100 MHz to 40 GHz. The VNA

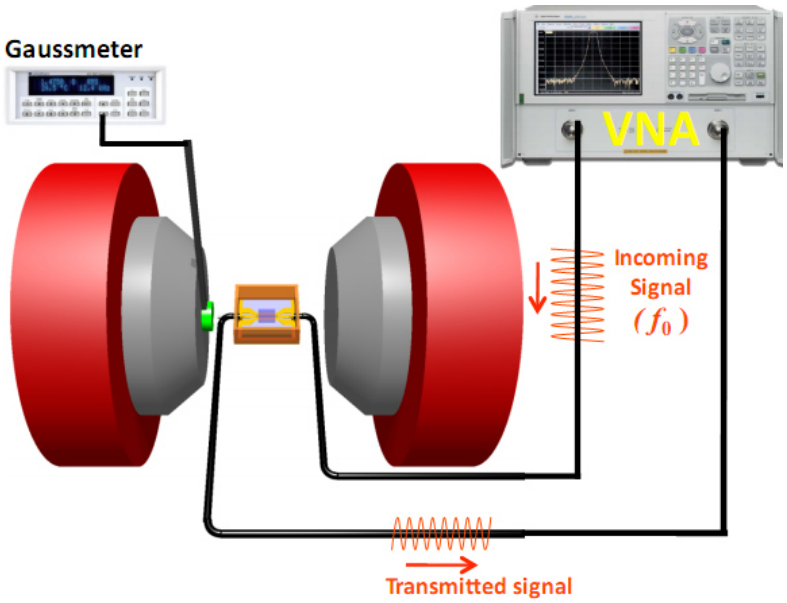

Figure 57: A schematic of FMR set up. The VNA is used to generate the RF signal to the.waveguide which produce RF magnetic field, and DC Magnet aligns the magnetic moment of the sample

sets the requested frequency and the amplitude of the signal is set by the power. A set of coaxial cables with SMA connectors and characteristic impedance of 50 Ω is used to apply and measure the RF current. These cables connect to the ports of the VNA from one side and the other side is connected to CPW using Picoprobe microwave probes which transfer the current from SMA connectors to three spring loaded tips (separated by 200 μm) with the geometry of ground-signal-ground (Fig. 58), and the

alternative is to connect the SMA connector to the waveguide by soldering. The CPW is usually fabricated on high permittivity (ε_r) substrates like GaAs (ε_r=12.9) or PCB board.

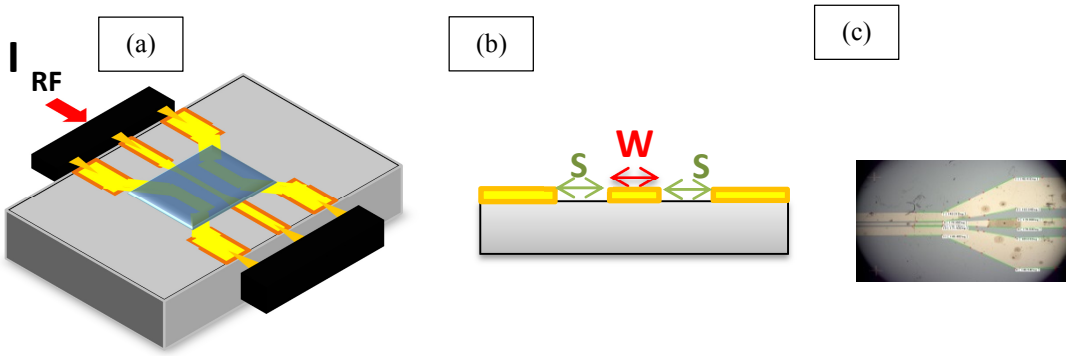

Figure 58: Schematic of copalanar waveguide: (a) the connectionof microwave probes to the waveguide and sample is placed face down on the waveguide. (b) The side view of CPW that the signal line with width of W is separated from the ground lines with spacing of S. (c) the microscope image of part of a waveguide.

The dimensions of the CPW, the signal line width, w, and spacing, s, (Fig. 58 (b)) is calculated using the online calculator [92] to ensure the characteristic impedance of 50 Ω which would minimize the loss and reflected power at the interfaces. The sample is placed face down on the CPW, and the combination of the sample and CPW is placed within poles of the DC magnet in a way that the DC field is perpendicular to the surface of the sample and the RF field is orthogonal to the DC field. The external field is applied through an electromagnet, and the magnetic field is being detected by a Hall probe. The DC field aligns the magnetic moments of the sample. As a result it is

important to make sure the components are nonmagnetic to prevent the distortion in the result.

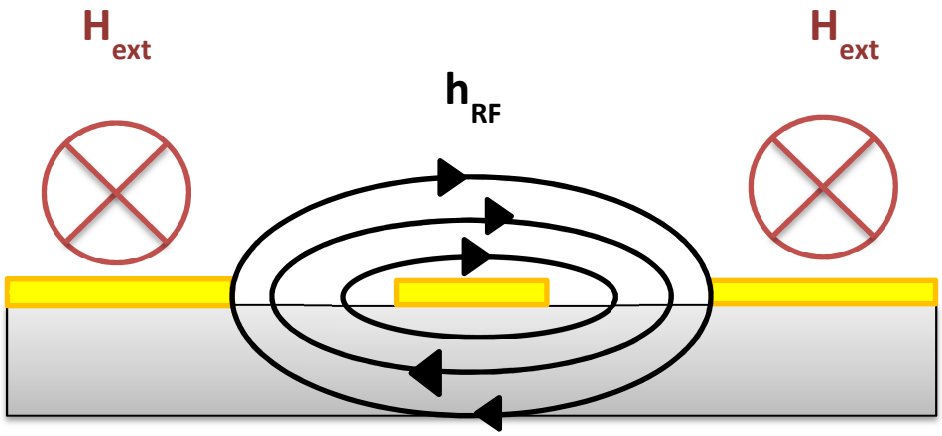

Figure 59: Generate RF field around the signal line of CPW and its orientation with respect to the external field is shown.

The FMR experiment was done on the BPM samples with composite structure of Ta (2_{nm}) / [Co(0.25_{nm}) / Pd (y)]$_5$ / Fe (x) / [Pd (y) / Co (0.25_{nm})]$_5$ / Pd (1_{nm}) where X =1,1.5, and 2 nm (Sec.4.3). During the experiment the VNA was set to generate a RF current with a fixed frequency in the range of 5-18GHz, the external field is swept from -7.5KOe to +7.5KOe to pass through the resonance condition, and both real and imaginary parts of the S parameters are measured. The RF current produces oscillating magnetic field around the signal line of the CPW (Fig.59). The RF field direction is in the plane of the sample, and it is orthogonal to the external field. When the RF field frequency is equal to the precession frequency of the magnetic moment, resonance occurs and the magnetic moment absorbs energy from the RF field and precesses at

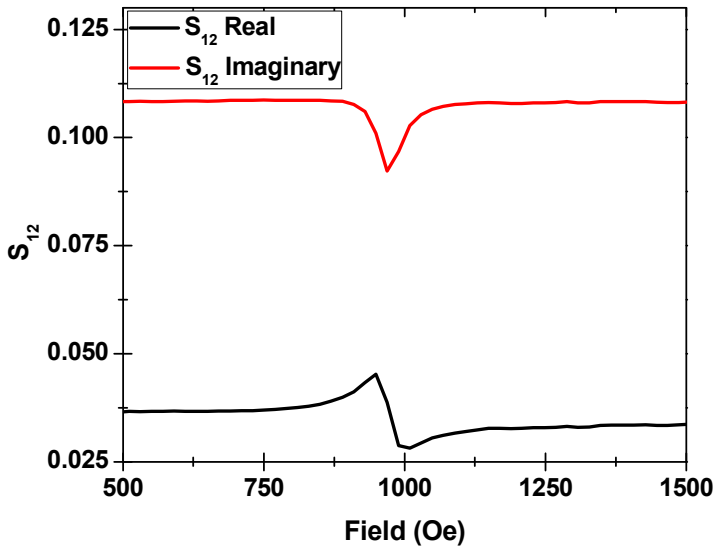

Figure 60: The real (black) and imaginary (red) S_{12} signal, and the dip in the imaginary part shows the resonance.

a larger angle. As a result there is sharp decrease in the power of S_{12} parameter (Fig. 60) [93].

Throughout the experiment, the transmitted signal, S_{12}, was considered for data analysis. The FMR signal considered as magnitude of S_{12} which calculated using both real and imaginary parts:

$$|S_{12}| = \sqrt{(\mathrm{Re}(S_{12}))^2 + (\mathrm{IM}(S_{12}))^2} \quad (87)$$

and series of $|S_{12}|$ signals at different frequencies versus external field is graphed in Figure 61 which belong to the sample with structure of $[Co(0.25\ _{nm}) / Pd\ (y)]_5$ /Fe (2_{nm}) / $[Pd\ (y) / Co\ (0.25\ _{nm})]_5$. The dip in the signal shows the resonance, and the

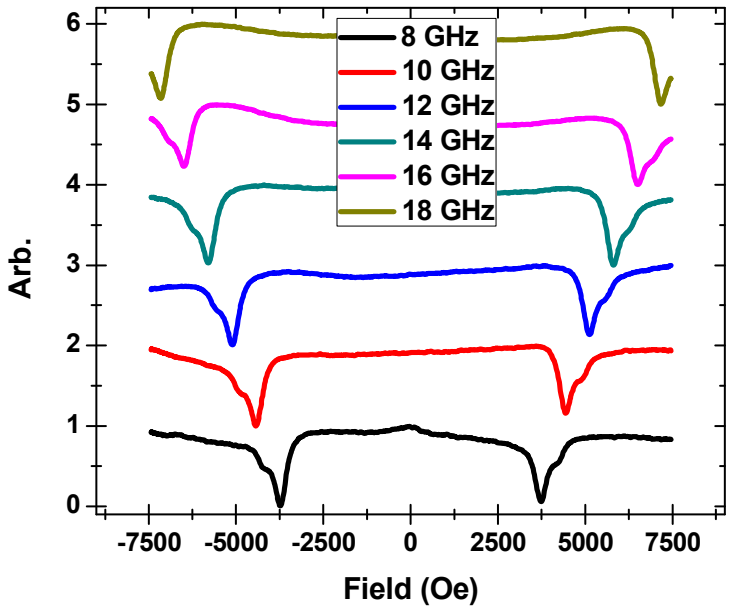

Figure 61: The measured magnitude of S_{12} signal determined using Eq. 81 versus field. The sharp decreases in the signal shows the onset of FMR.

resonance field is almost symmetric. Figure 62 shows the $|S_{12}|$ for the patterned sample with different Fe thickness at frequency of 18GHz. The linewidth of the peak is increasing by decreasing the Fe thickness and the resonant field decreases. To extract the linewidth and resonance fields at each frequency, the $|S_{12}|$ signal for the negative range of field (0 to -7500 Oe) at different frequencies (5-18 GHz) was fitted to the modified Lorentzian function:

$$S_{12} = y_{\circ} + \frac{2A}{\pi}\frac{\Delta H}{4(H-H_{res})^2+\Delta H^2} + \frac{2A}{\pi}\frac{2(H-H_{res})}{4(H-H_{res})^2+\Delta H^2} \quad (88)$$

where y_0 is an offset, A and B are the fitting parameter, ΔH is the linewidth of the signal's peak, and H_{res} is the resonant field. The extracted values of ΔH versus

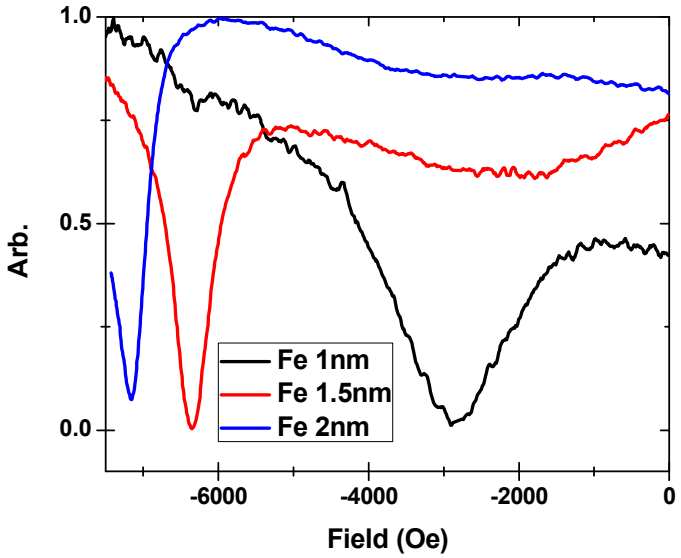

Figure 62: The FMR peaks at frequency of 18Ghz for samples with structure of [Co (0.25 nm) / Pd (y)]$_5$ /Fe (x) / [Pd (y) / Co (0.25 nm)]$_5$ where x = 1,1.5, and 2 nm.

Table 7: The dynamic properties of patterned sample with composite structure of [Co/Pd]/Fe (x)/ [Pd/Co] for various Fe thickness

Properties	Fe =1.5 nm	Fe =2 nm
α	0.0136	0.0103
ΔH_0 (Oe)	300	443
H_{keff} (Oe)	-974	-163

frequency (Fig. 63) was fitted to eq. 86 to extract the damping parameter, α, and inhomogeneity, ΔH_0 for samples (Table. 7). The FMR result's SNR from the sample with structure [Co(0.25 $_{nm}$) / Pd (y)]$_5$ / Fe (1$_{nm}$) / [Pd (y) / Co (0.25 $_{nm}$)]$_5$ was low due to

very thin layer of Fe, so the FMR parameters weren't analyzed. The damping parameter, α, and H_{Keff} values indicate that the FMR signal is mostly due to the Fe layer however, but the resonant fields are shifted by coupling to the [Co/Pd] multilayers. The ΔH_0 values are fairly low for both samples; however it is lower for the sample with Fe layer with thickness of 1.5nm. To extract the anisotropy field, H_{keff}, for the samples, the extracted resonant field (Eq. 88) versus frequency was fitted (Fig. 64) to Eq. 83 since the geometry of the sample is similar to Fig. 56(b) and the extracted values are shown in Table.7. Both H_{keff} values are negative which confirm the total perpendicular anisotropy of the samples. The sample with 2-nm of Fe has a very small H_{keff} which confirms that Fe's shape anisotropy is nearly canceled by the [Co/Pd] PMA and as a result the Fe layer behaves as if it is isotropic. The same behavior of the Fe layer was confirmed through neutron experiment in pervious chapter (Sec. 5.2.).

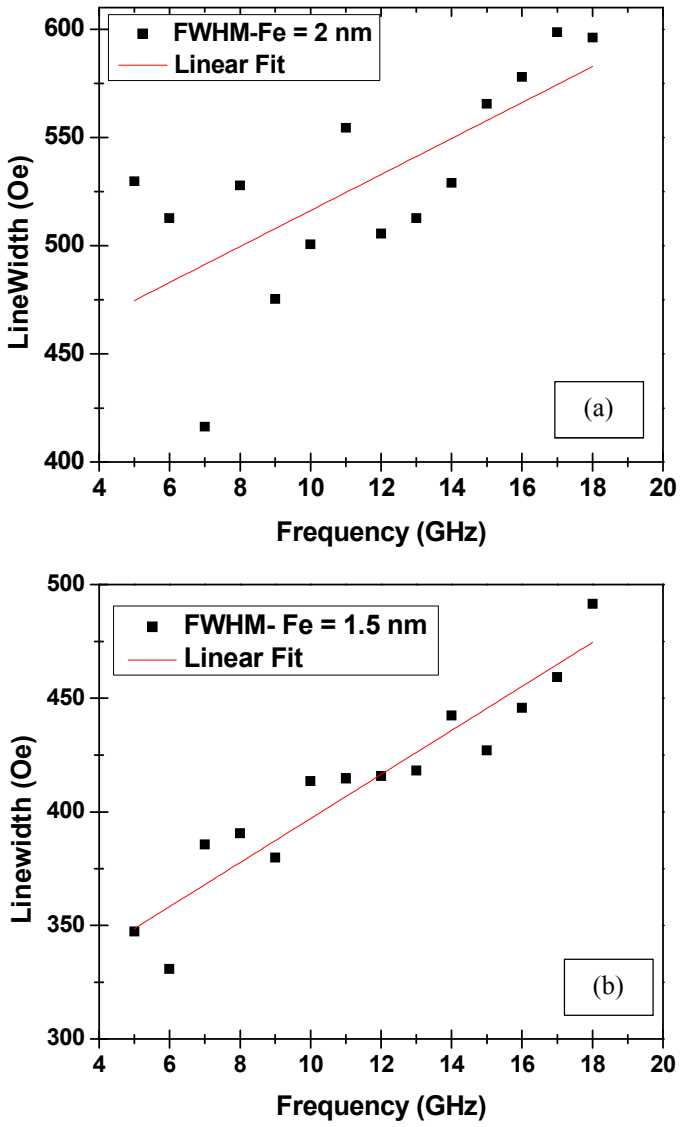

Figure 63: Linewidth (FWHM) of FMR peaks vs. the frequency for sample with structure of (a) x=2nm and (b) x=1.5nm. The solid line is the linear fit (eq.80) to the data to extract damping parameter

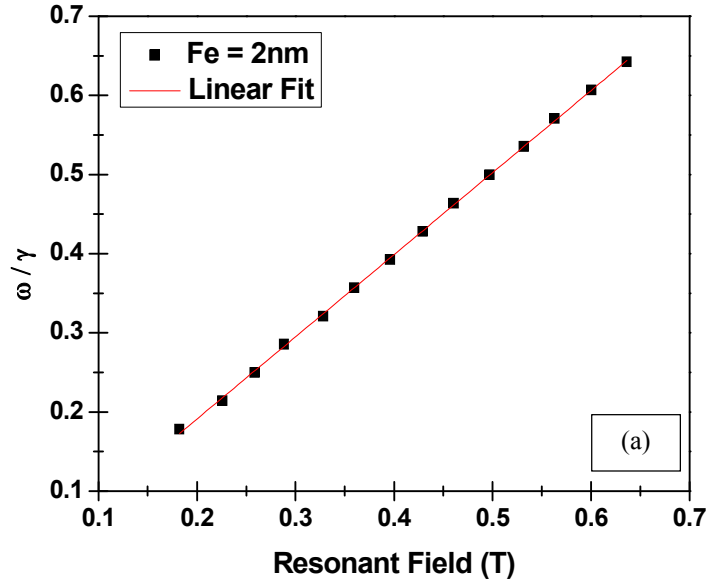

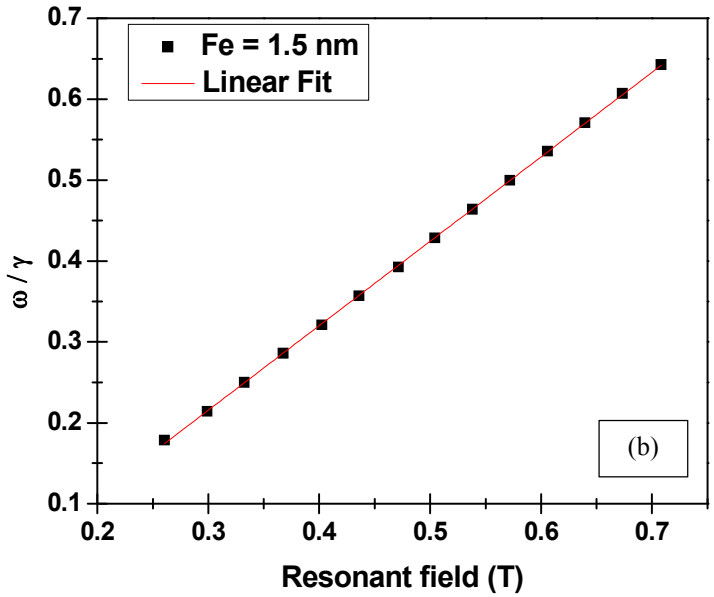

Figure 64: The frequency vs. resonance field data for sample with structure of (a) x=2nm and (b) x=1.5nm. The solid line is the linear fit (eq. 83) to data to extract the effective anisotropy of the samples.

6.4. Microwave Assisted Magnetic Recording

Microwave assisted magnetic recording (MAMR) is another promising technology to expand the future storage areal density. MAMR takes advantage of the concept of FMR and uses microwave field along with DC external field to reduce the switching field [24,83]. This method allows reducing the grain size while ensuring thermally stable bits by using magnetic materials with high anisotropy, and the writability challenge is addressed by using microwave field to reduce the switching field.

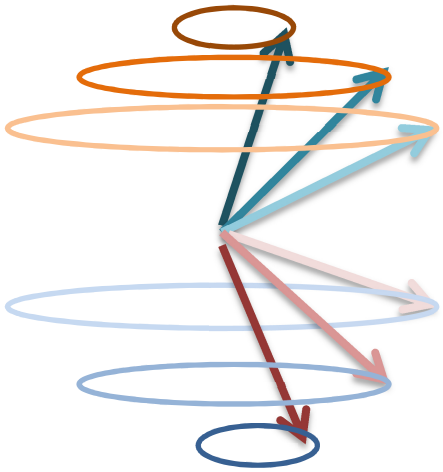

Figure 65: The precession and switching of magnetic moment in the present of microwave field

A specimen that is saturated along its easy axis is considered and when a DC field is applied in the opposite direction along the easy axis, the sample follows its normal loop with a specific and rather high coercive field, H_C. However, adding an AC

field with angular frequency of ω along an axis orthogonal to the direction of external field, the magnetization would go through precession (Sec.6.2). If the AC field frequency equals the resonance frequency, FMR happens and the system absorbs energy from AC field and magnetization presses at a larger angle and then the magnetization reverses (Fig. 65) at a new switching field, H_C' , which is much lower than the normal H_C. The goal of this method is that H_s' is in the range of conventional write field. The resonance frequency depends on the DC and anisotropy field of the sample. It should be concerned that when the resonance phenomenon happens, the rate of energy absorption should be higher than damping and its strength should be high enough to overcome the energy barrier.

6.5. Experimental Methods

The exchanged-coupled composite structure provide unique opportunity to be used for MAMR. The microwave fields couple to the soft layer at much lower frequency and drives the layer in to the resonance, then the energy is transferred from the soft layer to the hard layer through exchange coupling and drives the hard layer into resonance, and eventually the whole system is switched as a unit at lower frequency and field[94]. This also can be used to make multilevel recording systems where the selective writing of different layers is achieved by tuning the resonant frequencies. The BPM samples with composite structures of [co/Pd]/Fe/[Pd/Co] in this thesis have potential to be combined with MAMR technology. The microwave field

couples to the Fe layer through which the microwave energy is absorbed into the hard layers of [Co/Pd] and it would assist the switching. This approach has the advantage that the resonant field can be tuned independently of the anisotropy of the hard layer. If only a hard layer would be used then the resonant field would be so high that it be impractical to generate the high frequency signals. Two different experimental methods were used to study the effect of the microwave assisted fields on the samples with such structures. The first method used magneto optical Kerr effect (MOKE) to probe the magnetization while the continuous RF current was applied using signal generator. The second method used extraordinary Hall effect to probe the magnetization, and instead of continuous field, trains of RF pulses was used to pump the system.

6.5.1. Magneto Kerr Effect and Continuous RF Current

In this experimental technique a similar set up as used for FMR measurements was used and a polar MOKE set up was added to the system (Fig. 66). The Agilent signal generator E4405B which is capable of generating continuous RF current with frequency range of 9 KHz to 13.5 GHz was used. To increase the applied RF field, the signal's power was amplified. The input power was monitored through a directional coupler and power meter before entering the coplanar waveguide. The waveguide that was used in this experiment have the same configuration (ground-signal- ground)

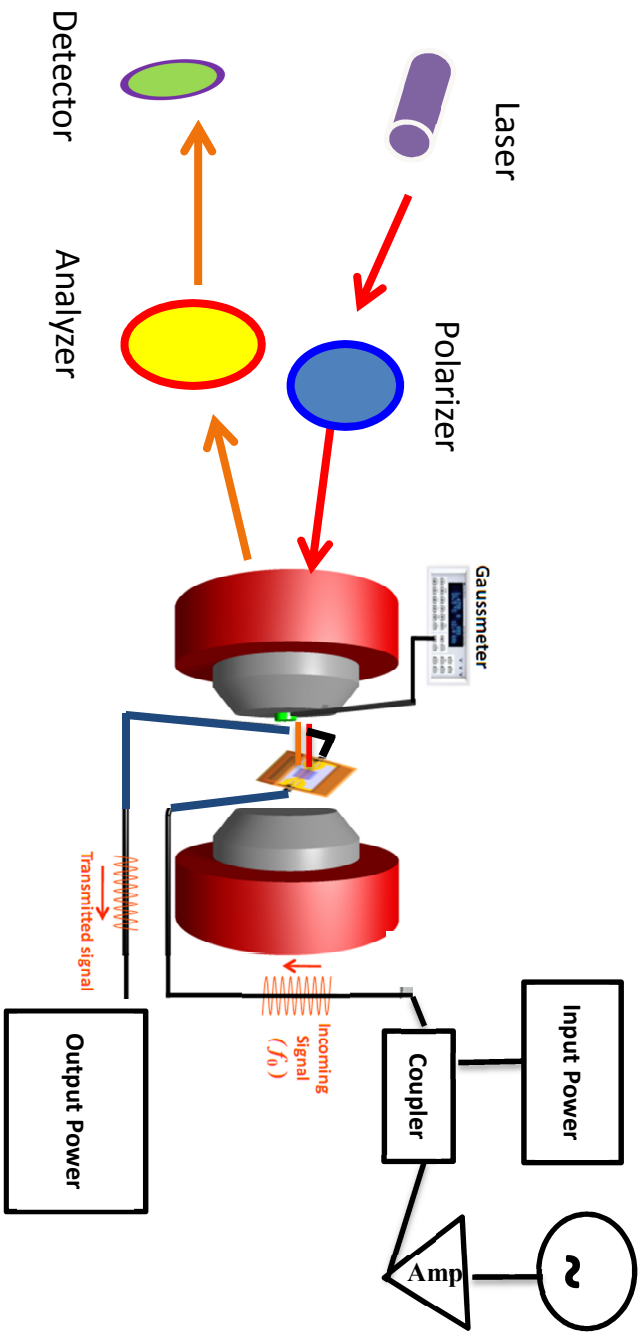

Figure 66: Schematic of MAMR experimental setup

as the one used for FMR experiment (Sec. 6.3); however, this waveguide fabricated on two side polished C-plane sapphire substrate with $\varepsilon_r = 11.6$, and as a result the value of the signal line width, w and the spacing, s was recalculated base on the properties of the substrate. The waveguide was fabricated using the photolithography technique (Sec.3.3), and the metal is sputtered using AJA dc magnetron sputtering technique (Sec. 3.2) and its configuration is Pt 5nm / Au 400 nm/ Pt 5nm. The signal was carried to waveguide using the same microprobe that was used in FMR experiment. The output power was monitored by feeding the signal out of waveguide to a second power meter. The sample was placed face down on the waveguide and the combination of the waveguide and sample was place in middle of the DC magnet in the same configuration as FMR setup to ensure the DC field to be perpendicular to the surface of the sample and orthogonal to the h_{RF}. The MOKE section of experiment was placed in a way that the laser would shine from back of the waveguide through the spacing between the signal line and the ground lines to the sample, and the change in intensity of rotated polarization of light (Kerr effect) was measured using a diode detector. The frequency and power of the RF current is fixed and the continuous RF current is applied while the dc field sweeps from -7KOe to +7KOe and the Kerr signal is being measure in parallel. With this experimental set up, half of major loop of the sample is measured at different RF frequencies and powers. Figure 67 shows graphed loops at 2 GHz for various input powers. Although there is about 1300 Oe (50%) improvement in switching field at 32dbm, the lower switching field is both due to sample heating and microwave field effect. Since continuous current with high power was used in this

experiment, the sample is heated, and this was confirmed by using a thermocouple. The magnetic signal that was measured thorough MOKE, is the average signal from magnetic islands which are located at the spacing in the waveguide, and as it mentioned in section 6.4. the RF field is more effective above the signal line, where the laser is blinded due to the signal line. The laser beam reflects from the sample

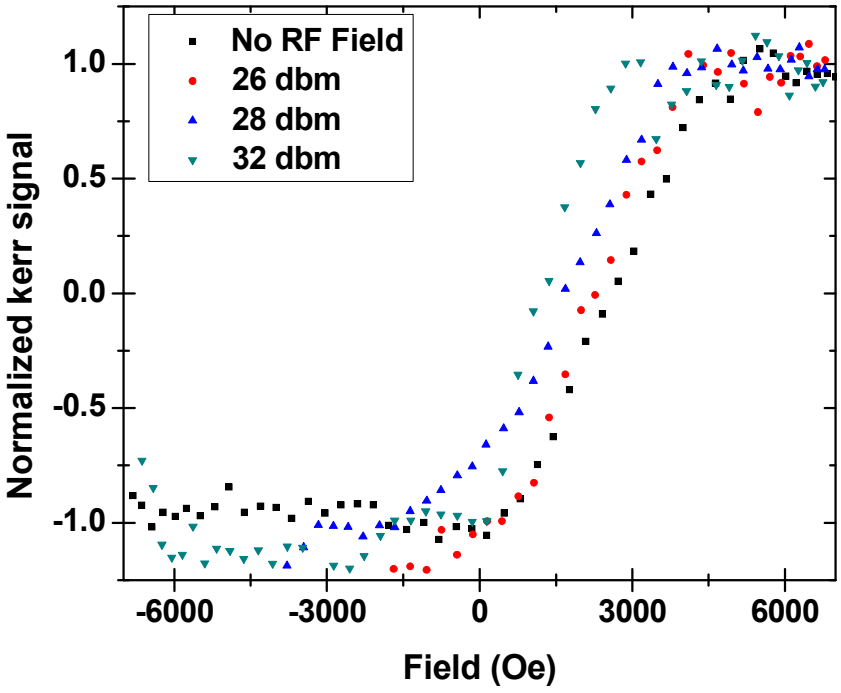

Figure 67: Half major loop measurement of sample with structure of $[Co/Pd]_5$/Fe 2nm/ $[Pd/Co]_5$ with MOKE at 2GHz but different microwave powers.

surface through the spacing area of the waveguide (Fig.59). As a result, it is not confirmed that the reflected beam provide the magnetic status of the islands which are directly perturbed by the maximum RF field produced by the waveguide. To improve

the experiment, in the next section Hall Effect was used instead of MOKE to measure the change in the magnetization of the area of interest, and a pulse generator was used to avoid the sample heating.

6.5.2. Hall Effect and Pulsed Generator

Hall effect:

The ordinary Hall effect is shown in Fig. 68. A conducting slab is considered which carries a current, I. The magnetic field is applied transverse to the direction of the current and normal to the slab. The magnetic field exerts a Lorentz force on the moving charged electrons and causes deflection in their path. This effect results in the

surface charge at the sides of the slab which causes an electric field and Hall voltage within the slab. The Hall voltage, V_H, and Hall coefficient, R_H, is defined as:

$$V_H = -\frac{IB}{ned} \tag{89}$$

$$R_H = \frac{E}{jB} \tag{90}$$

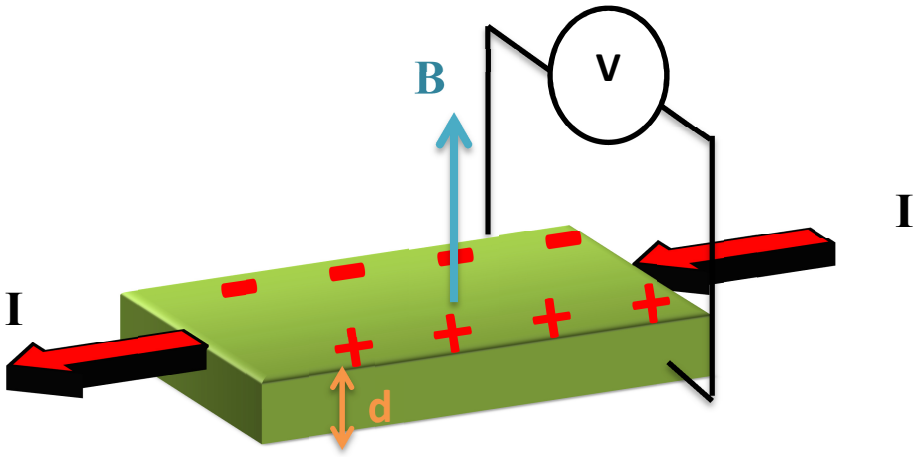

Figure 68: Schematic of Hall Effect.

where I is current, B is the magnetic field, n is electron density, e is electron charge, d is the slab's thickness, E is electric field, and j is current density.

If the conductor is a ferromagnet, there is a second contribution to the Hall signal that is often much larger than the ordinary Hall effect (OHE) and is called the anomalous Hall effect (AHE) or extraordinary Hall effect. In OHE the relation between the Hall resistivity and magnetic field is linear as it is expected from the Lorentz force. AHE, however, shows a nonlinear relation between the Hall resistivity, ρ, and the magnetic field similar to the relation of magnetization and magnetic field. As a result it is shown that the resistivity has two contributions in ferromagnetic materials:

$$\rho_H = R_H B + R_{AHE} M \tag{91}$$

where first term represent the ordinary hall effect and second term represent the AHE. Experimentally it is shown that the AHE >> OHE. AHE is due to the spontaneous

magnetization of the ferromagnet which cause asymmetric scattering of the charged electrons.

In this thesis, the transport measurement (Hall measurement) was done using 4 wire configuration (Fig. 69) where two wires applied current, while the other two wires measured voltage. This measurement was done while the external magnetic field was applied perpendicular to the surface of the sample. The Hall resistance can be calculated and graphed versus field which shows the shape of the hysteresis loop.

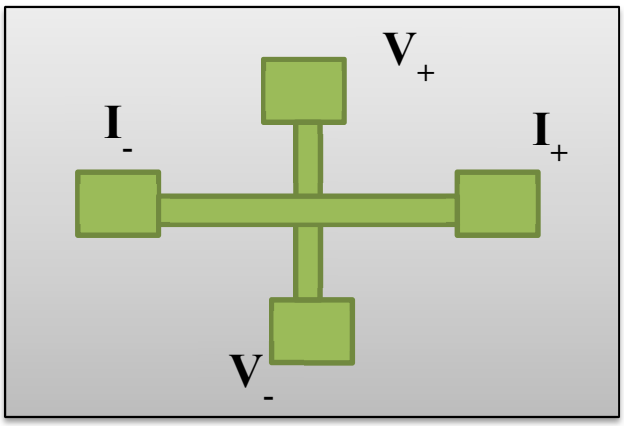

Figure 69: Four point measurement schematic for Hall cross experiment

Sample Preparation:

The samples were prepared on a 4" wafer. Photolithography technique (sec. 3.3) was used to pattern Hall crosses on the wafer, then magnetron sputtering (sec. 3.2) was used to deposit a Cr 5nm/ Pt 2nm bilayer on the wafer and the excess metal was removed through lift-off method. Cr has a good conductivity and it is not

magnetic in room temperature also it is a hard material to etch which helps during the process of patterning the film later. The Pt layer was used to cover the Cr and protect it from oxidization and ensure a good connection between the hall cross and the

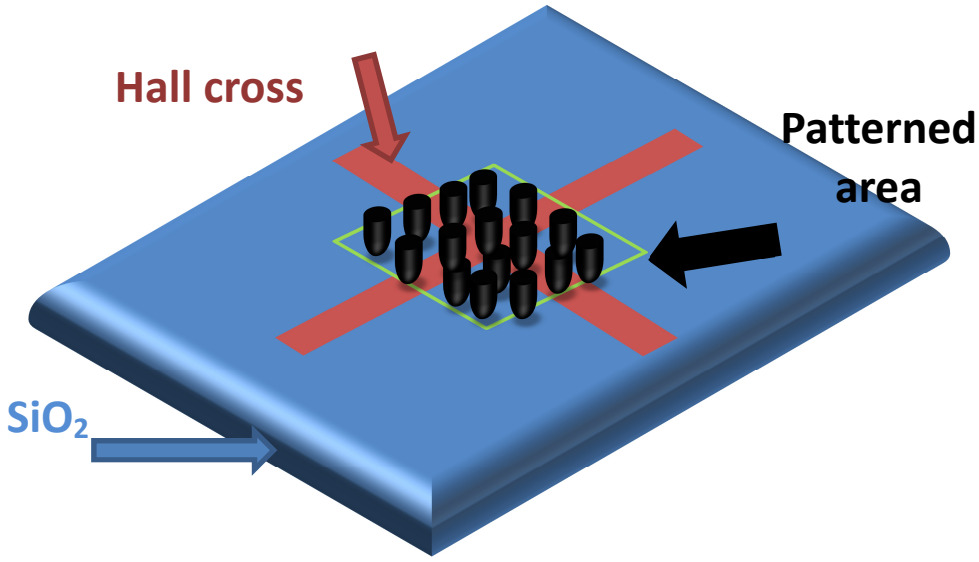

Figure 70: Schematic of fabricated sample for MAMR experiment.

Islands which were patterned later. The magnetic film of structure Pt/[Co/Pt]/Fe/[Pt/Co]/Pt is deposited next on the wafer and covers the whole wafer. The pattern which includes arrays of dots is transferred to the wafer using nano imprint method (Sec. 3.5). The etch post process was used where each resist layer is etched separately and the combination was used as etch mask to pattern the magnetic layer (Fig. 22). The etch processes were calibrated to avoid over etch, but ensure the island separation (magnetically).

To prevent the short between the Hall cross and waveguide 120 nm of Al_2O_3 was grown on top of the sample using atomic layer deposition method which is a directional vapor deposition. During this process the sample is annealed at 250C for about 1 hour which inevitably causes changes in magnetic properties, *i.e*. reduction in coercivity and PMA.

Experiment:

Two techniques were used to apply the RF field to the sample: first, the CPW was directly photolithographed on the sample, and the second, the waveguide was on another substrate (PCB board) and the sample was placed on it faced down and it was made sure that the hall crossing was passed through the center line of the waveguide to ensure that the dots that are being measured by the hall cross are seeing the RF field from the waveguide. The rest of the experiment setup was similar to the FMR-MOKE setup (Fig. 66), except instead of using continuous signal generator we used the pulse generator and used Hall cross to measure the switching of dots in absence of an amplifier. The pulse generator of model Keysight E8257D capable of generating pulses in the frequency range of 100KHz to 67 GHz was used. The RF current was applied in the form of a train of pulses with pulse width 2 μsec and pulse spacing of 2 msec. The frequency was swept from 2- 20 GHz and at each frequency the power swept between 4- 25 dbm.

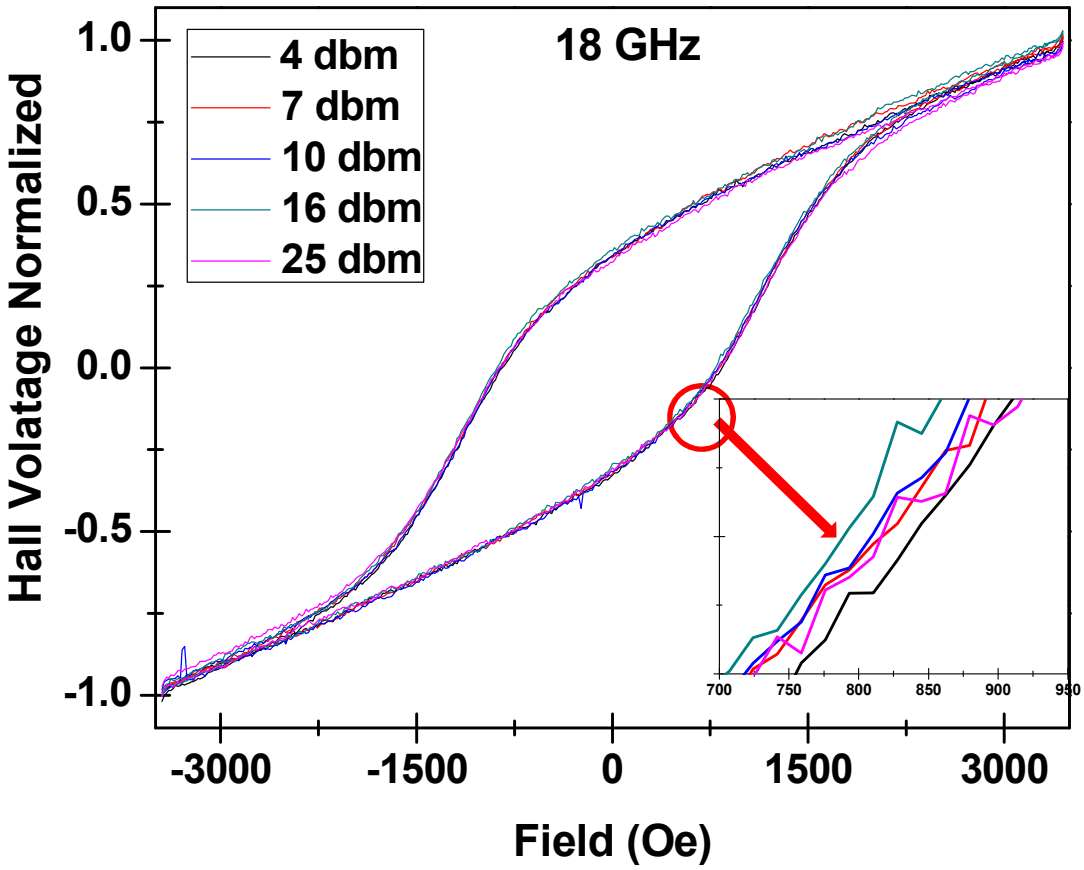

Figure 71: Perpendicular measurement of major loop while the RF magnetici field at 18 GHz s applied perpendicular to the external field at various powers.

The first experiment with patterned waveguide directly on the substrate showed poor impedance matching and most of the power was absorbed within the substrate, so most of the experiments were done with having waveguide on a separate substrate. In Fig. 71 the major loops of sample with structure of Pt(5nm)/[Co0.4/Pt0.7]$_5$ / Fe(2nm) / [Pt(0.7)/Co(0.4)]$_5$/Pt(5nm) is measured at 18 GHz at various powers are compared. Throughout the experiment the maximum

improvement of 100 Oe in switching field was observed for 25 dbm. The improvement in the switching field, unfortunately, was not as high as expected.

The future work on this topic can be considered by modifying the layers structure to vary the total anisotropy and using high power >30dbm RF current to increase the RF magnetic field.

Chapter 6, in part, is currently being prepared for publication. N.Eibagi, J.J. Kan and E.E. Fullerton.

Chapter 7: Conclusion

In this era of information technologies with the increasing rate of produced digital data, there is pressure on the hard disk drive industry to maintain the compound growth rate of storage areal densities as high as possible to address data storage needs. Bit-patterned media is a promising approach to overcome the magnetic trilemma challenge and help the hard disk drive industry to move forward. More generally patterned magnetic nanostructures have the potential for other applications such magnetic memories and oscillators. Also, these structures have the advantage of being combined with other novel data storage techniques to make a game changing step forward.

In this thesis, we studied the combination of perpendicular bit-patterned media with composite structure of [Co/Pd]/Fe/[Pd/Co] and the possibility of using this system with microwave assisted switching. We studied both the static and dynamic magnetic properties of this particular structure.

Through conventional magnetometers, it was found that by varying the Fe thickness, the coercivity and switching field distribution can be tuned. The sample with Fe thickness of 2 nm showed the lowest coercivity and switching field distribution. It was confirmed that although the average islands are thermally stable, there is a distribution of energy barrier due to dipolar interaction. Also, it was shown that the dipolar interaction has the main role in broadening the switching field distribution. To implement these structures as non-volatile HDDs, it is needed to eliminate or control the dipolar interactions. Capped bit patterned media is a promising solution.

The interfacial coupling of layers was studied by neutron reflectometry which confirmed the magnetic behavior of the Fe layer due to exchange coupling to the adjacent Co layers. The perpendicular anisotropy of the multilayers could overcome the in-plane shape anisotropy of the Fe layer. This property is an advantage from dynamic point of view as the resonant frequency can be tuned and suggests the combination of this system with microwave assisted recording techniques. The microwave field potentially can drive the Fe layer into resonance at a lower field and cause the whole system to switch.

The dynamic properties were explored by FMR techniques which confirmed the tunable resonant behavior of Fe layer which makes such structures a good candidate for MAMR. However we weren't able to produce sufficient RF magnetic fields and as a result we weren't able to confirm the improved switching in this particular sample using microwave fields. However, going forward patterned nanomagnets with composite structure also show promising magnetic properties to be implemented as a nonvolatile memory and magnetic oscillators. In all these cases a composite structure allows the higher magnetic energy in the nano-element while still be controlled by external DC and RF fields as well as spin-polarized currents.

Appendix: Energy Barrier Dependence on Power Law

The thermal stability of high-density recording media for archival storage (> 5 years) is a crucial issue to be addressed. In Chapter 4 the method of calculating the energy barrier of a dense bit-patterned media with composite structure is explained. The result showed about an order of magnitude distribution in energy barrier values with respect to the average magnetization value. Through careful analysis and calculations it was confirmed that dipolar interaction mainly causes this distribution.

In this Appendix, I would like to address the effect of the variations in the exponent n in Chantrell et al. equation:

$$H_c(R) = H_0\left[1 - \left(\frac{1}{a}\ln\left(\frac{f_0 H_0}{2a}\frac{1}{R}\right)\right)^{\frac{1}{n}}\right]$$

on the extracted energy barrier values for the samples that are discussed in Chapter 4.

Table 8: Calculated magnetization and anisotropy ratio of soft layer to hard layer for [Co/Pd]5/Fe(x)/[Pd/Cp]5 with x = 1,1.5, and 2 nm.

Parameters	Fe = 1 nm	Fe = 1.5 nm	Fe = 2 nm
$M_s t_s / M_h t_h$	0.24	0.36	0.48
$K_s t_s / K_h t_h$	0.01	0.016	0.02

The value of n = 3/2 was considered in all the Chapter 4 calculations. Sharrock [95] and Victora [96] had discussed that the typical value of n should be 2 for applied magnetic fields along the anisotropy axis of the media and 3/2 for field off the anisotropy axis

(roughly 45 degrees). Bertram [68] explored the power law in composite structures and showed the dependence of n on $M_s t_s$ / $M_h t_h$, $K_s t_s / K_h t_h$, and θ_H. where M is magnetization, t is the layer thickness, K is the anisotropy value and θ_H is the angle of external field with respect to anisotropy axis (where the subscript s and h refer to the soft and hard layers, respectively). The magnetization ratio and the anisotropy ratio is calculated for the samples and the values are given in Table 5. Comparison between the calculated values and Bertram calculation suggest that the choice of n=3/2 is indeed accurate. However, we repeated the calculations in Chapter 4 for n=2 and the results are shown in Fig. 72. This result also shows that there is a distribution in energy barrier and the distribution increases as Fe thickness increases. The calculated values which are in good agreement with measured values confirm that the distribution in energy barrier values is due to dipolar interactions. In Fig. 71 the energy barrier values using two powers of 2 and 3/2 are compared. Although the distribution in energy barrier increases by a factor of 1.6 for n=2, still the fact that the distribution is caused by dipolar interactions holds. That is the data analysis is self-consistent as long as the same exponent n is used but it does result in quantitative differences in the extracted parameters.

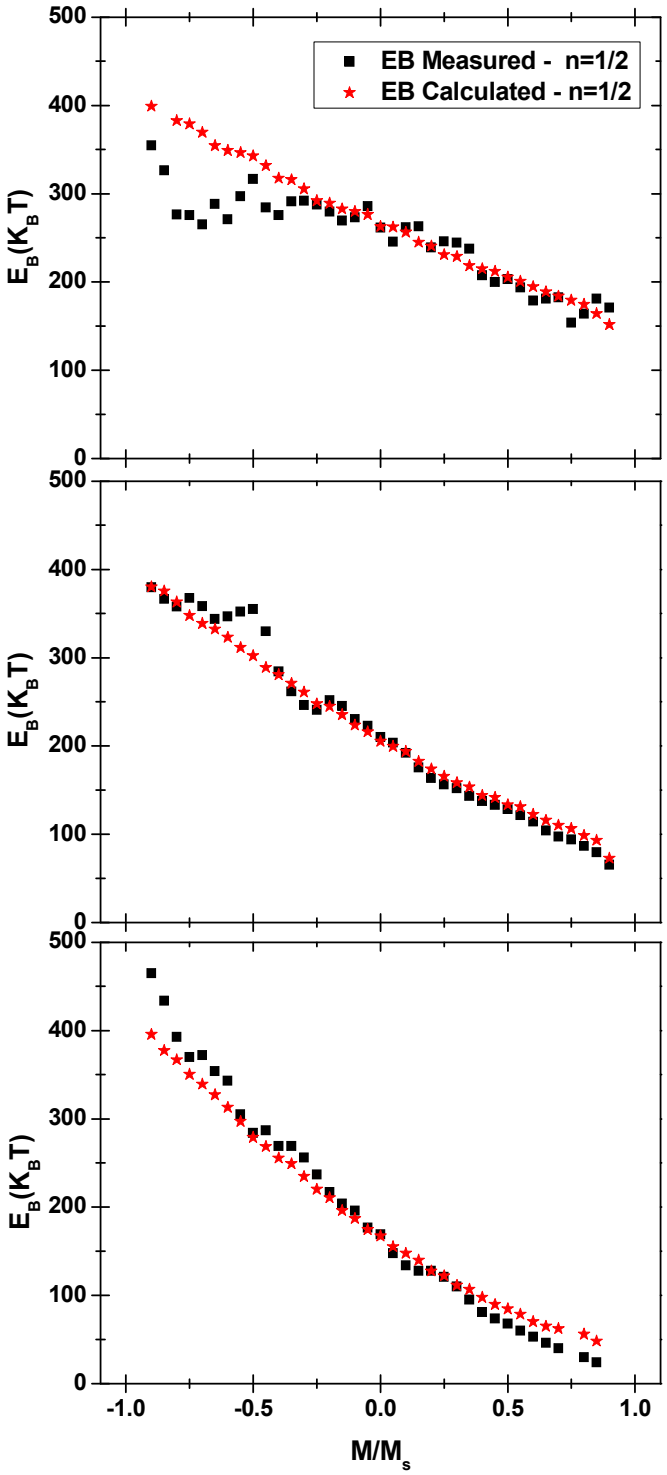

Figure 72: The distribution of energy barriers for [Co/Pd]5/Fe(x)/[Pd/Cp]5 BPM samples: (a) x=1nm,(b) x=1.5nm, and (c) x=2nm. The squares show the measured values of energy barrier for each M/M_S , and the stars are the calculated using eq. 44 with n=2.

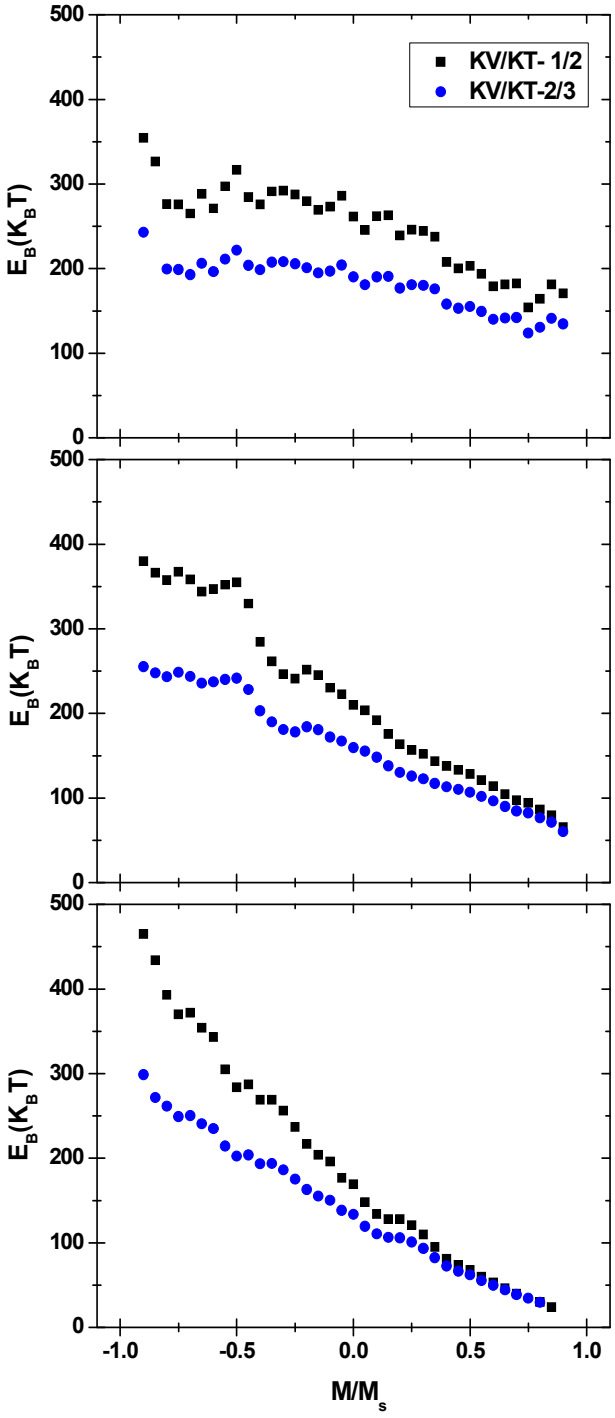

Figure 73: Comparison of energy barrier for [Co/Pd]5/Fe(x)/[Pd/Cp]5 BPM samples: (a) x=1nm,(b) x=1.5nm, and (c) x=2nm for both n=2 and n=3/2. The distribution in is larger by a factor of 1.6 for n=2.

References

(1) V. Turner, J.F. Gantz, D. Reinsel, and S. Minton, " The Digital Universe of Opportunities: Rich Data and the Increasing Value of the Internet of Things", http://idcdocserv.com/1678 (April 2014)

(2) J.F. Gantz, and D. Reinsel, " The Digital Universe in 2020: Big Data, Bigger Digital Shadwos, and Biggest Growth in the Far East" http://www.emc.com/collateral/analyst-reports/idc-the-digital-universe-in-2020.pdf (December 2012)

(3)J.F. Gantz, D. Reinsel, C. Chute, W. Schlichting, J. McArthur, S. Minton, I. Xheneti, A. Toncheva, and A. Manfrediz, " The Expanding Digital Universe", http://www.emc.com/collateral/analyst-reports/idc-the-digital-universe-in-2020.pdf (March 2007)

(4) A. Thierer, "IDC's "Diverse & Exploding Digital Universe" report" http://techliberation.com/2008/03/14/idcs-diverse-exploding-digital-universe-report/ (March 2008)

(5) J.F. Gantz, and D. Reinsel, " As the Economy contracts, the Digital Universe Expands" http://www.emc.com/collateral/leadership/digital-universe/2009DU_final.pdf (May 2009)

(6) J.F. Gantz, and D.Reinsel, " The Digital Universe Decade- Are You Ready?", http://www.emc.com/collateral/leadership/digital-universe/2009DU_final.pdf (May 2010)

(7) J.F. Gantz, and D. Reinsel, " Extracting Value from Chaso" , http://www.emc.com/collateral/analyst-reports/idc-extracting-value-from-chaos-ar.pdf (June 2011)

(8) "Oberlin Smith and the Invention of Magnetic Recording", http://www.oberlinsmith.org/Magrecord/mag-record.html (1988)

(9) "Valdemar Poulsen", IEEE Global History Network, http://www.ieeeghn.org/wiki/index.php/Valdemar_Poulsen

(10) "Magnetic Tape", IEEE Global History Network, http://www.ieeeghn.org/wiki/index.php/Magnetic_Ta

(11) “Magnetic Recording History Pictures”, http://www.aes.org/aeshc/docs/recording.technology.history/tape.html

(12) “RAMAC, The First Magnetic Hard Disk”, http://www-03.ibm.com/ibm/history/ibm100/us/en/icons/ramac/

(13) “The First Disk Drive: RAMAC 350”, http://www.computerhistory.org/revolution/memory-storage/8/233

(14) “IBM 3380 direct access storage device”, http://www-03.ibm.com/ibm/history/exhibits/storage/storage_3380d.html

(15) E. Grochowski, R. E. Fontana, “ Future Technology Challenges For NAND, Flash And HDD Products”, http://www.flashmemorysummit.com/English/Collaterals/Proceedings/2012/20120821_S102A_Grochowski.pdf (2012)

(16) “Toshiba Boosts Perfomances with Industry-Leading Areal Density on 1TB 2.5-Inch Hard Disk Drive for PC and Consumer Electronics Applications” http://www.businesswire.com/news/home/20110801006984/en/Toshiba-Boosts-Performance-Industry-Leading-Areal-Density-1TB#.VJBuCyvF_NE

(17) K. Craige, “ A mechatronic Marvel: The computer Hard Disk Drive, Past-Present-Future”, http://multimechatronics.com/images/uploads/mech_n/Hard_Disk_Drive_Presentation.pdf

(18) “HDD- Hard disk drive”, http://www.helpdisc.rs/eng/data-recovery/hard-disks

(19) S. Iwasaki, “ Perpendicular Magnetic Recording”, IEEE. Trans. Magn., Vol.16, PP. 71-76 (1980).

(20) N. Supper, D.T. Margulies, A. Moser, A. Berger, H. Do, and E. E. Fullerton, “Writability enhancement using exchange spring media”, IEEE Trans. Mag., Vol. 41, PP. 3238-3240 (2005).

(21) A. Berger, N. Supper, Y. Ikeda, B. Lengsfield, A. Moser, and E.E. Fullerton, “Improved media performance in optimally coupled exchange spring layer media”, Appl. Phys. Lett., Vol. 93, PP. 122502-1-3 (2008).

(22) E.E. Fullerton, H.V. Do, D.T. Margulies, and N. Supper, "Incoherently-Reversing Magnetic Laminate with Exchange Coupled Ferromagnetic Layers", United States Patent No. 7,425,377 (2008).

(23) A. Berger, E. E. Fullerton, H. V. Do, and N. Supper, " Perpendicular recording media having an exchange-spring structure", United States Patent No. 7,687,157 (2010).

(24) R.H. Victora, and X. Shen, "Exchange Coupled Composite Media for Perpendicular Magnetic Recording", IEEE. Trans. Magn., Vol. 41, PP. 2828-2833 (2005).

(25) J-P. Wang, W. Shen, and J.Bai, "Exchange Coupled Composite Media for Perpendicular Magnetic Recording", IEEE. Trans. Magn., Vol. 41, PP. 3181-3186 (2005).

(26) D. Suess, J. Lee, J. Fidler, and T. Schrefl, " Exchange-coupled perpendicular media", J. Magn. Magn. Mater., Vol. 321 , PP. 545-554 (2009).

(27) T.R. Albrecht, H. Arora, V. Ayanoor-Vitikkate, J.M. Beaujour, D. Bedau, D. Berman, A.L. Bogdanov, Y.A. Chapuis, J. Cushen, E.E. Dobisz, and G. Doerk, "Bit-Patterned Magnetic Recording: Theory, Media Fabrication, and Recording Performance", IEEE. Trans. Magn., Vol. 51, 0800342 (2015).

(28) W.A. Challener, C. Peng, A.V. Itagi, D. Karns, W. Peng, Y. Peng, x. Yang, X. Zhu, N.J. Gokemeijer, Y-T. Hsia, G. Ju, R.E. Rottmayer, M. A. Seigler, and E.C. Gage, " Heat-assited magnetic recording by a near-field transducer with efficient optical energy transfer" Nature Photonics., Vol. 3, PP. 220-224 (2009).

(29) J-G. Zhu, X. Zhu, and Y. Tang, " Microwave Assited Magnetic Recording", IEEE. Trans. Magn., Vol. 44, PP. 125-131 (2008).

(30) B.D. cullity, and C.D. Graham, "Introduction to Magnetic Materials", 2nd Edition. Wiley-IEEE Press (2008).

(31) M.A. Ruderman, and C. Kittel, "Indirect exchange coupling of nuclear magnetic moments by conduction electrons", Phys. Rev., Vol. 96, PP. 99-102 (1954).

(32) T. Kasuya, "A theory of metallic ferro- and antiferromagnetism on Zener's model", Prog. Theory Phys., Vol. 16, PP. 45-57 (1956).

(33) K. Yosida, “Magnetic properties of Cu-Mn alloys”, Phys. Rev., Vol. 106, PP. 893-898 (1957)

(34) P. Bruno, and C. Chappert, “Oscillatory coupling between ferromagnetic layers separated by a nonmagnetic metal spacer”, Phys. Rev. Lett., Vol. 67, PP. 1602-1605 (1991).

(35) P.J Kelly, and R.D. Arnell, “Magnetron sputtering: a review of recent developments and applications”, Vacuum, Vol. 56, PP. 159-172 (2000).

(36) M. Leskela, and m. Ritala, “ Atomic layer deposition (ALD): from precursors to thin film structures”, Thin solid films, Vol. 409, PP. 138-146 (2002).

(37) M.B. Panish, "Molecular beam epitaxy", *Science* , Vol. 208, PP. 916-922 (1980).

(34) J.R. Arthur, “Molecular beam epitaxy”, Surface science, Vol. 500, PP. 189-217 (2002).

(38) F. A. Lowenheim and S. Senderoff, “Modern Electroplating”, J. Electrochem. Soc., Vol. 111, PP. 262C-263C

(40) M. J. Hampden-Smith, and T.K. Toivo, . "Chemical vapor deposition of metals: Part 1. An overview of CVD processes", *Chemical Vapor Deposition, Vol.1, PP.* 8-23 (1995).

(41) A. Kikitsu, Y. Kamata, M. Sakurai, and K. Naito, “ Recent Progress of Patterned Media”, IEEE. Trans. Magn., vol.43, pp. 3685-3688 (2007).

(42) H. Wang, M.T. Rahman, H. Zhao, Y. Isowaki, Y. Kamata, A. Kikitsu, and J. Wang, “Fabrication of FePt type exchange coupled composite bit patterned media by block copolymer lithography”, J. Appl. Phys. Vol. 109, 07B754 (2011).

(43) S.Y. Chou, P. R. Krauss, and P. J. Renstrom, “ Nanoimprint Lithography”, Journal of Vacuum Science & Technology B 14.6, PP. 4129-4133 (1996).

(44) S. Iwasaki, and O. Kazuhiro, “ Co-Cr recording films with perpendicular magnetic anisotropy”, IEEE. Trans. Magn., Vol. 14, PP. 849-851 (1978).

(45) J.U. Thiele, L. Folks, M.F. Toney, and D.K. Weller, “ Perpendicular magnetic anisotropy and magnetic domain structure in sputtered epitaxial FePt (001) $L1_0$ films”, J. App. Phys., Vol. 84, PP. 5686-5692 (1998).

(46) M.T. Johnson, P.J. Bloemen, F.J. A den Broeder, and J.J. de Vries, " Magnetic anisotropy in metallic multilayers", Rep. Prog. Phys., Vol. 59, PP. 1409-1458 (1996).

(47) W.B. Zeper, F.J. A.M. Greidanus, P.F. Carcia, and C.R. Fincher, "Perpendicular magnetic anisotropy and magneto-optical Kerr effect of vapor-deposited Co/Pt-layered structures", J. App. Phys., Vol. 65, PP. 4971-4975 (1989).

(48) S. Hashimoto, Y. Ochiai, and K. Aso, " Perpendicular magnetic anisotropy and magnetostriction of sputtered Co/Pd and Co/Pt multilayered films", J. App. Phys., Vol 66, PP. 4909-4916 (1989).

(49) S. Ikeda, K. Miura, H. Yamamoto, K. Mizunuma, H.D. Gan, M. Endo, Sl Kanai, J. Hayakawa, F. Matsukura, and H. Ohno, " A perpendicular-anisotropy CoFeB-MgO magnetic tunnel junction", Nature materials., Vol. 9, PP. 721-724 (2010).

(50) E.E. Fullerton, H.V. Do, D.T. Margulies, and N. Supper, "Incoherently-Reversing Magnetic Laminate with Exchange Coupled Ferromagnetic Layers", United States Patent No. 7,425,377, 2008.

(51) N. Supper, D.T. Margulies, A. Moser, A. Berger, H. Do, and E. E. Fullerton, "Writability enhancement using exchange spring media," *IEEE Trans. Mag.*, Vol. 41, No. 10, PP. 3238-3240 (2005).

(52) A. Berger, N. Supper, Y. Ikeda, B. Lengsfield, A. Moser, and E.E. Fullerton, "Improved media performance in optimally coupled exchange spring layer media," *Applied Physics Letters*, Vol. 93, No. 12, PP. 122502-1-3 (2008)**.**

(53) R.H. Victora, and X. Shen, " Exchange Coupled Composite media", Proceedings of the IEEE., Vol 96, PP. 1799-1809 (2008).

(54) B.N. Engel, J. Akerman, B. Butcher, R.W. Dave, M. DeHerrera, M. Durlam, G. Grynkewich, J. Janesky, S.V. Pietambaram, N.D. Rizzo, J.M. Slaughter, K. Smith, J.J. Sun, and S. Tehrani, "A 4-Mb toggle MRAM based on a novelbit and switching method," IEEE Trans. Magn., Vol. 41, no.1, PP. 132-136 (2005).

(55) W. Gallagher, and S.S. Parkin, " Development of the magnetic tunnel junction MRAM at IBM: from first juctions to a 16-Mb MRAM demostrator chip," IBM J. Res. And Dev., Vol.50, PP. 5-23 (2006).

(56) B.D. Terris, and T. Thomson, " Nanofabricated and self-assembled magnetic structures as data stroage media," J. Phys. D: Appl. Phys., Vol. 38, PP. R199-R222 (2005).

(57) A. Moser, K. Takano, D.T. Margulies, M. Albercht, Y. Sonobe, Y. Ikeda, S.H. Sun, and E.E. Fullerton, " Magnetic recording: advancing into the future," J. Phys. D: Appl. Phys., Vol.35, PP. R157-R167 (2002).

(58) O. Hellwig, J.K. Bosworth, E. Dobisz, D. Kercher, T. Hauet, G. Zeltzer, J.D. Risner-Jamtgaard, D. Yaney, R. Ruiz, " Bit Patterned media based on block copolymer direct assembly with narrow magnetic switching field distribution," Appl. Phys. Lett., Vol. 96, 052511 (2010).

(59) A. Berger, Y. Xu, Y. Ikeda, and E.E. Fullerton, "ΔH(M,ΔM) method for the determination of intrinsic switching field distributions in perpendicular media," IEEE Trans. Magn., Vol.41, No. 10, PP. 3178-3180 (2005)

(60) M.V. Lubarda, S. Li, B. Livhitz, E.E. Fullerton, and V. Lomakin, " Reversal in bit patterned media with vertical and lateral exchange," IEEE Trans. Magn., Vol.47, NO.1, PP.18-25 (2011).

(61) I. Tagawa, and Y. Nakamura, " Relationships between high density recording perfance and particle coercivity distribution," IEEE Trans. Magn., Vol.27, PP.4975-4977 (1991).

(62) O. Hellwig, A. Berger, T. Thomson, E. Dobisz, Z. Bandic, H. Yang, D.S. Kercher, and E. E. Fullerton, " Separation diplar broadening from the intrinsic switching field distribution in perpendicular patterned media," Appl. Phys. Lett., vol.90, 162516 (2007).

(63) I. Tudosa, M.V. Lubarda, K.T. Chan, M.A. Escobar, V. Lomakin, and E.E. Fullerton, "Thermal stability of patterned Co/Pd nanodot arrays," Appl. Phys. Lett., Vol. 100, 102401 (2012).

(64) N. Eibagi, J.J. Kan, F.E. Spada, and E.E. Fullerton, "Role of dipolar interactions on the thermal stability of high-density bit-patterned media," IEEE. Magn. Lett., Vol.3, PP. 4500204-4500204 (2012).

(65) E.C. Stoner, " Collective electron ferromagnetism," Proceedings of the Royal Society of London Series a – Mathematical and Physical Sciences, Vo. 165, PP. 372-414 (1938).

(66) M.P. Sharrock, " Time-dependent magnetic phenomena and particle-size effects in recording media," IEEE. Trans. Magn., Vol.26, No.1, PP. 193-197 (1990)

(67) A.M. de witte, M. El-Hilo, K. O'Grady, and R.W. Chantrell, " Sweep rate measurements of coercivity in particulate recording media," J. Magn. Magn. Mat., Vol. 120, PP. 184-186 (1993).

(68) H.N. Bertram, and B. Lengsfield, "Energy barriers in composite media grains," IEEE Trans. Magn., Vol.43, No.6, PP. 2145-2147 (2007).

(69) O. Hellwig, T. Hauet, T. Thomson, E.J.D. Rinser-Jamtgaard, D. Yaney, B.D. Terri, and E.E. Fullerton, " Coercivity tunning Co/Pd multilayer based bit patterned media," Appl. Phys. Lett., Vol.90, 232505 (2009).

(70) M. Ranjbar, S.N. Piramanayagam, S.Z. Deng, K.O. Aung, R. Sbiaa, S.K. Wong, and C.T. Chong, " Antiferromagnetically coupled patterned media and control of switching field distritubtion," IEEE Trans. Magn., Vol.46, No. 6, PP. 1787-1790 (2010).

(71) M.V. Lubarda, S. Li, B. Livhitz, E.E. Fullerton, and V. Lomakin, " Antiferromagnetically coupled capped bit patterned media for high density magnetic recording." Appl. Phys. Lett., Vol. 98, 012513 (2011).

(72) C.F. Majkrzak, " Neutron scattering studies of magnetic thin films and multilayers", Physica B: Condensed Matter, Vol. 221. PP. 342-356 (1996).

(73) S.J. Blundell, and J.A. Bland, "Polarized neutron reflection as a probe of magnetic films and multilayers," Phys. Rev. B., Vol.46, No.6, PP. 3391-3400 (1992).

(74) C.F. Majkrzak, K.V. O'Donovan, and N.F. Berk, "Polarized Neutron Reflectometry," NIST Center for Neutron Research, http://www.ncnr.nist.gov/instruments/ng1refl/pnrchapti.pdf (2004).

(75) C.F. Majkrzak, " Polarized neutron reflectometry," Physica B: Condensed Matter, Vol.173, PP. 75-88 (1991).

(76) V. Lauter, H. Ambaye, R. Goyetter, L.W. Hal, and A. Parizzi, "Highlights from the magnetism reflectometer at the SNS," Physica B: Cond. Mat., Vol.404, PP. 2543-2546 (2009).

(77) "Magnetism Reflectometer at SNS", http://neutrons.ornl.gov/mr/

(78) L.G. Parratt, " Surface studies of solids by total reflection of X-rays," Phys. Rev., Vol. 95, No.2, PP. 359-369 (1954).

(79) X-L. Zhou, " Quantitative analysis of the nonlinear relationship between neutron or x-ray reflectance and the scattering-length-density profile," Phys. Rev. E., Vol. 52, No. 2, PP.1938-1952 (1995).

(80) R. Chang, S. Li, M.V. Lubarda, B. Livshitz, and V. Lomakin, "FastMag: fast 111 micromagnetic simulator for complex magnetic structures", J. Appl. Phys. Vol.109, 07D358 (2011).

(81) P. Sturc, Z. Grait, P. Duhaj, F. Schreiber, and J. Pelzl, " Investigation of magnetoelastic properties of Co-based amorphous alloys by ferromagnetic resonance," IEEE. Trans. Magn., Vol. 34, No. 2, PP. 531-534 (1998).

(82) M. Farle, " Ferromagnetic resonance of ultrathin metallic layers," Reports on Progress in physics, Vol. 166, PP. 6-26 (1998).

(83) B. Hillebrands, and L. Ounadjela, "Spin dynamics in confined magnetic structures II," Topics Appl. Phys., Vol.87, PP. 59-92 (2003).

(84) D. Backes, D. Bedau, H. Liu, J. Langer, and A.D. Kent, "Characterization of interlayer interactions in magnetic random access memory layer stacks using ferromagnetic resonance," J. App. Phys., Vol. 11 (2012).

(85) S. Vonsovskii, " Ferromagnetic resonance: the phenomenon of resonant absorption of a high-frequency magnetic field in ferromagnetic substances," Pergamon Press (1966).

(86) C. Kittel, " On the theory of ferromagnetic resonance absorption," Pys. Rev., Vol.73, No.2, PP.155-161 (1948)

(87) T.L. Gilbert, " A phenomenological theory of damping in ferromagnetic materials," IEEE. Trans. Magn., Vol. 40, PP. 3443 (2004)

(88) C. Bilzer, " Microwave susceptibility of thin ferromagnetic films: metrology and insight into magnetization dynamics," PHD thesis (2007).

(89) J.M. Beaujour, D. Ravelosona, I. Tudosa, E.E. Fullerton, and A.D. Kent, " Ferromagnetic resonance linewidth in ultrathin films with perpendicular magnetic anisotropy," Phys. Rev. B., Vol. 80, 180415(R) (2009).

(90) V. Kambersky, " Ferromagnetic-resonanced damping in metals," Czecholosvak Journal of physics, Vol.26, No. 12, PP. 1366-1383 (1976).

(91) W. Barry, " A broad-band, automated, stripline technique for the siulataneous measurement of complex permitivity and permeability," IEEE Transactions on Microwave Theory and Techniques, Vol. 34, PP. 80-84 (1986).

(92)" Coplanar Waveguide Calculator", http://www.microwaves101.com/calculators/864-coplanar-waveguide-calculator

(93) L. Neudecker, G. Woltersdorf, B. Heinrich, T. Okuno, G. Gubbiotti, and C. H. Back, " Comparison of frequency, field and time domain ferromagnetic resonace methods," J. Magn. Magn. Mat., Vol.307, No.1, PP. 148-156 (2006).

(94) S. Li, B. Livshitz, H.N. Bertram, M. Schabes, T. Schrefl, E.E. Fullerton, and V. Lomakin, "Microwave assisted magnetization reversal in composite media," Appl. Phys. Lett. Vol. 94, PP. 202509 (2009).

(95) M.P. Sharrock, "Time dependence of switching fields in magnetic recording media," J. Appl. Phys., Vol. 76, PP. 6413 (1994)

(96) R. H. Victora, " Predicted time dependence of the switching field for magnetic materials." Phys. Rev. let., Vol. 63, PP. 457 (1989).